

# Sediment transport directions by infragravity waves in the surf zone at the Sandmotor

MSc thesis Earth Surface and Water,  
Coastal dynamics and Fluvial systems

Student name: Florian van der Steen

Student number: 3713865

Start: June 1<sup>st</sup> 2014

Finish: July 31<sup>st</sup> 2015

1<sup>st</sup> supervisor: A.T.M. de Bakker

2<sup>nd</sup> supervisor: prof. dr. B.G. Ruessink



Utrecht University  
Department of Physical Geography  
Faculty of Geosciences

## **Preface**

First of all I would thank my supervisor, Anouk de Bakker for her guidance and for pointing me in the right direction. Laura Brakenhoff for interesting “klets sessies” every now and then. Femmie Roques for saying, “enough is enough for one day”. Marieke Dirksen for her assistance in the field. Gerben Ruessink and the technicians for without them the data-set would not even exist. Finally, my stereo receiver for without its tunes I would probably have gone nuts.

## Abstract

Numerous studies have analyzed the sediment transport by infragravity waves and their relative importance to sea-swell wave induced sediment transport. Sometimes, suspended sediment transport by infragravity-waves can dominate the net sediment transport while, at other times, suspended sediment transport by infragravity waves is insignificant. Furthermore, there is no general consensus on the direction of sediment transport by infragravity waves at a particular location in the surf zone. This study aims to explain the direction of sediment transport by infragravity waves along a cross-shore transect.

Four frames were deployed at a relatively steep-sloping (1:30) beach along a transect during a six week field campaign at the Sandmotor in The Netherlands. Each frame was equipped with Optical Backscatter Sensors (OBS) to measure suspended sediment concentration, a Pressure Transducer (PT) to estimate the sea-surface elevation from pressure below the waves and an ElectroMagnetic Flow meter (EMF) to measure the flow velocity in both cross-shore and alongshore direction.

Fifteen-minute averaged suspended sediment transport calculations are used to determine the direction and relative importance of suspended sediment transport by infragravity, sea-swell and mean transport components. Co-spectra between suspended sediment concentrations and cross-shore velocity are used to examine the frequency dependence of the cross-shore suspended sediment transport rate.

In this study, suspended sediment transport by infragravity waves has the same order of magnitude as sea-swell waves while the mean offshore directed transport is dominant. We observe that the  $r_0$  parameter, which describes correlation between sea-swell waves crest/trough and the infragravity-wave crest/trough, is a useful tool to estimate the direction of transport by infragravity waves. In addition it pinpoints and where peaks in suspended sediment concentrations can be expected relative to the infragravity-wave along the transect. When  $r_0$  has a negative (positive) value which is predominantly in the outer (inner) part of the surf zone, the largest sea-swell waves predominantly occur in the trough (crest) of the infragravity wave and suspended sediment transport by infragravity waves is directed offshore (onshore). When  $r_0$  is negative, intense suspension events predominantly occur during negative infragravity-wave velocities (trough phase). When  $r_0$  becomes increasingly positive towards the shoreline, intense sediment suspension events occur during positive infragravity-wave velocities.

# Contents

Preface .....	2
Abstract.....	3
1. Introduction .....	5
2. Generation and evolution of infragravity waves (literature).....	6
2.1 Generation mechanisms .....	6
2.2 Growth of Infragravity waves .....	7
2.3 Energy flux and reflection .....	9
3. Sediment transport by waves (literature).....	12
3.1 Transport Equations.....	12
3.2 Sea-swell wave induced transport .....	14
3.2.1 Wave shape.....	14
3.2.2 Breaking and turbulence .....	16
3.3 Mean transport .....	16
3.4 Infragravity wave induced transport .....	17
3.4.1 Seaward of the surf zone .....	17
3.4.2 Surf zone .....	18
3.4.3 Swash zone.....	26
4. Methodology.....	27
4.1 Research goal and main and sub questions.....	27
4.2 Field Site.....	27
4.3 Instrumentation .....	27
4.4 Offshore wave conditions .....	28
4.5 Data selection and initial processing .....	30
5. Results.....	34
5.1 Hydrodynamics .....	34
5.2 Sediment transport.....	39
6. Discussion.....	55
6.1 Sub questions.....	55
6.2 Main question .....	55
6.3 Comparison with literature.....	56
6.4 Suggestions for further research .....	58
7. Conclusion.....	59
8. References .....	60

## 1. Introduction

The ocean field can roughly be subdivided into two components, wind generated sea-swell (2-20 s) waves and infragravity (20-200 s) waves. In general, the longer infragravity waves are less energetic than the shorter, higher frequency sea-swell waves. However, they may dominate the water motion, and subsequent sediment transport, close to the shore. Offshore, infragravity waves are bound to the incident sea-swell wave groups. Within a sea-swell group there are variations in wave height. Under sets of relatively large waves there is a set-down (the sea surface slightly drops), while under sets of relatively small-waves there is a set-up (the sea surface is slightly raised). This generates a wave-like motion that is 180° out of phase with the wave group, and where the trough of the secondary wave corresponds to the largest waves in the groups, and the crest corresponds to the smallest waves in the wave group, i.e. a bound infragravity-wave (Figure 1.1).

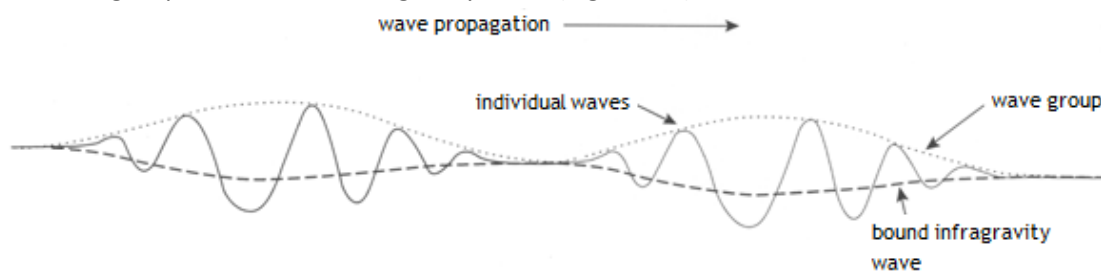


Figure 1.1: Infragravity-wave which is bound to a sea-swell wave group.

Infragravity waves are released in the surf zone, when the group structure disappears, and propagate further to shore as free waves. After reflection at the shoreline, infragravity waves may either be trapped close to the coast (edge waves), or propagate into deep water (leaky waves). Recently, it has been observed that infragravity waves can lose a considerable part of their energy close to shore, potential dissipation mechanisms could either be the breaking of the infragravity wave, the transfer of energy back to the sea-swell waves and energy loss due to bottom friction.

Numerous studies analyse the sediment transport by infragravity frequencies and its relative importance to sea-swell wave induced sediment transport. However, studies often only focus on one aspect, they generally describe either the hydrodynamics or the sediment transport by infragravity waves. In addition, some studies are only based on measurements at one location in the surf zone while often several locations along a cross-shore transect are needed for a thorough analysis. Furthermore, as beach and wave conditions are different for each fieldwork location a comparison between studies is difficult. At present there is no general consensus on what the influence is of the infragravity waves on the direction of sediment transport at a particular location in the surf zone. Several infragravity-wave sediment transport mechanisms have been proposed, varying from the influence of the infragravity waves on the transport of sediment, to their role in the suspension of sediment.

This study aims to explain the direction of infragravity-wave induced sediment transport along a cross-shore transect. The study is part of the MegaPEX 2014 project, which took place in September – October 2014, where many scientists from different fields of study conducted measurements and experiments. The location of the MegaPEX 2014 project is the Sandmotor, which is a 20 million m<sup>3</sup> sand nourishment. The project aims to obtain insight in the processes related to sediment transport, and to understand the impact of such a large nourishment on e.g. the surrounding ecology, beach safety, hydrology etc. For this specific MSc study, instruments were deployed on the southern flank of

the Sandmotor measuring velocities in cross-shore and alongshore direction, suspended sediment concentrations and wave characteristics.

The thesis is build-up as follows; the first two sections are a literature review of infragravity waves with a focus on sediment transport. Sections three and four describe the research questions and methodology of the research, respectively. Section five presents the results of the research. The thesis ends with answering of the research questions in the discussion and conclusion sections.

## 2. Generation and evolution of infragravity waves (literature)

### 2.1 Generation mechanisms

Waves do not only transport energy but also momentum (the product of mass and velocity). This transport of momentum is a stress on the waterbody, horizontal variations in this stress act as forces on the water and are called radiation stresses (Holthuijsen, 2006). Radiation stress ( $S_{xx}$ , transport of x-momentum in the x-direction (cross-shore)) is the transport of wave induced momentum and is capable of generating currents in the water column or tilting the mean sea level. The time averaged radiation stress per unit width and per unit time is given by (in the x-direction):  $S_{xx} = \left(2n - \frac{1}{2}\right)E$  (Holthuijsen, 2006). In which,  $n$  is the ratio of group velocity over phase speed and  $E$  is the wave energy  $E = \frac{1}{8}\rho gH^2$  where  $H^2$  is wave height,  $\rho$  is density of the water and  $g$  is gravitational acceleration.. The tilt in mean water level is given by:  $\frac{d\eta}{dx} = -\frac{1}{\rho g d} \frac{\delta S_{xx}}{\delta x}$ , in which  $\eta$  is mean surface water level and  $d$  is water depth. Here it can be seen that when the gradient in radiation stress  $\left(\frac{\delta S_{xx}}{\delta x}\right)$  is positive the slope in mean surface water level is negative and vice versa. A negative slope results in set-down while a positive slope gives set-up. Within a sea-swell wave group, there are variations in wave height, under relatively large waves the radiation stress causes a set-down while under relatively small waves there is a setup. This generates a wave-like motion that is  $180^\circ$  out of phase with the wave group, and where the trough of the secondary wave corresponds to the largest waves in the groups (Figure 1.1), and the crest corresponds to the smallest waves in the wave group, a bound infragravity wave (e.g. Ruessink, 1998).

Infragravity waves propagate shoreward, together with the sea-swell wave group, and gain energy by means of energy transfer from sea-swell waves to infragravity waves (Longuet-Higgins and Stewart, 1962). When the sea-swell waves start breaking and the group structure disappears, the bound waves are released and become free propagating waves. Whether infragravity waves are bound or free can be examined by the cross-correlation factor ( $r_0$ ). Values vary from -1 to 1 where a value of -1 corresponds to a bound infragravity-wave and a value of 0 means that the infragravity-wave is  $90^\circ$  out of phase with the wave groups and the infragravity wave can be considered as “free”.

In addition to deep ocean infragravity wave generation, another mechanism is hypothesized to generate infragravity waves in shallow water. Symonds (1982) proposes a mechanism where infragravity waves are generated due to a varying breakpoint at the edge of the surf zone. In the shoaling zone, sea-swell waves will generally increase in height causing the wave induced momentum to increase simultaneously. This will lead to a positive gradient in radiation stress and will result in a set-down. At the moment of breaking, waves will dissipate energy and loose height while propagating in the shoreward direction. This loss of energy causes a negative gradient in radiation stress and a wave induced set-up of mean sea level towards the shore, which can be interpreted as an infragravity

wave (thick solid line in Figure 2 | Symonds et al. 1982). The idea is that the groupiness of incident waves causes a time varying breakpoint which induces a time varying wave set-up.

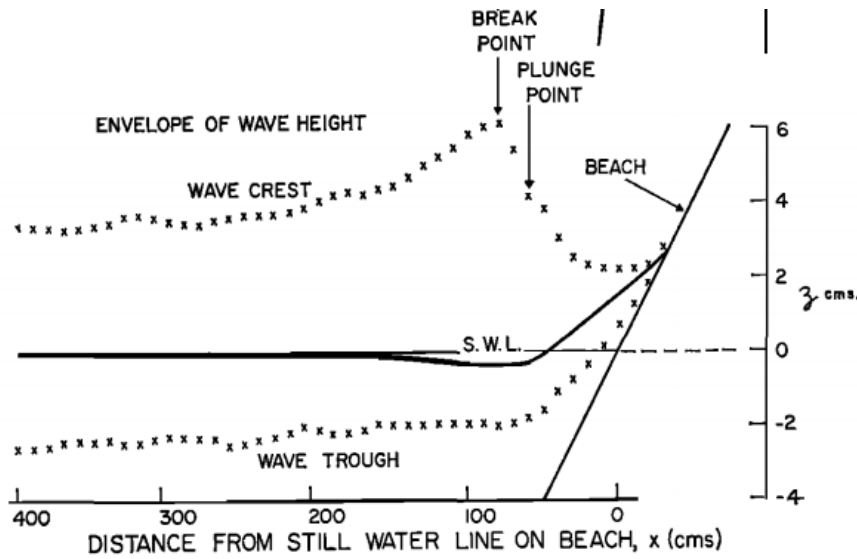


Figure 2.1: Dotted line represents the envelope of the wave crest. Thick solid line indicates whether there is setup or set-down. (source: Bowen et al. 1968)

According to Longuet-Higgins and Stewart (1962) the cross-shore pressure gradient is proportional to the beach slope, thus for a given slope the total set-up depends on the length of the surf zone. When waves arrive in groups, the length of the surf zone will vary in time and so does the total amount of wave-induced set-up for a given wave height. Laboratory experiments by Baldock et al. (2000) have indicated that the breakpoint generation mechanism is dominant on a relatively steep beach (slope 1:10). The relative importance of breakpoint-generated bound waves compared to the generation by incident waves increases with increasing bed slope (Battjes et al., 2004). Field observations show, so far, no clear evidence of a free breakpoint-generated infragravity wave.

## 2.2 Growth of Infragravity waves

When sea-swell wave groups propagate together with the bound infragravity-wave over a sloping bed, the phase difference shifts away from the initial phase difference of  $180^\circ$ . The bound infragravity-wave travels slightly slower than the propagating wave groups and starts to lag behind. The phase shift allows for energy transfer from sea-swell waves to infragravity waves (van Dongeren, 1996). With a larger phase shift, more energy will be transferred. This process allows for a stronger growth compared to the normal shoaling process. Often Green's law is used to describe (conservative/normal) shoaling:

$$\left(\frac{a}{a_0}\right) = \left(\frac{h}{h_0}\right)^{-1/4} \quad (2.1)$$

The equation describes an increase in wave amplitude ( $a$ ) with a decrease in water depth ( $h$ ). However, van Dongeren (1996) showed that due to the energy transfer, Green's law under predicts the total increase in infragravity-wave amplitude. They observed that the shoaling rate of the incoming infragravity wave amplitude lies between Green's law and the shallow-water equilibrium solution

proposed by Longuet-Higgins (1962). The latter describes an amplitude increase proportional to  $h^{-5/2}$  (while Green's law is  $h^{-1/4}$ ).

Battjes et al. (2004) studied the effect of the bed slope on the growth of waves and defined a normalized bed slope parameter. This parameter expresses the relative depth change per wavelength and is given by:

$$\beta = \frac{h_x}{\omega} \sqrt{\frac{g}{h'}} \quad (2.2)$$

In which  $h_x$  is the bed slope,  $\omega$  is the radial frequency of the waves,  $g$  is the gravitational acceleration and  $h'$  is a characteristic value of water depth which depends on the region and process considered, it can be specified for each particular case. The normalized bed slope parameter gives an indication whether a long or short wave experiences the bed slope as steep or gentle. To a longer wave, a given bed slope appears steeper than to a shorter wave as the former experiences a greater change in depth within a wavelength. Battjes et al. (2004) found that for values of  $\beta_s < 0.06$  (for  $h'$  a characteristic shelf depth  $h_s$  is used) a mild-slope regime exists in which the amplitude growth in the shoaling zone is large. For values of  $\beta_s > 0.3$  or  $\beta_b > 0.45$  ( $\beta_b$ , for  $h'$  they use a characteristic breaking depth  $h_b$ ) is a steep slope regime and the growth is weak. Thus, a steep slope corresponds to weak growth and a gentle slope corresponds to large growth.

Van Dongeren et al. (2007) studied the growth rate of incoming infragravity waves with laboratory experiments. Figure 2.2 shows the growth exponent ( $\alpha$ ) plotted against the normalized bed slope parameter ( $\beta_b$ ) for different conditions. The results show a strong decrease in  $\alpha$  with increasing  $\beta_b$  for every parameter, offshore depth, bed slope, sea-swell wave modulation or sea-swell-wave amplitude. It should be noted that the experiments were conducted for conditions for which the sea-swell waves propagate in intermediate water depth, this means that the value of  $-5/2$  will never be reached as that is the shallow water limit. The graph shows that Green's law holds for high values of  $\beta_b$  ( $>1$ , conservative shoaling without energy transfer) and that in intermediate water depths the shoaling exponent increases with decreasing  $\beta_b$  for each different parameter.

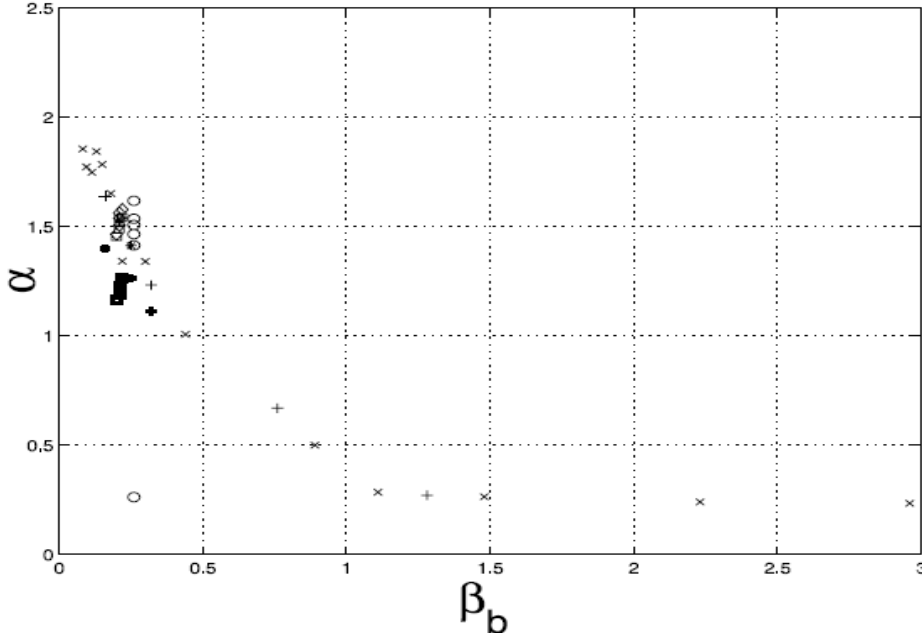


Figure 2.2: Growth rate  $\alpha$  as a function of  $\beta_b$  analysed from physical (bold) and numerical (thin) with several parameter variations: circles – variation in offshore depth, crosses – variation of bed slope, squares – variation of sea-swell wave modulation, diamonds – variation of sea-swell-wave amplitude. (source: van Dongeren et al. 2007)

### 2.3 Energy flux and reflection

Contrary to what was long thought, infragravity waves can dissipate a large part of their energy close to shore (Sheremet et al. 2002, Van Dongeren et al. 2007) instead of reflecting fully at the shoreline. The energy ( $E$ ) at a specific frequency ( $f$ ) can be determined with:

$$E^{\pm}(f, x) = \frac{1}{4} \left[ C o_{pp}(f, x) + \frac{h}{g} C o_{uu}(f, x) \pm \left( 2 \sqrt{\frac{h}{g}} \right) C o_{pu}(f, x) \right] \quad (2.4)$$

The total energy can then be determined as follows:

$$F^{\pm}(f) = E^{\pm}(f) \sqrt{gh} \quad (2.5)$$

With the  $\pm$  denoting whether it is an onshore (+) or offshore (-) directed energy flux and  $\sqrt{gh}$  as the wave celerity in shallow water regime.  $C o_{pp}$  and  $C o_{uu}$  are pressure ( $p$ ) and cross-shore velocity ( $u$ ) auto spectra.  $C o_{pu}$  is the co-spectrum between  $p$  and  $u$ . Energy fluxes ( $E^{\pm}(f)$ ) can be integrated over a specific frequency band  $[f_{min} f_{max}]$  to determine bulk fluxes (Sheremet et al. 2002).

The reflection coefficient ( $R^2$ ) is defined as the ratio between the offshore-directed energy flux ( $F^-$ ) and the onshore directed energy flux ( $F^+$ ) for a specific frequency ( $f$ ) and is given by:

$$R^2(f, x) = F^-(f, x) / F^+(f, x) \quad (2.6)$$

Where  $x$  denotes the cross-shore distance from the shore. When the reflection coefficient at a given location  $x$  is  $< 1$  ( $> 1$ ) then the outgoing flux is smaller (larger) than the incoming flux and energy is lost (gained) between the shoreline and location  $x$ .

Sheremet et al. (2002) conducted experiments in shallow to intermediate water depths analysing energy fluxes and corresponding reflection coefficients of sea-swell wave groups and infragravity waves for a significant wave height of  $H_s = 1$  m and  $H_s = 2$  m. Seaward of the surf zone, where coupling is large (Figure 2.3 g and h), onshore propagating infragravity waves are amplified by non-linear interactions with sea-swell waves and the shoreward energy flux increases (Figure 2.3 c and d). In the surf zone, non-linear energy transfers from the sea-swell peak ceases and the coupling of infragravity waves to sea-swell waves decreases (the infragravity wave becomes “free”). The shoreward energy flux tends to decrease for both infragravity waves and sea-swell waves and dissipation processes become important (Figure 2.3 a, b, c and d). In the case of  $H_s = 2$  m dissipation of infragravity waves seems to larger compared to  $H_s = 1$  m.

In both cases,  $H_s = 1$  m and  $H_s = 2$  m, reflection coefficients ( $R^2$ ) are around 1.0 at the shoreline, decrease in the seaward direction to values between 0.5 and 1.0 and seem to increase again seaward of the surf zone to a maximum of 1.5 (Figure 2.3 e and f). Sea-swell waves completely dissipate in the surf zone. It can be seen that cross-shore variation in the seaward energy flux is less than the onshore energy flux, resulting in a cross-shore reflection coefficient varying between 0.4 and 1.5. Seaward propagating infragravity waves are not coupled to groups of sea-swell and the infragravity-wave flux decreases with increasing distance from the shoreline. It seems that the infragravity-wave flux increases when there is a strong coupling to sea-swell waves.

Several dissipation mechanisms have been suggested in literature. Thomson et al. (2006) and Henderson et al. (2006) observe that energy dissipation of infragravity waves is partly the result of nonlinear transfers of energy from the low-frequency waves back to higher frequency motions (inverse of the generation mechanism). About 80% of the net changes in infragravity energy flux is attributed to nonlinear energy transfers and that other mechanisms (bottom friction and breaking) contributed about 20%. Van Dongeren et al. (2007) hypothesize that energy dissipation of infragravity waves is not due to bottom friction but due to infragravity wave breaking. More recently, De Bakker et al. (2014) found that infragravity-wave energy dissipation can be considerable in natural conditions and that it is frequency dependent. Infragravity-wave breaking is suggested as the most likely dissipation agent, as bottom friction plays a minor role and non-linear energy transfers from infragravity frequencies to higher frequencies are not observed on this very gently sloping beach.

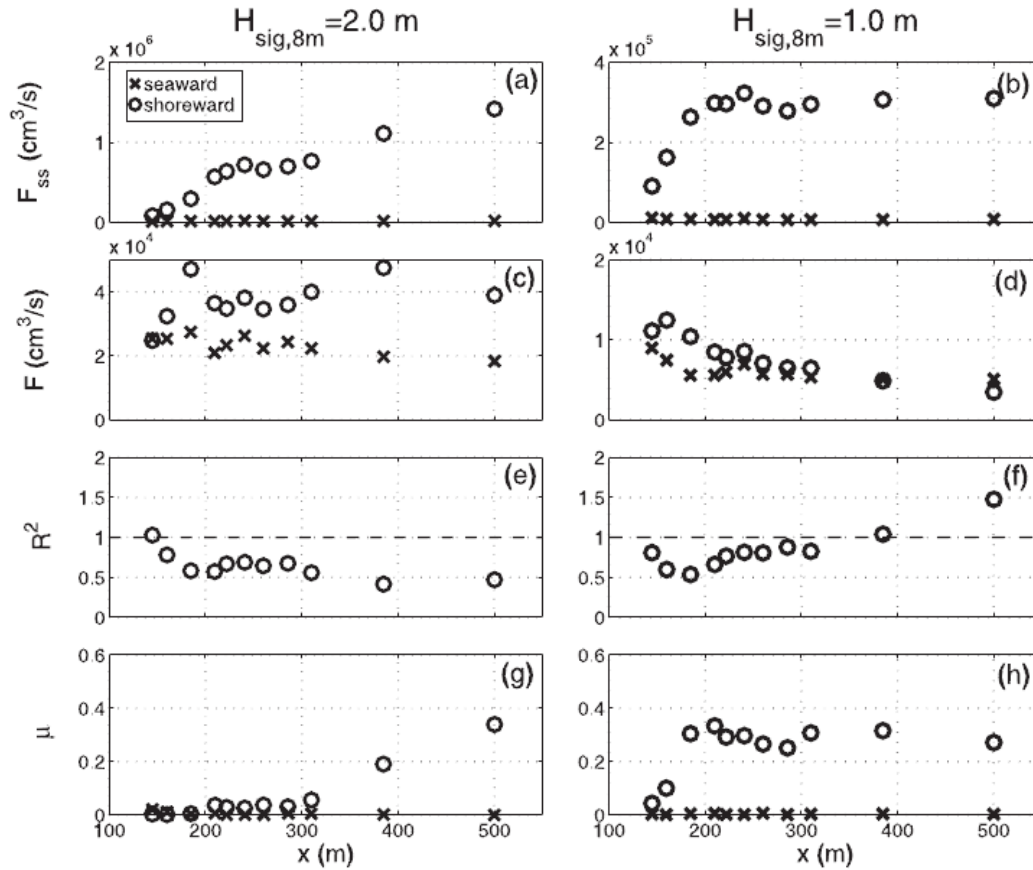


Figure 2.3: (a) and (b) Bulk seaward and shoreward sea-swell energy fluxes; (c) and (d) bulk seaward and shoreward infragravity energy fluxes; (e) and (f) bulk infragravity reflection coefficient  $R^2$ ; and (g) and (h) measures of nonlinear phase coupling  $\mu$  versus cross-shore. Circles and crosses correspond to shoreward and seaward infragravity wave propagation, respectively. Note the different vertical scales for fluxes in the left and right panels. (source: Sheremet et al. 2002)

In addition to infragravity-wave growth, Van Dongeren et al. (2007) found a strong relation between infragravity-wave reflection and the normalized bed slope parameter in which  $h'$  (in equation 2.2) is replaced by the wave height of the incoming infragravity-wave near the shoreline ( $H$ ) (Figure 2.4). A high bed slope parameter results in a high reflection coefficient. Similar results were found by Guedes et al. (2013) and de Bakker et al. (2014) who both found increased reflection coefficients with an increase in normalized bed slope parameter. Furthermore, the lowest (highest) frequencies in the infragravity band showed the highest (lowest) reflection coefficient.

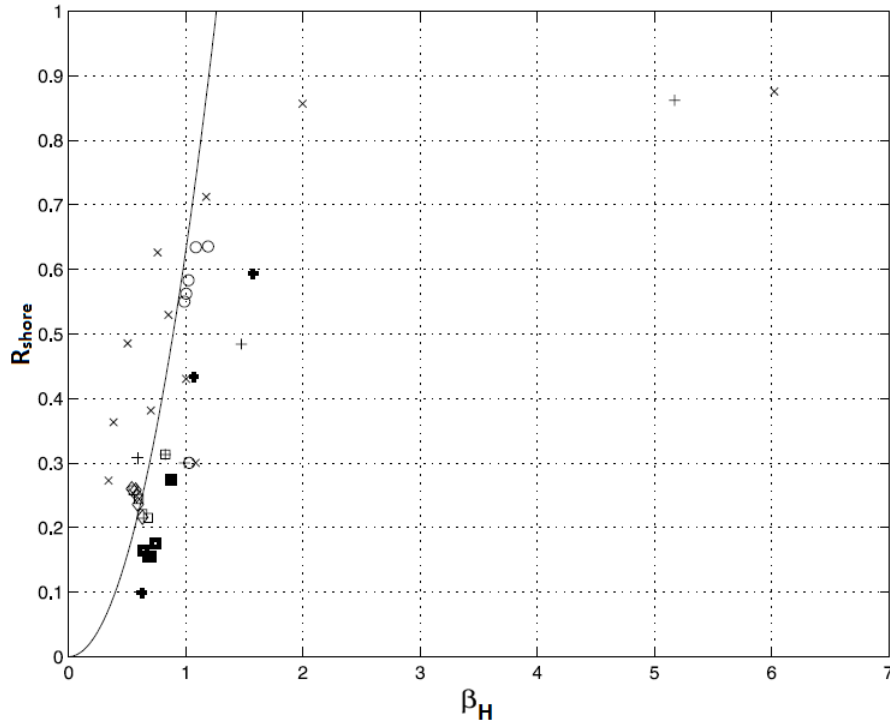


Figure 2.4 Shoreline reflection coefficient  $R$  as a function normalized bed slope parameter  $\beta_H$ , where height of the incoming long wave near the shoreline is used. Equation (8) is plotted as the solid line. The other symbols are the same as those in Figure 2.2 (source: van Dongeren et al. 2007)

### 3. Sediment transport by waves (literature)

Morphological change in the nearshore is driven by spatial and temporal gradients in sediment flux. Although studies show that the contribution by infragravity waves can be significant, the sediment transport mechanisms themselves are poorly understood. Whether infragravity waves stir and transport sediment themselves causing them to be a direct transport mechanism, or whether infragravity waves indirectly enhance or even reduce sediment transport remains unclear. Also sediment transport directions by infragravity waves are still unclear.

In this chapter, sediment transport by both sea-swell and infragravity waves are discussed. First some basic equations are introduced that are used to calculate sediment transport. Secondly, possible sediment stirring and transport mechanisms are investigated. After that, the different sediment transport components are introduced. The section about infragravity waves has been divided into out-and inside the surf zone. Finally a comparison between infragravity-wave sediment transport studies is made, comparing the different conditions and possible/proposed transport mechanisms.

#### 3.1 Transport Equations

Suspension and the consequent transport of sediment is the result of bed shear stress exerted on the bottom by the oscillatory fluid motions. The bed shear stress is proportional to the square of the near bed velocity (Aagaard and Greenwood, 2008). Bed shear stress under waves can be described with:

$$\tau_w = \frac{1}{2} \rho f_w u_o^2 \quad (3.1)$$

In which  $\rho$  is the density of water,  $f_w$  is a bed friction factor and  $u_0$  is the orbital velocity. Each oscillatory motion builds up a bottom boundary layer. Sea-swell waves have the most energetic orbital motions in the nearshore and are, in general, the main contributor to the total bed shear stress. Although very close to the shore infragravity-wave components can become dominant due to the decay of sea-swell waves by wave breaking (e.g. Beach and Sternberg, 1992). In shallow water, the near bed orbital velocity scales with the relative wave height ( $H/h$ ) and can be described with:

$$u_o = \frac{H}{2} \sqrt{\frac{g}{h}} \quad (3.2)$$

In which  $H$  is wave height,  $h$  is water depth and  $g$  is gravitational acceleration. From equations 3.1 and 3.2 it can be seen that the total bed shear stress induced by near bed orbital velocities also scales with relative wave height. Maximum suspended sediment concentrations (resuspension maxima) are expected at relative wave height maxima, where exerted bed shear stress by orbital velocities and turbulence due to breaking are large (Aagaard and Greenwood, 2008). On barred beaches, resuspension and relative wave height maxima occur often in the breaker zone on the seaward slope of bars as waves break. The location of the resuspension maxima shifts back and forth due to the groupiness behaviour of the incident waves. If relative wave height correlates well with suspended sediment concentration, variations in relative wave height in the cross-shore direction (e.g. on a barred shore face) and corresponding cross-shore gradients in bed shear stress will result in the development of cross-shore spatial gradients in suspended sediment.

Sediment transport is usually calculated using velocity and suspended sediment concentration. The total sediment transport can be calculated as follows; the concentration and velocity at any given time is composed of a steady (mean) component and a fluctuating (due to oscillations) component. The local time averaged sediment transport is given by (Russell, 1993):

$$\langle uc \rangle = \langle (u + u')(c + c') \rangle = uc + \langle uc' \rangle + \langle u'c \rangle + \langle u'c' \rangle \quad (3.3)$$

In which  $u$  is mean velocity,  $c$  is mean sediment concentration,  $u'$  and  $c'$  are velocity and sediment concentration around the mean and  $\langle \rangle$  denotes a time average. This equation can be reduced since  $\langle uc' \rangle$  and  $\langle u'c \rangle$  are zero because a time-average over fluctuations around a mean is zero. The reduced form is:

$$\langle uc \rangle = uc + \langle u'c' \rangle \quad (3.4)$$

The fluctuating part can be split up into a high frequency ( $hf$ ) and low-frequency ( $lf$ ) component, so:

$$\langle u'c' \rangle = u_{lf}c_{lf} + u_{hf}c_{hf} + u_{lf}c_{hf} + u_{hf}c_{lf} \quad (3.5)$$

With this the relative contribution to the rate and direction of sediment transport of the different components can be determined. Co-spectral analysis of the suspended sediment concentration (SSC) and cross-shore velocity time-series allows the oscillatory contribution to be sub-divided to give the transport contribution at gravity and infragravity frequencies (Russell, 1993). These transport components are variable in space and time and mainly depend on the wave-height to water depth ratio. Peaks in sediment concentration seem to be associated with individual wave cycles, wave groups and low frequency waves.

## 3.2 Sea-swell wave induced transport

### 3.2.1 Wave shape

When waves reach shallower water and start to feel the bottom they start to shoal, their wavelength will decrease as depth decreases and so will phase speed ( $c$ ) and group velocity ( $c_g$ ). Imagine a single harmonic wave propagating from point P1 to point P2. The assumption is made that energy dissipation from bottom friction can be neglected and that the energy flux ( $F = Ec_g$ ) through P2 is the same as through P1 thus,

$$(Ec_{g,1})_{P_1} = (Ec_{g,2})_{P_2} \quad (3.6)$$

$$\left(\frac{1}{2}\rho gH_1^2c_{g,1}\right) = \left(\frac{1}{2}\rho gH_2^2c_{g,2}\right) \quad (3.7)$$

Since  $c_{g,2}$  is lower than  $c_{g,1}$  the only variable that can increase is the wave height ( $H$ ),  $H_2$  becomes:

$$H_2 = \sqrt{\frac{c_{g,1}}{c_{g,2}}} H_1 \quad (3.8)$$

The shoaling coefficient ( $K_{sh}$ ) is then:

$$K_{sh} = \frac{H_2}{H_1} = \sqrt{\frac{c_{g,1}}{c_{g,2}}} \quad (3.9)$$

If linear wave theory would hold up towards the coast then  $K_{sh}$  would go to infinity, luckily linear wave theory does not hold up and other processes such as refraction and breaking start to determine the evolution of the wave. While shoaling, the wave shape will become skewed; the crest will become sharper and the trough will become broad and flat (Figure 3.1a left panel). Skewness ( $S$ ) can be quantified as follows:

$$S = \frac{\langle u^3 \rangle}{\langle u^2 \rangle^{3/2}} \quad (3.10)$$

in which  $u$  is instantaneous velocity and the brackets denote a time average. Typical values are 0 (not skewed) to 1 (skewed wave). For skewed waves, acceleration from crest to trough and from trough to crest are approximately equal (Figure 3.1b left panel). The higher flow velocity under the crest will mobilize and transport more sediment in the onshore direction than the corresponding offshore directed velocities under the trough (Hsu and Hanes, 2004).

Towards the shore waves will become more asymmetric, with steep front faces and gently sloping rear faces (Fig 3.1a right panel). The asymmetry ( $A$ ) of a wave can be quantified as follows:

$$A = -\frac{\langle a^3 \rangle}{\langle a^2 \rangle^{3/2}} \quad (3.11)$$

in which  $a$  is the acceleration. Typical values are -1,5 (very asymmetric) to 0 (no asymmetry). The flow acceleration has a more or less skewed shape (Figure 3.1b, right panel), larger (smaller) accelerations occur between the transition from trough (crest) to crest (trough). If sediment transport would only depend on flow velocity, the net sediment transport direction of skewed waves would be directed onshore as velocities during the crest are higher than during the trough. The net sediment transport direction of asymmetric waves would be zero as the net maximum flow velocities are equal in both trough and crest. Model simulations by Drake and Calantoni (2001) showed that sediment transport does not only depend on flow velocities. Intense bed load transport is strongly correlated with spikes in fluid acceleration. For asymmetric waves this means that strong fluid accelerations by the steep front face enhances sediment mobilization. Thus, wave shapes that induce a velocity skewness or asymmetry usually generate sediment transport in the direction of wave propagation. Furthermore, phase-lag effects, where sand that is stirred during the negative flow phase is being transported after flow reversal during the positive flow phase, enhance onshore transport (Ruessink et al. 2011). The phase-lag effect becomes relatively more important in finer sands.

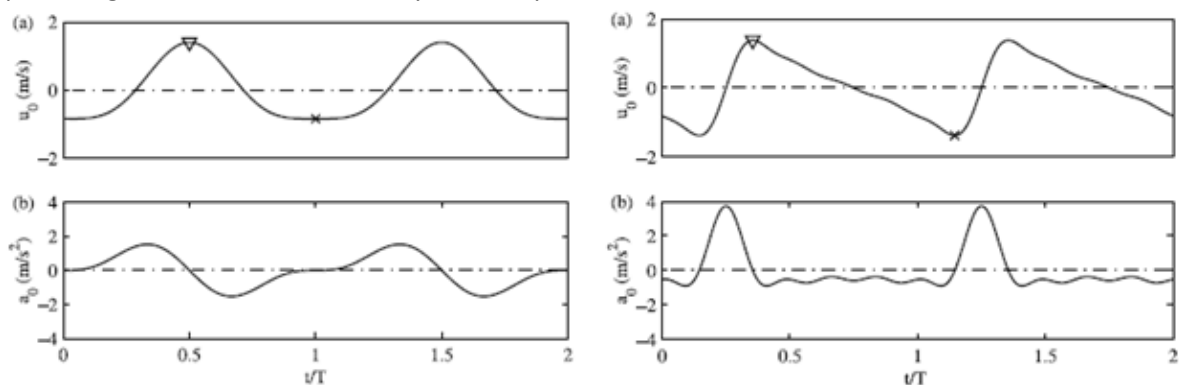


Figure 3.1: Left panels: a) velocity signal of a skewed wave, b) acceleration associated with a skewed wave and, right panels: a) velocity signal of an asymmetric wave, b) acceleration associated with an asymmetric wave (source: Hsu and Hanes, 2004).

Butt and Russell (1999) observed a relationship between infragravity-wave skewness and infragravity-wave transport direction in the swash zone in high and low-energy conditions. During low-energy conditions ( $H_s = 0.8$  m) both sea-swell and infragravity-wave skewness values are positive while for high-energy conditions ( $H_s = 2.2$  m) infragravity wave skewness becomes negative (Figure 3.2). This suggests that there is a process in the infragravity-wave band which could increase offshore transport, due to the increased negative skewness, in high-energy conditions in the swash zone. The increase in negative infragravity wave skewness seems to coincide with an increase in infragravity band energy. The exact process remains unclear, it has been hypothesized by Ozanne (1998) that non-linear interactions between incident and reflected waves led to an increase in negative skewness.

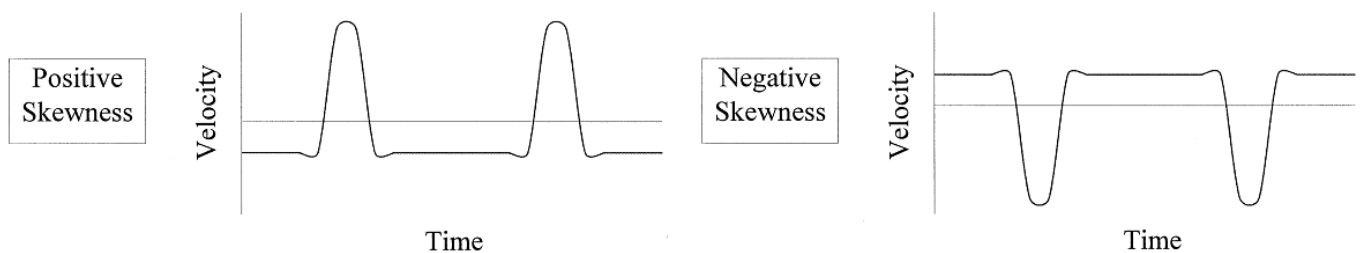


Figure 3.2 Schematic illustration of positive and negative skewness (source: Butt and Russell, 1999).

### **3.2.2 Breaking and turbulence**

Breaking waves cause major alterations in the fluid motions and inject turbulence and air into the water column, which has been suggested as a sediment suspension driver (Thornton, 1979, Aagaard and Hughes, 2006). Upon breaking, wave orbital motions dominate the flow pattern, but as wave breaking process progresses, orbital velocities are reduced and eddy motions and associated turbulence become dominant in the velocity field (Yu et al. 1993). For unbroken waves, suspended sediment transport occurs in a thin layer near the seabed. The sediment concentration increases as the wave progresses landwards due to an increase in orbital velocities near the bed. In the surf zone, overall suspended sediment concentration tend to increase and elevated levels of suspended sediment are present in the entire water column.

Vertical velocity changes significantly during wave breaking; for unbroken waves maximum vertical velocity occurs just in front of the wave crest; upon breaking maximum vertical velocity occurs under the crest and after breaking maximum vertical velocity lags behind the wave crest. The increased vertical velocities and associated eddies bump into the seabed and generate turbulence and bubbles. This causes an increase in overall suspended sediment and an increase in suspended sediment concentration higher up into the water column. The effect of turbulence traveling towards the bed is dependent on the breaker type (Zhang and Sunamura, 1990).

Smith and Mocke (2002) observed suspension events occurring after a series of breaking waves. The suspension events occurred within half of a wave period after the passing of the wave crest. The suspension events near the bed lagged behind vertical velocity events in the water column. The delay for elevated sediment concentration was longer higher up in the water column than near the bed, suggesting the source to be turbulence travelled from the water surface towards the bed and bringing sediment into the water column. The event-like pattern was most prominent at the seaward edge of the surf zone probably caused by the more energetic breaking of sea-swell waves compared to waves well within the surf zone. Alsina and Cáceres observed high levels of turbulence near the bed after the passage of the bore front, indicating that the turbulence produced at the bore indeed travels downward. However, no profound correlation was found between the level of turbulence and suspended sediment concentration. On the contrary high concentrations occurred at the velocity inversion and at the bore front itself, and not after the passage of the bore front when turbulence is highest.

In the inner surf and swash zone, the highest bores do not necessarily cause highest sediment concentration nor does the highest negative/positive flow velocity correspond to the highest sediment concentration (Butt et al. ,2009 and Alsina and Cáceres, 2011). If near-bed velocity shear would be the only suspension agent then the velocity peaks would be expected to be in phase with high suspended sediment concentrations, or at least with a constant phase shift. This is, however, not the case which suggests that, in addition to velocity-shear, other mechanisms such as bore turbulence and acceleration may be important in suspending sediment.

### **3.3 Mean transport**

Mean transport is characterized by a steady offshore directed return flow, called the undertow. In the breaker zone the undertow is an important component for sediment transport. The undertow is based on the principle 'what goes up must come down' or in this case, water that is transported towards the shore has to return towards the sea. Within the surf zone, the undertow is enhanced significantly because of the added onshore mass transport by wave breaking in the upper part of the water column. Near the bed the undertow has its maximum velocity (~0.5 m/s). The strength of the

undertow depends on the negative cross-shore gradient of wave radiation stress which in turn depends partly on beach gradient. For the same wave conditions the undertow is stronger on steep-sloping beaches than on gentle-sloping beaches (Longuet-Higgins and Stewart, 1964). Undertow is the main offshore directed current if the morphology is more or less uniform alongshore. If this is not the case the undertow is replaced by rip circulation (0.5 - 1 m/s).

### **3.4 Infragravity wave induced transport**

Several authors (e.g. Beach and Sternberg 1991, Osborne and Greenwood 1992, Russell 1993, Houser and Greenwood 2005) reported that cross-shore suspended sediment transport by infragravity waves in the surf zone can be significant during high energy conditions. However, the direction of the net infragravity-wave induced transport is unclear and seems erratic for each location. Beach and Sternberg (1991) and Russell (1993) found onshore oscillatory infragravity-wave transport that equalled or exceeded the magnitude of mean cross-shore currents. What follows is a summary of infragravity-wave induced sediment transport and its possible mechanisms at three locations (deep water, surf zone and swash zone) with a focus on the surf zone.

#### **3.4.1 Seaward of the surf zone**

Seaward of the breakpoint the total contribution of infragravity waves to the total sediment transport is small and in theory should be offshore directed. The seaward direction of the infragravity wave component is due to the group behaviour of incident sea-swell waves. The sequences of large sea-swell waves, present in the trough of the bound infragravity-wave (where velocities are offshore directed), stir a larger amount of sediment than the sequences of small sea-swell waves present on the infragravity-wave crest. This generates a net offshore transport (Figure 3.3). That infragravity waves induce a net offshore transport is confirmed by Huntley and Hanes (1987) and Osborne and Greenwood (1992) who observe that the near-bed suspended sediment transport is strongly onshore directed at incident wave frequencies and weakly offshore directed at infragravity frequencies (Figure 3.4ba, giving a net onshore transport overall at locations seaward of the surf zone. Furthermore Huntley and Hanes (1987) observed a change of sediment transport rate with height, showing that the relative contribution of the infragravity-wave decreases with height. Sensors located higher above the sea-bed sometimes even showed onshore directed transport (Figure 3.4b). This is because of the long time lag between the occurrence of suspended sediment peak between the lowest and higher located sensors. Flow reversal can take place during the time it takes for the sediment to reach higher in the water column which can result in net onshore suspended sediment transport.

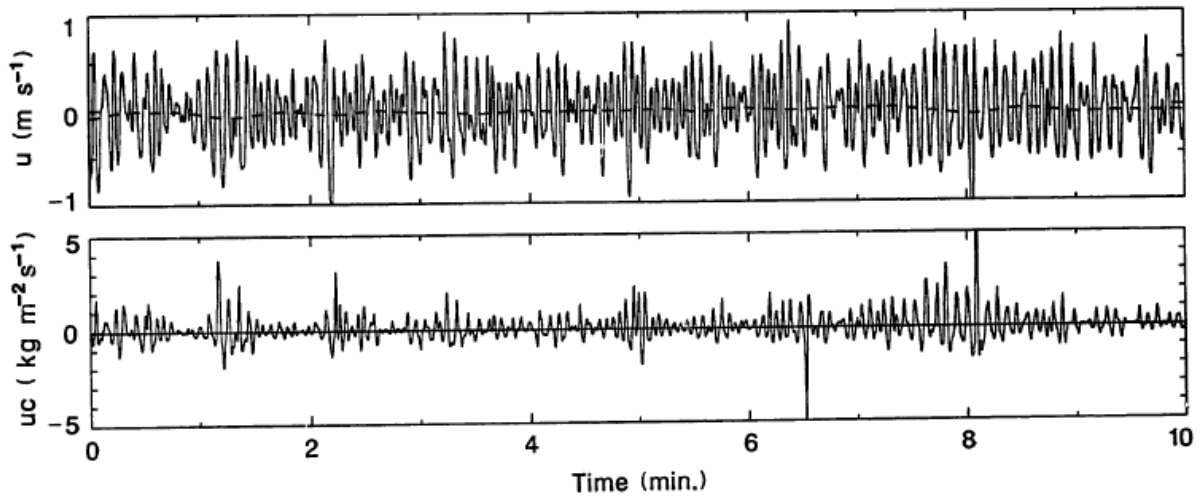


Figure 3.3: Time-series of cross-shore velocity (solid line) and suspended sediment transport ( $uc$ ) dashed line: low pass filtered series. (source: Osborne and Greenwood, 1992)

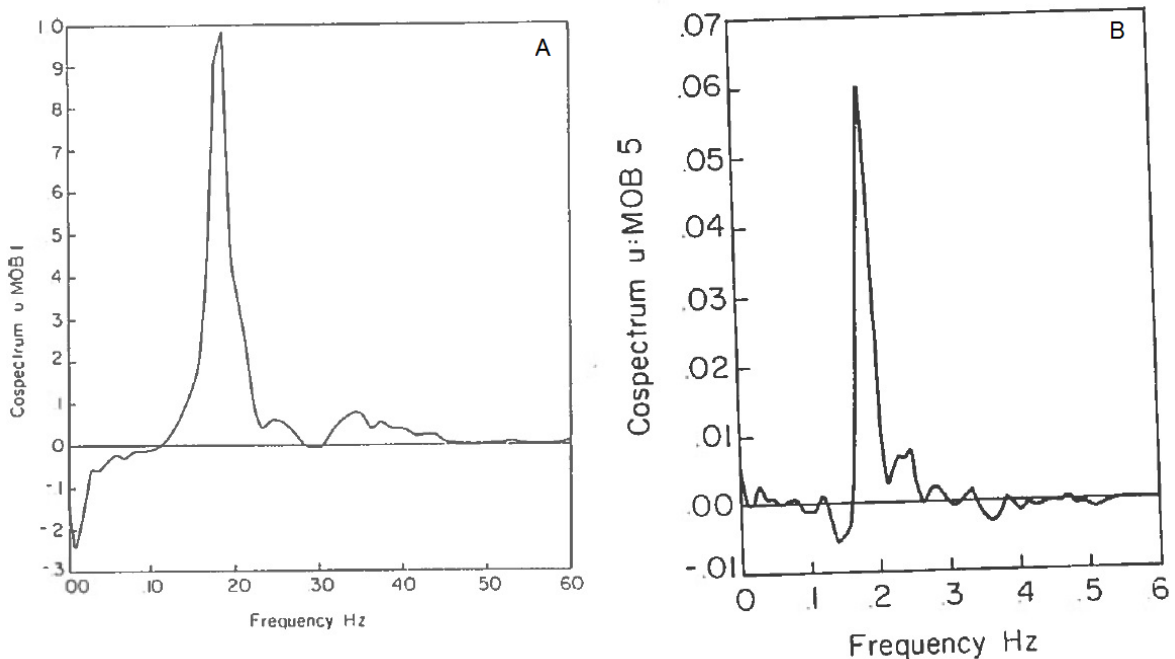


Figure 3.4: Co-spectrum between velocity and suspended sediment concentration at a) MOB1 (sensor closest to the bed) and b) MOB5 (higher located sensor). (source: Huntley and Hanes, 1987)

### 3.4.2 Surf zone

The location where the surf zone begins depends on relative waterdepth ( $H/h$ ). High energetic conditions cause waves to break further offshore compared to low energetic conditions. The boundary between the surf and shoaling zone is never static and shifts back and forth constantly due to incident wave groups. Smith and Mocke (2002) defined a transition zone as the region extending from the commencement of wave breaking to a point where bores are fully developed. In this region the infragravity-wave shifts from a bound wave towards a free wave causing infragravity waves to alter from being a transporting agent to a possible sediment suspending agent.

## Advection

Sediment concentrations within the surf zone are highest at the resuspension maxima, where relative wave height is high. Here the infragravity waves act as an advection mechanism and transport the sediment suspended by the sea-swell waves. Aagaard and Greenwood (2008) suggest that transport direction may depend on the position within the surf zone relative to a sediment resuspension maximum. Infragravity waves would then pick-up most of their sediment at a resuspension maximum which slowly settles out with time, creating a cross-shore gradient in sediment concentration around the resuspension maximum. They suggest that, as a result of this, net infragravity-wave sediment transport should be directed onshore (offshore) landward (seaward) of such a maximum however the authors do not state clearly why this is the case. Figure 3.5 shows results from Aagaard and Greenwood (2008) where net infragravity-wave fluxes are plotted against the position relative to resuspension maxima. Shoreward of the resuspension maxima the flux is directed onshore while seaward the flux is directed offshore.

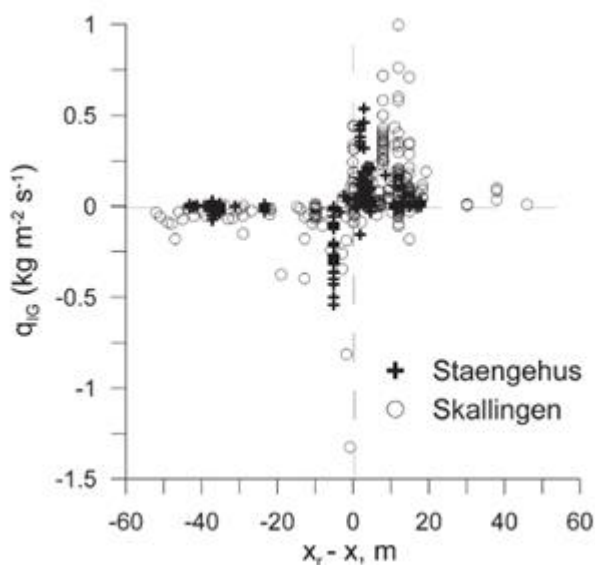


Figure 3.5: Observed net infragravity sediment fluxes ( $q_{ig}$ ) against measurement position relative to resuspension maxima ( $x_r - x$ ). Positive values of ( $x_r - x$ ) indicate that the measurement position is located landward of the resuspension maximum. (source: Aagaard and Greenwood, 2008)

## Enhanced sea-swell wave breaking

A laboratory study by Smith and Mocke (2002) showed that sediment suspension and oscillatory transport flux were dominated by infragravity-wave frequencies in the surf zone. They state that increased sediment suspension on the infragravity scale is caused by local water-level lowering at the trough of the infragravity-wave which results in increased sea-swell wave breaking activity (Figure 3.6).

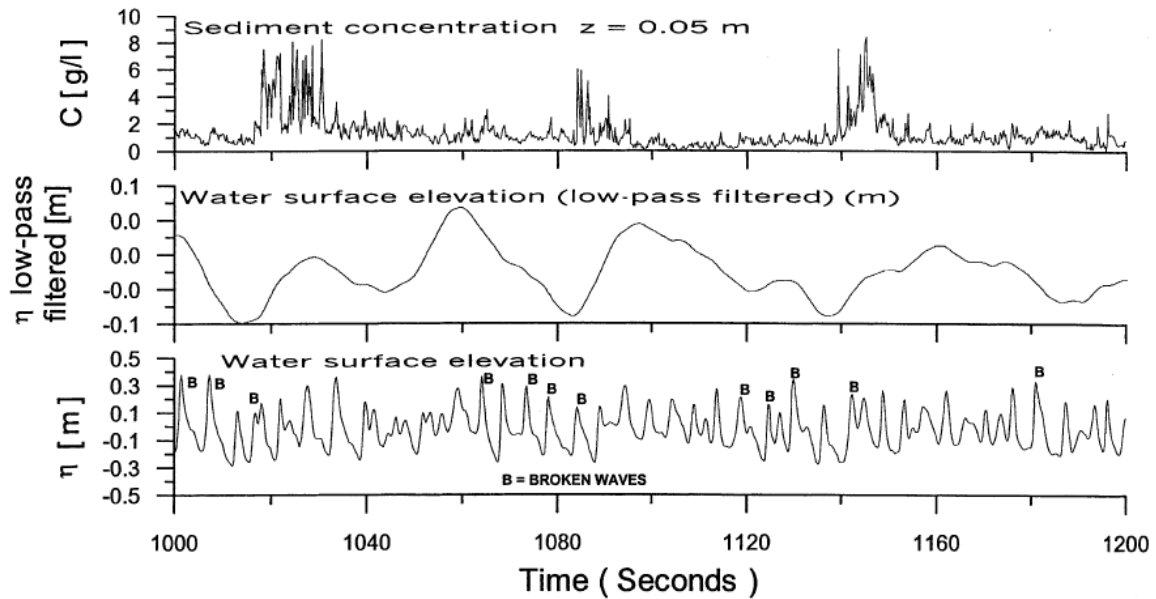


Figure 3.6: Time series of near-bed sediment concentration (top), water surface elevation (bottom) and low-pass-filtered water surface elevation ( $< 0.05$  Hz) (centre). Sediment suspension is evident soon after troughs in the latter time series (and after corresponding broken waves). (source: Smith and Mocke, 2002)

Similar results were achieved by Alsina and Cáceres (2011) who found that high suspended sediment concentrations in the inner surf zone and swash zone occur in combination with broken sea-swell waves during an infragravity-wave trough. Correlations between suspended-sediment concentration and turbulent kinetic energy or square incident horizontal velocity were low and showed no distinct relation. However, correlations seem to improve when computed during the trough of an infragravity wave (Figure 3.7).

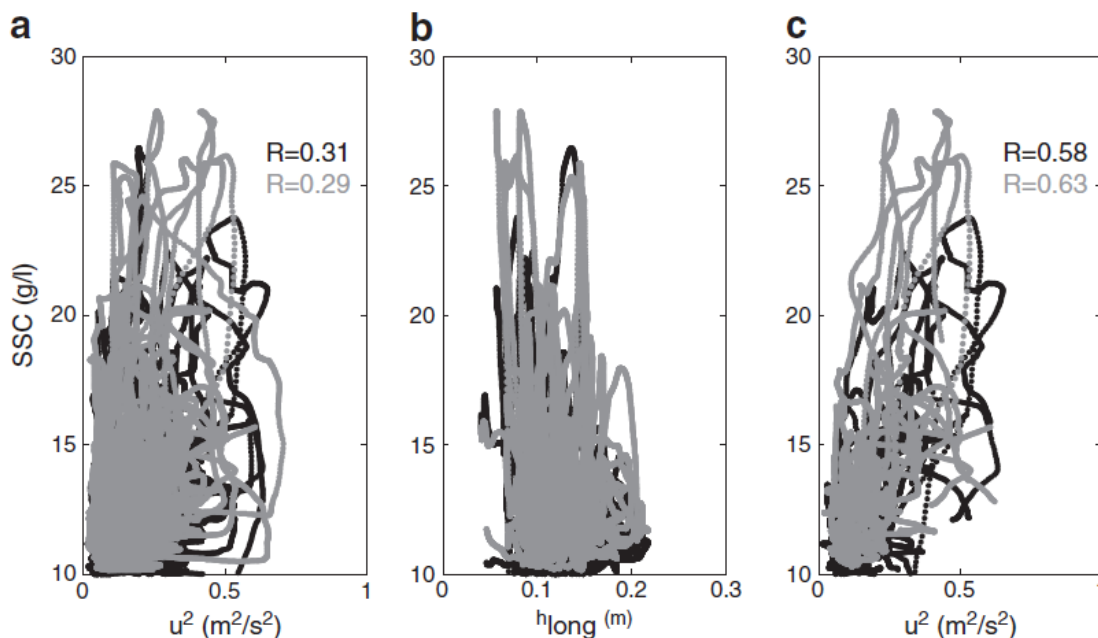


Figure 3.7: Correlation plots between suspended sediment concentration and: a) square sea-swell wave velocity, b) long wave water surface elevation and c) square sea-swell wave velocity computed during depression of the long wave water surface elevation. Data corresponding to test 10, cross-shore location  $x=-2.71$  m and vertical elevations from the bed level of 4 cm (black) and 9 cm (grey). (source: Alsina and Cáceres, 2011)

### Infragravity wave velocities

Contrary to both the increased breaking of sea-swell waves facilitated by infragravity waves and the advection mechanism, Beach & Sternberg (1988) observed a direct influence of the infragravity-wave on the suspension of sediment. A time-series obtained during their field experiments is shown in Figure 3.8. They investigated the influence of infragravity waves on suspended sediment and subsequent transport with an 11-minute time series. During the first 5.5 minutes strong infragravity wave motions existed but were absent during the rest of the time series. This gave the authors the opportunity to determine the relative importance of infragravity waves and sea-swell wave motions on suspended sediment transport while other forcing factors such as, wind, water levels, incident wave height, morphology etc. remained more or less the same. The findings showed that, during the first 5.5 minutes, 85% of the cross-shore velocity variance occurred in the infragravity band. The initiation of sediment movement and peak concentration occurred during the trough phase of the infragravity wave. Furthermore, the vertical structure of sediment concentrations developed and decayed at the infragravity wave scale, rather than at sea-swell wave scale. Here it is expected that the infragravity wave is stirring agent.

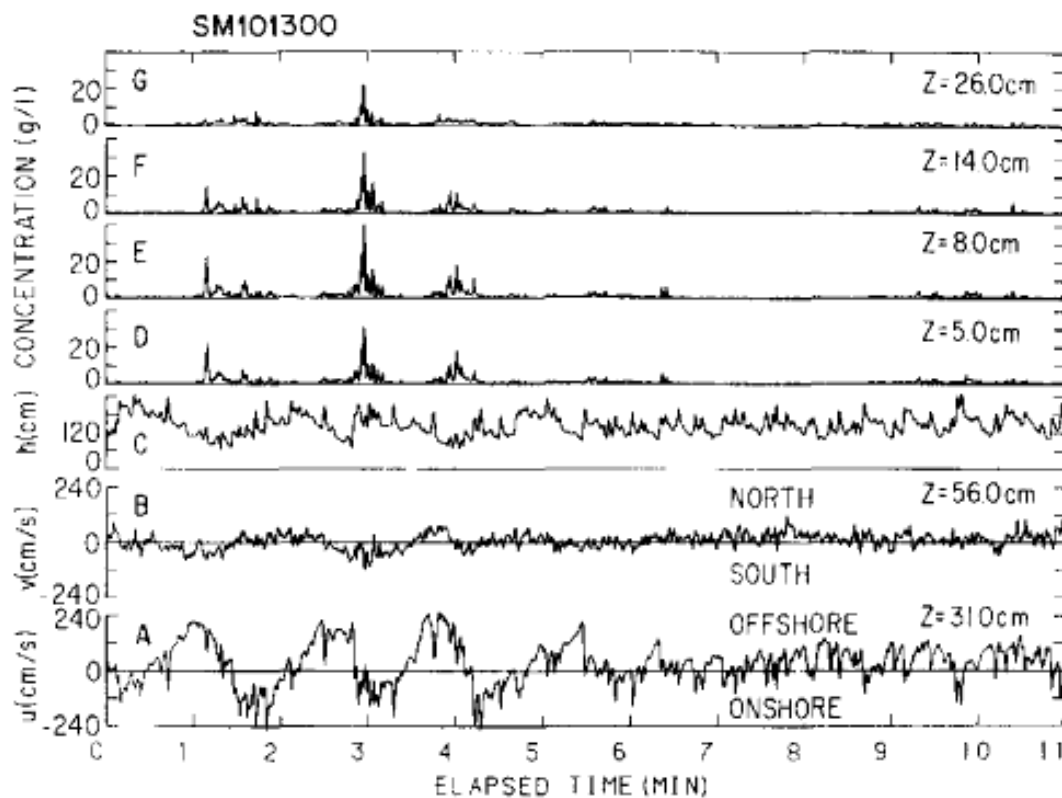


Figure 3.8: Time series as recorded at the central array. a) cross-shore velocity, b) longshore velocity, c) sea level fluctuations and d-g) suspended sediment concentration at four levels  $z$  above the bed. Note that when velocity is stated as positive, the transport is in the offshore direction. (source: Beach and Sternberg, 1988)

### Transport

Because the mechanisms of sediment suspension and/or transport by infragravity waves are spanning a whole range of processes, the direction of the net low-frequency oscillatory transport is not well understood. The direction and magnitude of sediment transport is seen to vary with the location in the surf zone and the present morphology at that particular location.

Russel (1993) observed that on a moderately sloping beach (1:70) transport at infragravity frequencies was mostly offshore directed, except during the flood tide of a storm. During the following

ebb-tide, infragravity-wave induced sediment transport was directed offshore again and dominated shoreward from the inner surf zone (Table 3-1). The sediment suspension events were more frequent and their duration and concentration increased with decreasing waterdepth.

Houser and Greenwood (2005) found that net infragravity transport depended on the position relative to the breakpoint in the inner surf zone of a dissipative beach. When incoming waves broke seaward of a bar, the direction of transport at the bar was directed onshore, forcing an onshore migration of the bar. When waves broke landward of the bar crest the transport was directed offshore. The onshore sediment transport increased linearly with relative wave height for values of  $H/h$  larger than 0.4 (Figure 3.9 b, f).

*Table 3-1: Comparison of transport directions of different components on a high-energy macrotidal dissipative beach in the inner surf zone, data from Russell (1993).*

	Mean	High frequency	Low frequency
Calm flood	Weak offshore	onshore	Weak offshore
Calm ebb	Offshore	offshore	Offshore
Storm flood	Offshore	-	onshore
Storm Ebb	Offshore	-	Strong offshore

Aagaard and Greenwood (2008) observed that the contribution of infragravity waves to the sediment flux increased dramatically with decreasing water depth within the surf zone but found no consistent transport direction (Figure 3.10). Measurements were done on two different cross-shore profiles at Skallingen and Staengehus (Denmark). Skallingen is a triple barred system which is in a dissipative state, it has a gently sloping surface of about 0.005. The beach at Staengehus is also triple barred but slightly steeper (0.016). The normalized transport reached values of 0.4 and up to 0.8 close to the shoreline, dominating the net suspended sediment transport. Outside the surf zone, the sediment flux was mostly directed offshore and contributed for less than 25% of the total suspended sediment flux. At times the infragravity frequencies completely dominated the sediment flux and was the main forcing factor for morphological alterations. Here, net infragravity-wave transport potentially contributed up to 40% of the total suspended sediment flux in the mid-surf zone. The other 60% was attributed to sea-swell waves and mean currents. However, the latter two are often directed oppositely, causing sediment transport by infragravity wave to become important for the net transport.

An overview of all the studies can be seen in Table 3-2.

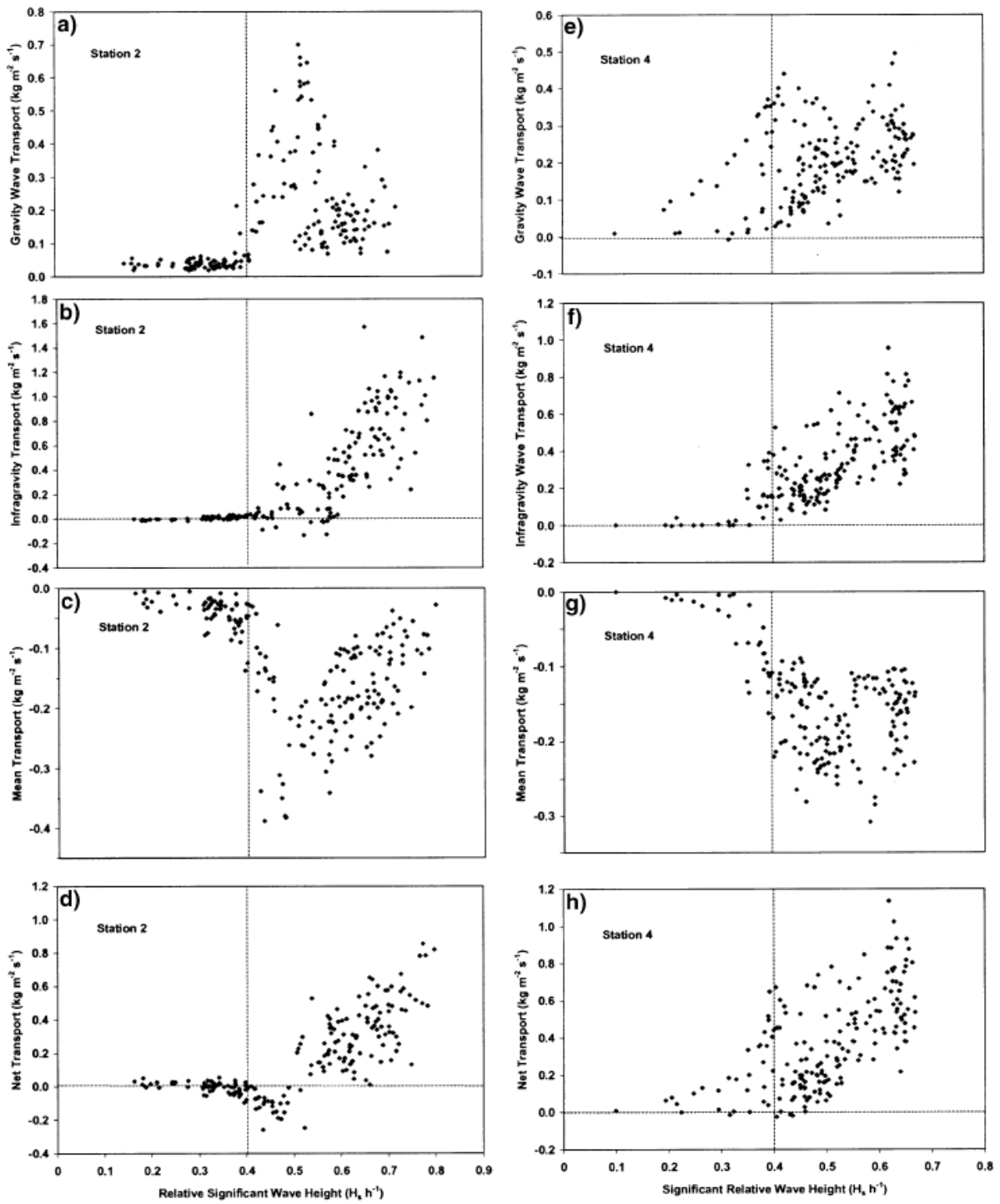


Figure 3.9: Measured gravity wave (a, e), infragravity wave (b, f), mean (c, g), and net suspended sediment transport (d, h) at Stations 2 (a–d) and 4 (e–h) relative to the respective local relative significant wave height ( $H_s h^{-1}$ ). Positive values indicate a shoreward and negative values indicate offshore flux of sediment. Note the differing axis between station 2 and 4 (left and right panels). (source: Houser and Greenwood, 2005)

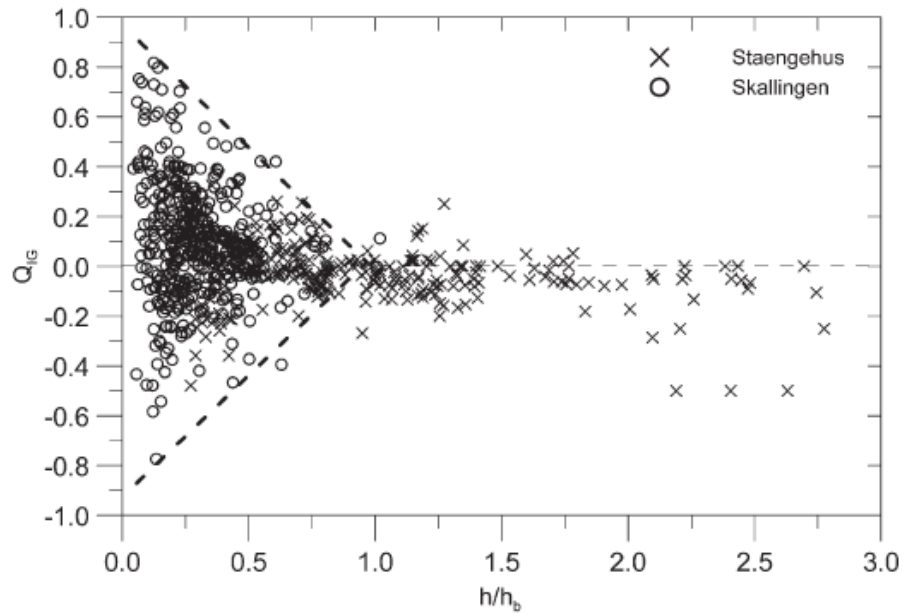


Figure 3.10: Normalized oscillatory infragravity wave sediment flux ( $Q_{ig}$ ) as a function of local water depth relative to the water depth at the first (outer) wave breakpoint ( $h/h_b$ ). The sloping dashed lines are the approximate maximum values of  $Q_{ig}$ . (source: Aagaard and Greenwood, 2008).

Author	Osborne and Greenwood (1992)	Russell (1993)	Houser and Greenwood (2005)	Beach and Sternberg (1988)	Aagaard and Greenwood (2008) (Skallingen)	Aagaard and Greenwood (2008) (Staengehus)	Huntley and Hanes (1987)
<b>Slope</b>	Near the shoreline 1:10, decreasing to 1:33 further offshore	Moderate slope, 1:70	Low slope, 1:110	Steep slope, 1:33	Low slope, 1:200	Moderate slope, 1:63	-
<b>Grainsize D<sub>50</sub></b>	0.16 - 0.27 increasing in shoreward direction	0.23 mm	0.18 – 0.20 mm	0.23 mm	-	-	-
<b>Coastal regime</b>	<i>Surf zone and just outside the surf zone</i>	<i>Surf zone during high and low – energy conditions</i>	<i>Surf zone and inner surf zone</i>	<i>Surf zone</i>	<i>Entire nearshore</i>	<i>Entire nearshore</i>	<i>Outside the surf zone</i>
<b>Tidal range and wave height</b>	Meso tidal, about 2 m.	Macro tidal, 8.5 on springs and 4.1m on neaps	none	Meso tidal, about 2.2 m. Significant wave height of 2 m	Meso tidal, about 1.8 m, mean annual wave height 1 m	Small tidal range, 0.25 m. Mean annual wave height 0.35 m	-
<b>Nr. Of bars</b>	0	0	3	2	3	3	-
<b>Other notes</b>	Periods of wind-forced waves, followed by long crested swell.	Both wind-driven and long period swell, Spilling breakers	Limited fetch, storm-generated wind waves. Bars not broken up by rip channels. Relative wave height varying from 0.2 – 0.7.	mean waterdepth, 1.2 m	Low relief of the nearshore bars, often broken up by rip channels, mean annual wave height	Large nearshore bars with deep troughs, crescentic shaped bars,	Sand ripples would be expected
<b>Possible transport mechanism</b>	Advection	Calm: advection Storm flood: both Storm ebb: infragravity velocities or enh. sea-swell wave breaking.	Advection	Infragravity wave velocities	Advection	Advection	Advection
<b>Direction</b>	Offshore outside the surf zone, onshore inside the surf zone	see table 3-1	Onshore (offshore) when wave broke seawards (landwards) of bar crest	Offshore close to the shoreline,	Both onshore and offshore	Both onshore and offshore	Generally offshore, but seen to be height dependent

Table 3-2: Summary of hydrodynamic and morphological characteristics of different field campaigns.

### **3.4.3 Swash zone**

The swash zone is the limit between the aerial and the submerged part of the beach which is intermittently inundated by wave action. A swash event consists of an uprush and a down rush event and is characterized by high turbulence levels, unsteady flows and large sediment transport rates (Alsina and Cáceres, 2011). Butt and Russell (1999) found that the onshore transport by the uprush phase of the swash zone has a different transport mechanism compared to the thin flowing backwash and cannot be considered reversals of each other. Turbulence is probably the main suspension mechanism during the uprush which is caused by a sudden transition from offshore to onshore velocities, rather than the near bottom flow acceleration. Sediment transport for both low- and high-energy conditions is onshore, but the ratio between on- and offshore transport becomes less for high energy conditions (Butt and Russell, 1999). Observations in the swash-zone area so far have been slim, mainly caused by the difficult measurement conditions and the lack of proper measurement equipment.

Swash motions can be dominated by infragravity-wave frequencies. This predominantly occurs on gently sloping beaches with low values of the Iribarren number and where sea-swell wave energy dissipation rate in the inner surf and swash zone is relatively larger than that of waves in the infragravity range. The energy density spectrum changes considerably from the beginning of the breaker zone towards the swash zone in high energy dissipative conditions. In saturated surf zones the energy in the infragravity band tends to increase shorewards (Russell, 1993). As a result the shoreline becomes increasingly more infragravity dominated as the offshore wave height increases.

## 4. Methodology

### 4.1 Research goal and main and sub questions

The objective of the present study is to investigate the sediment transport directions in the surf zone at the Sandmotor, with a focus on the role of infragravity waves. The main question for this study is: What are the processes behind the spatial variability in the cross-shore direction of sediment transport induced by infragravity waves? The sub questions are formulated in such a way that the observations found in the main question might be explained.

1. What is the relative importance of infragravity-wave induced sediment transport compared to transport by sea-swell waves and the mean transport, during different wave conditions?
2. Can we identify the advection transport mechanism in our observations?
3. Can infragravity waves suspend sediment, and if so, in what way?

### 4.2 Field Site

The field study was conducted on the southern flank of the Sandmotor (Figure 4.1), a 20 million m<sup>3</sup> sand nourishment, close to The Hague, The Netherlands, during September 14 – October 24, 2014. The site was located on a moderately steep sloping (1:30), roughly N-S oriented beach with an average grainsize of 403  $\mu\text{m}$ . The area is characterized by a semi-diurnal tidal cycle with spring and neap tidal ranges of 1.5 and 0.8 m respectively. The site is exposed to the North Sea, waves generally range from 0.5 m during calm conditions and 2 m during more energetic conditions. Wave breaking ranged from spilling to mildly plunging.

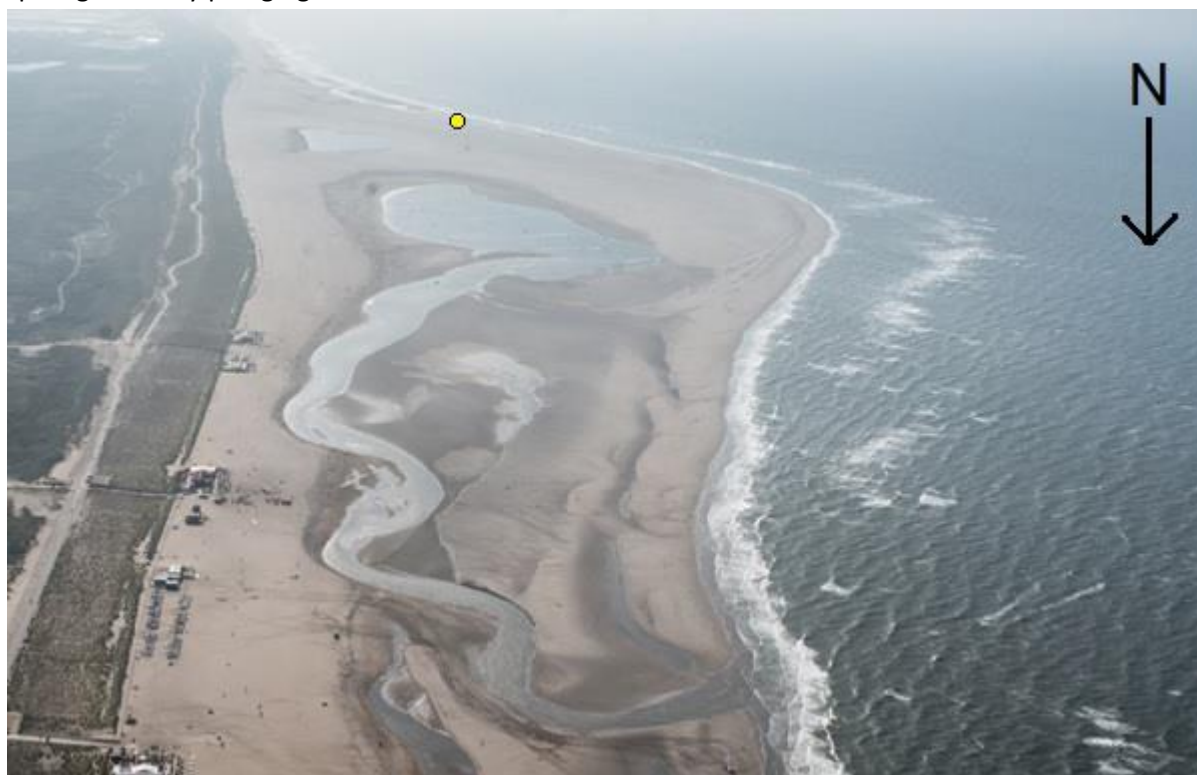


Figure 4.1: Aerial photograph of the Sandmotor (looking towards the south), September 13<sup>th</sup> 2014. Yellow dot indicates the approximate position of the cross-shore transect. ([www.zandmotor.nl](http://www.zandmotor.nl))

### 4.3 Instrumentation

During a six-week field campaign in The Netherlands, instruments were placed along a cross-shore oriented transect on the southern flank of the Sandmotor (Figure 4.2). The transect is located between

the low ( $\sim -0.5$  m below MSL) and high ( $\sim 1$  m above MSL) water lines, 9 OSSIs (Ocean Sensor System Inc., pressure sensors) were distributed along the cross-shore transect that sampled at a frequency of 5 Hz. OSS11 is located at  $x = 0$ , positive values towards the sea. Three Mini-Frames were each equipped with three Optical Backscatter Sensors (OBS) to measure suspended sediment concentration, a Pressure Transducer (PT) to estimate the sea-surface elevation from pressure below the waves and an ElectroMagnetic Flow meter (EMF) to measure the flow velocity in both cross-shore and alongshore direction. Each instrument measured at a frequency of 4 Hz. A large frame, the Truc Vert frame, was equipped with one PT, five OBS's, along with three Sontek Acoustic Doppler Velocimeters (ADV, sampling frequency of 10 Hz) that measure flow velocity in three directions, and a Ripple scanner to scan bedforms. Measurements were carried out 24 hours a day as long as the equipment was below the water surface. Data was electronically logged.

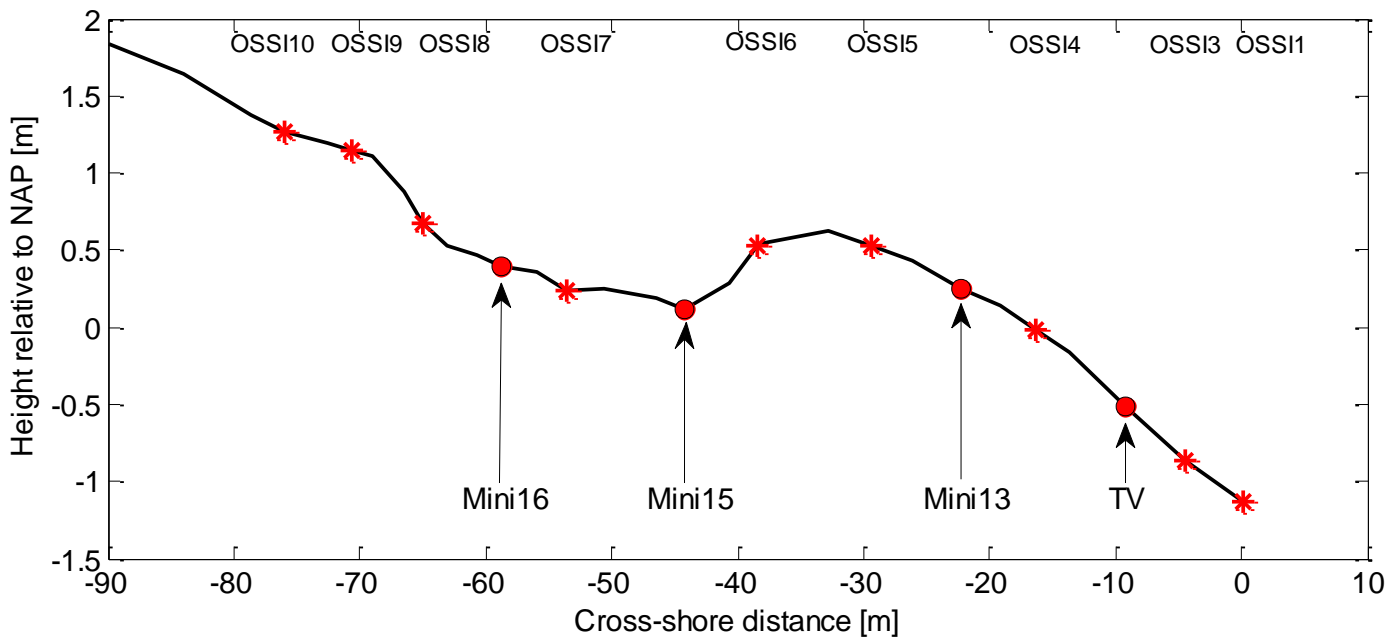


Figure 4.2: Cross-shore profile with locations of the Instruments at the start of the field campaign, 09-17-2014.

The instrument height above the bed was measured each day and adjusted when needed. At each low-tide EMF meters at the Mini-Frames were re-positioned to around 15 cm above the bed, the three OBS's at 3 cm, 9 cm and 15 cm above the bed and the PT at 9 cm above the bed. The relative position of all instruments to one another was kept constant. At the Truc Vert frame the same instrument heights were aimed for, however large fluctuations occurred due to large erosion events. The instrument heights are linearly interpolated between each measurement to simulate the evolution of the bed profile along one tidal cycle.

The bottom topography around the transect (approximately 200 m south and 200 m north of the transect) was mapped a few times per week using a Differential Global Positioning System (DGPS) mounted on a quad. The morphological change along the transect was monitored daily with DGPS measurements. A grid of about 500 x 500 m was monitored using Argus imaging at a sampling frequency of 2 Hz. Offshore data is available from a buoy 800 m offshore in 11 m water depth at the head of the Sandmotor.

#### 4.4 Offshore wave conditions

Overall, conditions were gentle during the field campaign with mean significant wave height ( $H_{m0}$ )  $\sim 0.65$  m, and a peak period ( $T_{m0}$ )  $\sim 4$  s. Also several higher energetic events were measured, including

a storm with a surge level of 1.7 m,  $H_{m0} \sim 4.3$  m and  $T_{m0} \sim 7$  s. Corresponding infragravity-wave heights over the array were in general around  $H_{ig} \sim 0.1-0.2$  m and reached up to  $H_{ig} \sim 0.45$  m during the storm. The offshore wave angle of incidence was relatively constant, ranging between  $270^\circ$  and  $360^\circ$  (Figure 4.3), thus coming from the north-west.

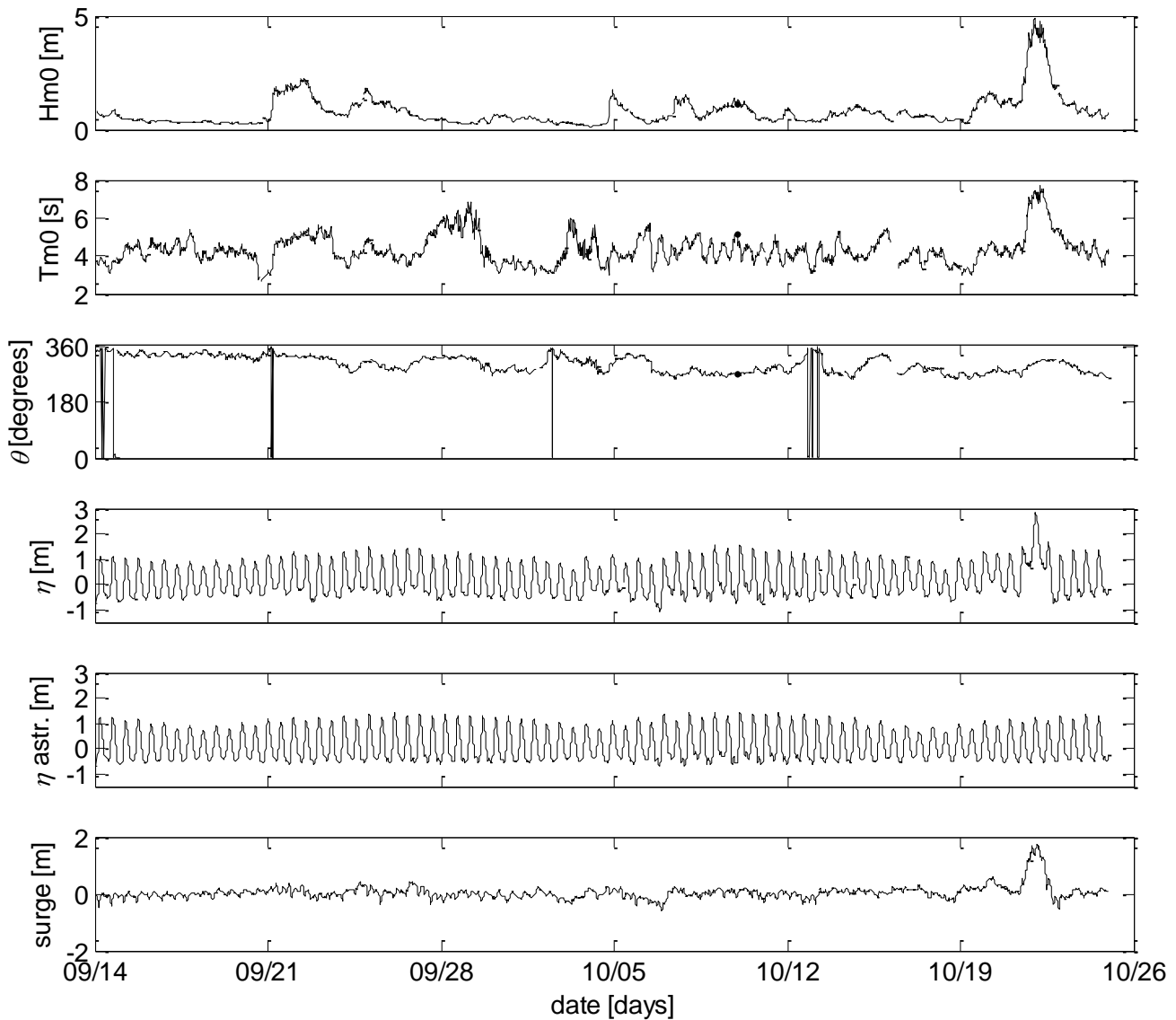


Figure 4.3: Offshore wave conditions and water levels during the field campaign. a) Significant wave height, b) significant wave period, c) angle of incidence, d) measured water level fluctuations, e) predicted water level fluctuations, f) measured surge, calculated by subtracting predicted from measured water levels. The time axis is the date in the year 2014.

Although conditions were gentle, morphological change was larger and faster than initially expected (Figure 4.4). The bar and trough system present at beginning of the campaign increased in height and moved landwards during the first two weeks, changing the morphological position of Mini-Frame 15 towards the crest of the sandbar. During October 5<sup>th</sup> and October 7<sup>th</sup>, higher energetic conditions were recorded. The small storm resulted in considerable flattening of the sandbar and narrowing of the trough. At this stage, all measurement rigs were on the top, or on the seaward side of the bar crest. After October 12<sup>th</sup> the bar- trough system disappeared and the bed had a constant slope along the transect. The storm did not alter the bed at the transect much, only at the most seaward section of the transect a considerable amount of sediment was deposited.

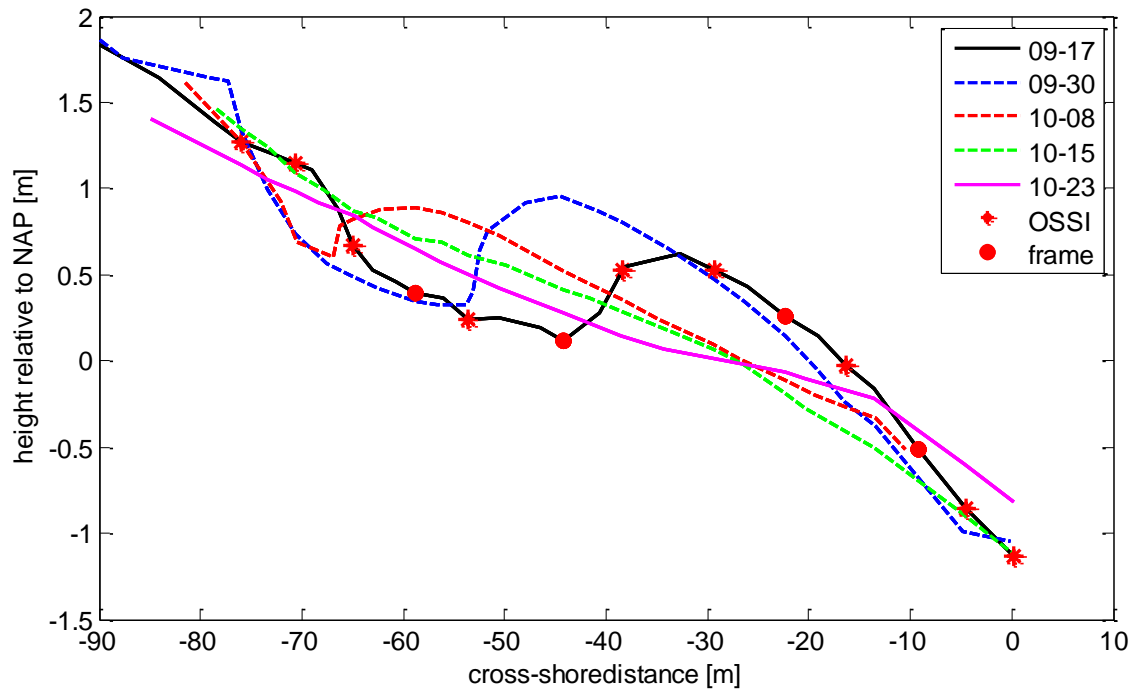


Figure 4.4: Morphological change along the transect during the field campaign, black line indicates the initial profile.

#### 4.5 Data selection and initial processing

Here initial data processing and data selection will be discussed. More detailed processing methods and calculations are discussed in their associated chapters or have already been described in the literature part.

The tidal signal is derived from the most seaward located PT (OSSI\_01), a frequency filter (set at an upper boundary of 0.002 Hz and a lower boundary of 0 Hz) is used to filter out the tidal signal and to determine when high tide occurred (Figure 4.5). In total, 73 high tides were recorded. The filter also identified two high water levels during one low tide, this particular low tide occurred during storm conditions and is included in the data set.

The data selection procedure was based upon data availability, stationarity and wave characteristics. First, 75 two-hour time series around high tide from the tidal signal at OSSI\_01 were created. High-tide sequences are chosen because conditions can assumed to be stationary in comparison to rising or falling water levels. Furthermore, this allows us to observe processes in the shoaling- and surf zone, depending on the offshore wave conditions. A data check was carried out to verify whether most of the instruments measured and gave a reliable signal during the tidal sequence. The entire two-hour time series was removed if the data showed any intermittently dry and wet conditions. Suspended sediment concentration signals are manually checked for the presence of bubbles. When a bubble was identified, an unrealistically sharply peaked high concentration event exceeding  $\sim 120 \text{ kg m}^{-3}$ , the data series was removed. Mini-Frame 16 did not pass the checks for most high tides as instruments were only submerged for a period of two hours around spring tide or during high surge, and because most of signals showed bubbles at the beginning of the time-series. Above mentioned checks reduced the dataset from 75 to 24 useable high tides (Table 4-1), this data set will be referred to as the bulk data set.

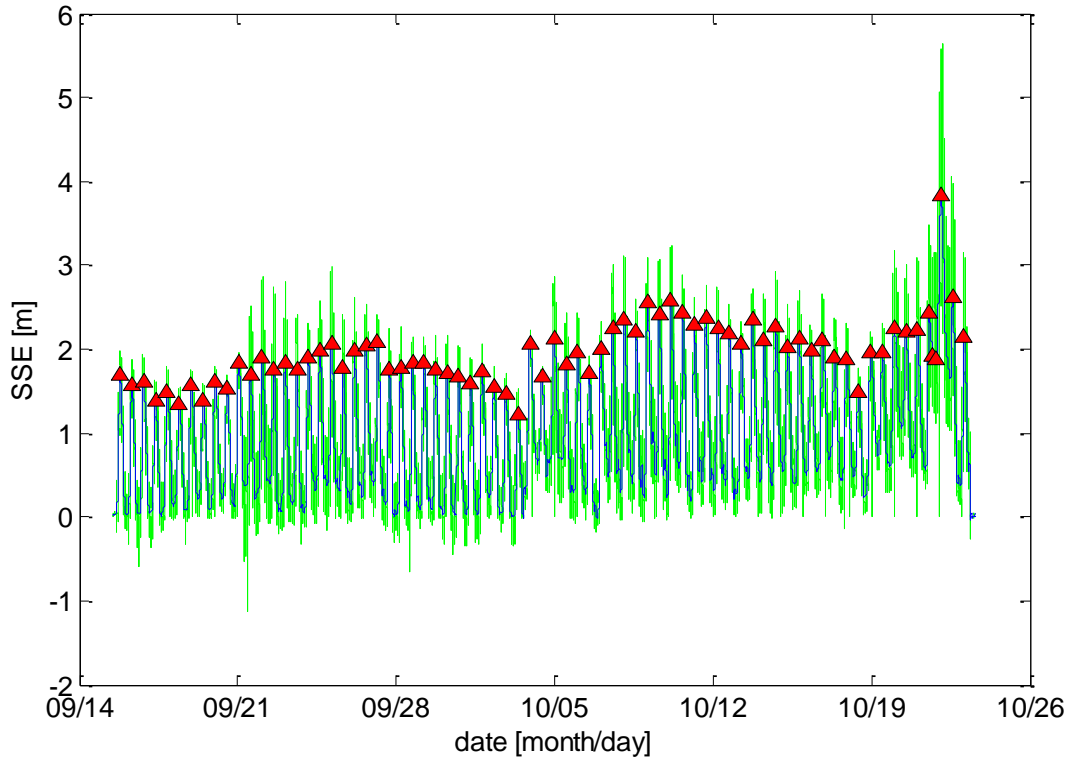


Figure 4.5: Tidal signal during the field campaign at OSSI\_01, in green: pressure signal measured by OSSI, in blue: tidal signal and triangles denote high tide.

Table 4-1: Bulk data-set.

Tide nr.	Bulk nr.	Date	Tide nr.	Bulk nr.	Date	Tide nr.	Bulk nr.	Date
3	1	09/16	49	9	10/10	62	17	10/17
19	2	09/25	52	10	10/12	66	18	10/19
20	3	09/25	55	11	10/13	67	19	10/20
22	4	09/26	56	12	10/14	68	20	10/20
23	5	09/27	57	13	10/14	69	21	10/21
26	6	09/28	58	14	10/15	71	22	10/21
46	7	10/09	59	15	10/15	72	23	10/21
48	8	10/10	61	16	10/16	73	24	10/22

For the bulk data set, sea-surface elevation above the bed is calculated by applying linear wave theory to the corrected pressure signal plus adding the instrument height above the bed. Water depths ( $h$ ) are calculated as the mean of the sea surface elevation. Background suspended sediment concentration signals or “field offset” was filtered out. Background concentration was defined as the one percentile (99% percent of all the measured suspended sediment concentrations are higher than the one percentile value) of the sediment concentration for a window of 90 seconds. The one-percentile value is subtracted from the measured suspended sediment concentration value, obtained negative values are set to zero.

Data was filtered into high (0.05 – 1 Hz) sea-swell and low (0.005-0.05 Hz) infragravity frequencies. Wave energy spectra were calculated, with a block size of 600 data points (2.5 minutes) resulting in 95 blocks with a 50% overlap and 240 degrees of freedom with a frequency resolution of 1/150. Each

block was tapered with a Hamming window of the same length, 95% confidence intervals ranged from 0.84 to 1.21. Wave heights were calculated as,

$$Hm_0 = 4\sqrt{m_0}$$

with  $m_0$  as the zeroth moment of the energy spectra. Figure 4.6 shows an overview of the bulk data set, the top panel shows infragravity wave height ( $Hm_{0inf}$ ), the ratio between infragravity waves and sea-swell waves ( $Hm_{0inf}/Hm_{0hf}$ ) and the ratio between the longshore and cross-shore current (Ratio VU). Significant infragravity-wave height ranged between 0.06 – 0.45 meter. The general trend is that large infragravity waves occur when the longshore current is strong, with the exception of tide number 23. Tide 23 is not a high tide but small peaks in water level at low tide during storm conditions. The bottom panel shows the instrument height of the lowest OBS during high tide of each tide, the other two OBS's were positioned 6 and 12 cm higher respectively.

Four representative tides were selected from the bulk data set (Table 4-2) to be examined more closely. Tide selection was based on STM height (at least one STM of each Mini-Frame has to be at 3 – 7 cm above the bottom) and shear wave contribution. Shear wave contribution to the total velocity field in the infragravity band during the four selected tides did not exceed 50% (not shown). Shear wave contribution has been determined following the method described in Lippmann et al. (1999). Initially it was aimed for that also the ratio between longshore- and cross-shore velocity should not be greater than 0.5, however due to the severe limitation of the data set using this criteria, this was dropped.

Table 4-2: Selected tides

Tide / bulk nr.	Date
52 / 10	12 Oct 2014
56 / 12	14 Oct 2014
62 / 17	17 Oct 2014
72 / 23	21 Oct 2014

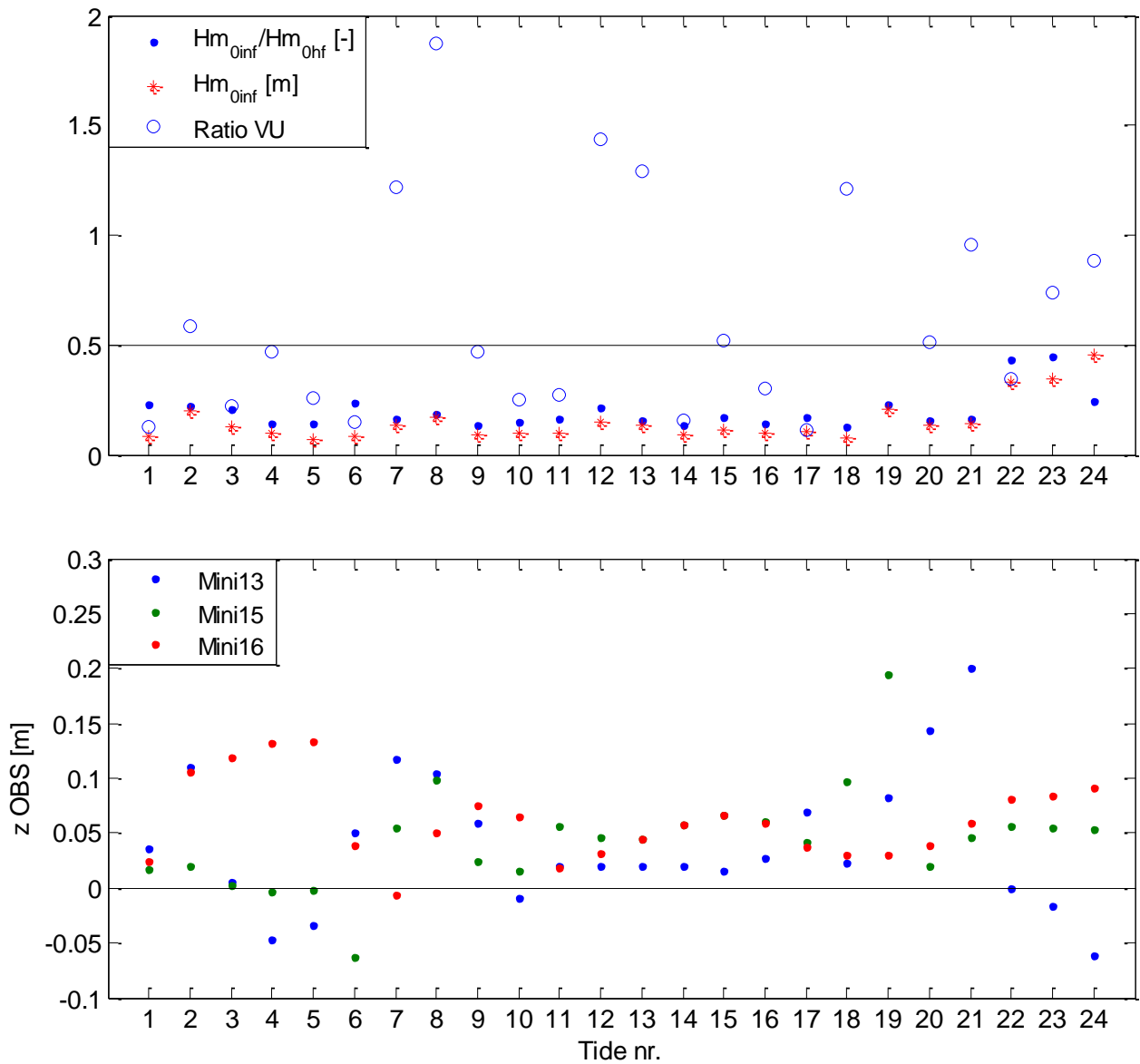


Figure 4.6: Overview of the bulk data set. The top panel shows 1) ratio between infragravity wave height and sea-swell wave height (blue dot), 2) infragravity wave height (red star), 3) ratio between longshore and cross-shore velocity. The bottom panel shows OBS height of the lowest OBS at the three Mini-Frames.

## 5. Results

Here the results of both the bulk data set and the four individual cases are presented. Section 5.1 gives an overview of the characteristics of the bulk data set and the four selected cases. Section 5.2 present the results on the sediment suspension and transport associated with sea-swell, infragravity waves and mean currents.

### 5.1 Hydrodynamics

#### Infragravity wave height

At all locations the significant infragravity-wave height shows a good correlation ( $R^2 = 0.94$ ) with offshore significant sea-swell wave height (Figure 5.1a), and is  $\sim 10\text{-}15\%$  of  $H_{m0}$ . In the onshore direction, the infragravity wave becomes relatively more important (Figure 5.1b).

The following three tables give an overview of the offshore wave conditions (Table 5-1) and conditions at Mini-Frame 13 (Table 5-2) and Mini-Frame 15 (Table 5-3) during the four selected cases.

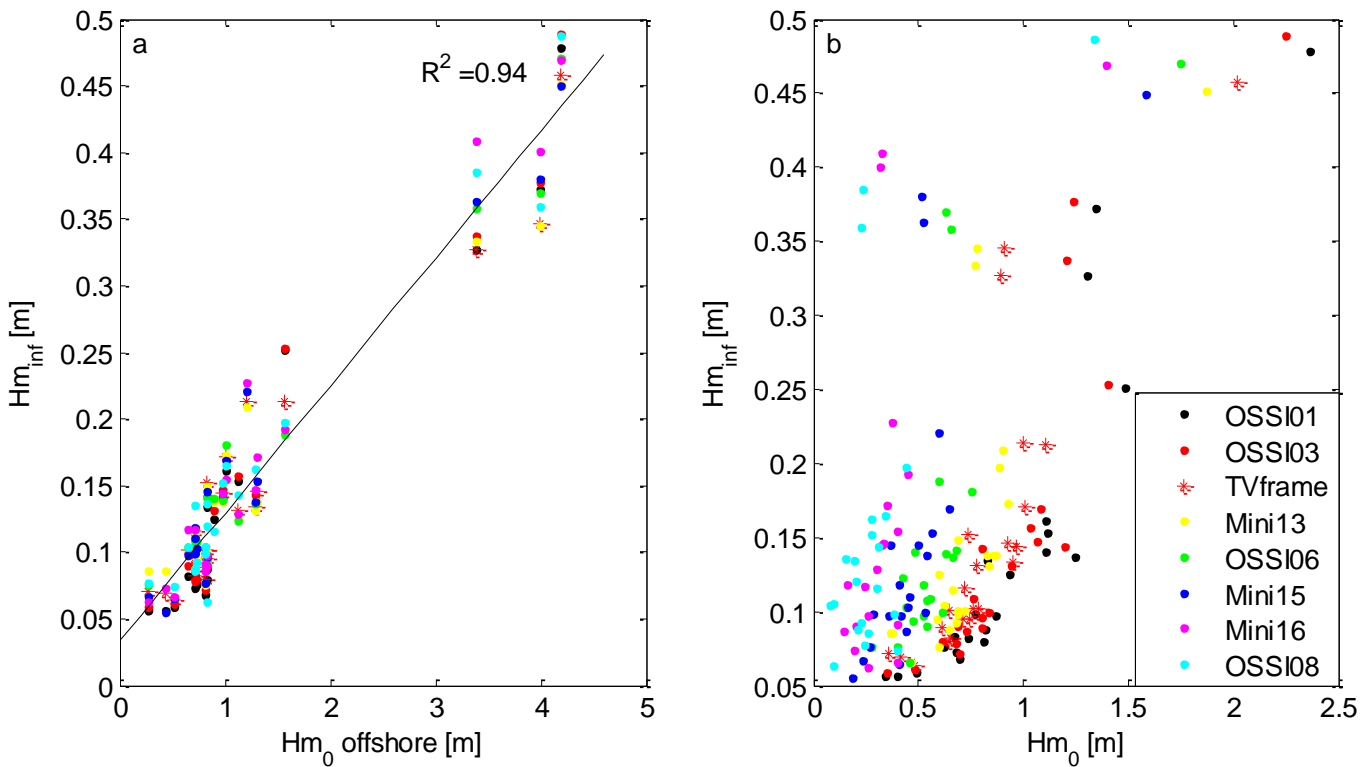


Figure 5.1: a) Infragravity-wave height plotted against offshore significant sea-swell wave height, b) infragravity-wave height plotted against sea-swell wave height at the location of the instrument.

Table 5-1: Offshore conditions during the four selected cases.

Tide bulk nr.	10	12	17	23
Significant sea-swell wave height ( $H_{hf}$ ) [m]	0.72	0.80	0.64	3.99
Peak period ( $T$ ) [s]	3.94	4.33	3.27	6.9
Angle of incidence [ $^{\circ}$ ]	294	270	291	301

Table 5-2: Conditions during the four selected cases at Mini-Frame 13.

Tide	10	12	17	23
Significant sea-swell wave height ( $H_{hf}$ ) [m]	0.69	0.68	0.61	0.77
Infragravity wave height ( $H_{ig}$ ) [m]	0.10	0.15	0.10	0.35
Relative wave height ( $H_{hf} h^{-1}$ ) [-]	0.55	0.61	0.60	0.66
Slope [m/m]	1:30	1:33	1:35	1:33
Angle of incidence [°] + = north, - = south	3.84	13.9	-0.78	0.47
r0 [-]	-0.46	-0.33	-0.35	0.26

Table 5-3: Conditions during the four selected cases at Mini-Frame 15

Tide / bulk nr.	10	12	17	23
Significant sea-swell wave height ( $H_{hf}$ ) [m]	0.46	0.37	0.29	0.51
Infragravity wave height ( $H_{ig}$ ) [m]	0.11	0.15	0.10	0.40
Relative wave height ( $H_{hf} h^{-1}$ ) [-]	0.61	0.54	0.51	0.70
Slope [m/m]	1:30	1:33	1:35	1:33
Angle of incidence [°] + = north, - = south	-1.6	-1.9	-4.3	-5.2
r0 [-]	-0.04	0.27	0.28	0.29

### Wave energy

Wave-energy spectra of the observed time-series are shown for the four selected cases at four locations along the cross-shore in Figure 5.2. Tide 10 has relatively low-energy conditions, tide 12 and 17 have about similar moderate energy conditions and tide 23 has higher energy conditions. Tide 12, 17 and 23 show one clear peak in the sea-swell frequency band. Tide 10 shows two distinct peaks, the lower frequency peak are swell-waves and the higher frequency are sea-waves (wind). Energy in the sea-swell frequency bands decreases in the onshore direction and infragravity wave energy becomes increasingly more important.

The location where sea-swell waves break highly depends on the slope of the bed and occurs at a certain relative wave height. However, the exact relation between bed slope and wave breaking is still unknown. Ruessink (1998) observed that at a low sloping (< 1:50) beach where most of the sea-swell waves start to break or are already breaking, the relative wave height is  $\sim 0.33$ . Houser and Greenwood (2005) on the other hand observe this when relative wave height is  $\sim 0.4$  (bed slope 1:110). Figure 5.3 shows the relation between the cross-correlation ( $r_0$ ) between sea-swell wave envelope and the infragravity-wave and the relative significant sea-swell wave height ( $H_s h^{-1}$ ). When  $r_0$  is negative, the infragravity-wave can be considered as bound to the sea-swell wave groups; high (low) sea-swell waves are present in the trough (crest) of the infragravity wave. Upon breaking of the sea-swell waves this correlation becomes positive and high (low) sea-swell waves are present in the crest (trough) of the infragravity-wave; infragravity-waves are free. At a relative wave height of  $\sim 0.48$  correlation changes rapidly towards a more positive value, presumably a large part of the sea-swell waves start

to break. The highest sea-swell waves probably already started to break earlier. The  $r_0$  value gives a good estimation of the relative position in the coastal regime of the considered instruments. In general  $r_0$  is negative in the shoaling zone and the first part of the surf zone and becomes increasingly more positive in the onshore direction. However, when in very shallow water smaller sea-swell waves at the crest of the infragravity wave also start to break, the correlation shifts towards 0 again. When not looked at carefully, one might assume this is at a more offshore position while the location is actually well within the surf zone or close to the swash zone.

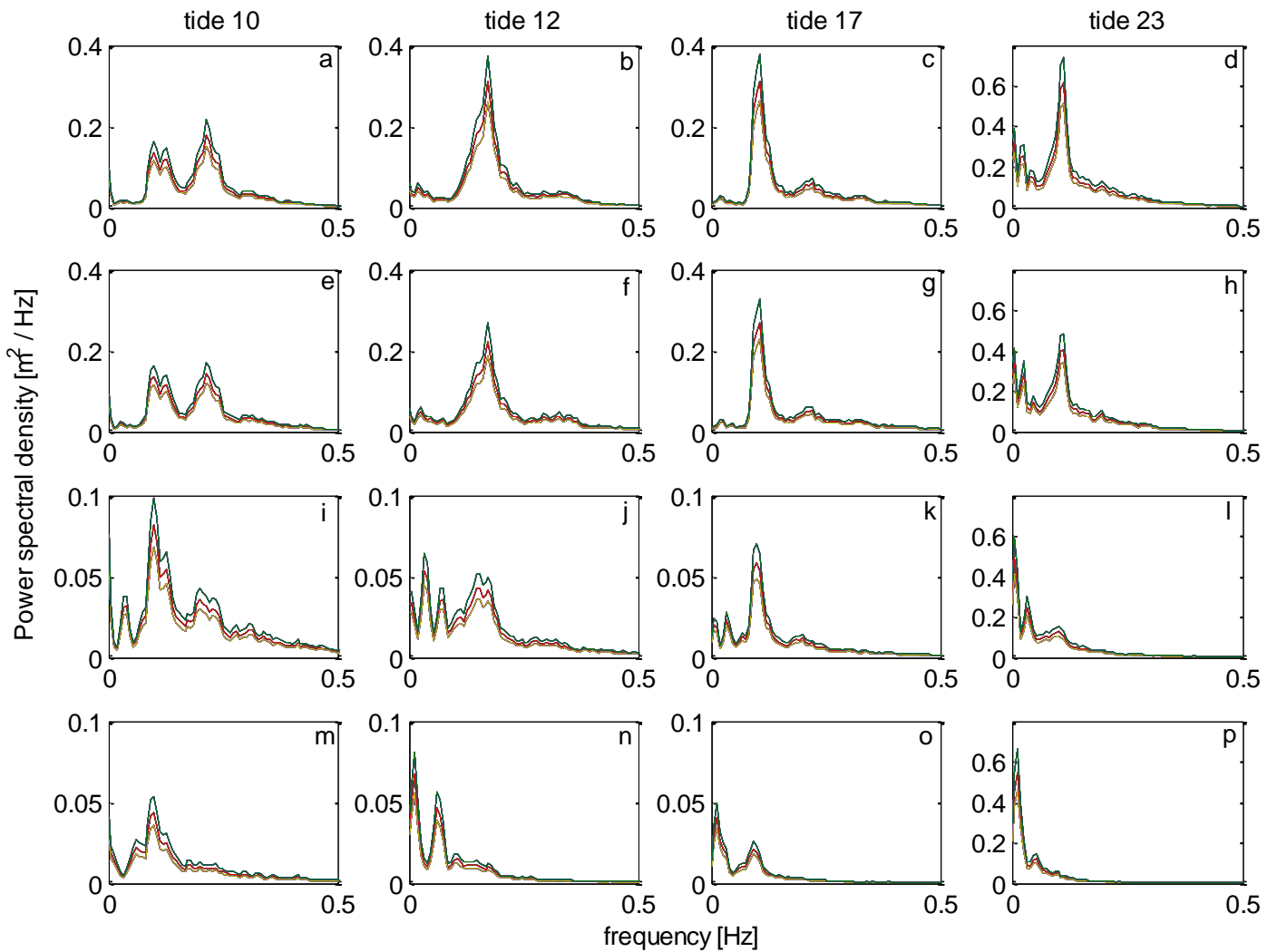


Figure 5.2: Power spectra for the selected cases with 95% confidence belts. a-d) Truce Vert Frame, e-h) Mini-Frame 13, i-l) Mini-Frame 15 and m-o) Mini-Frame 16. Please note the varying scales on the y-axis.

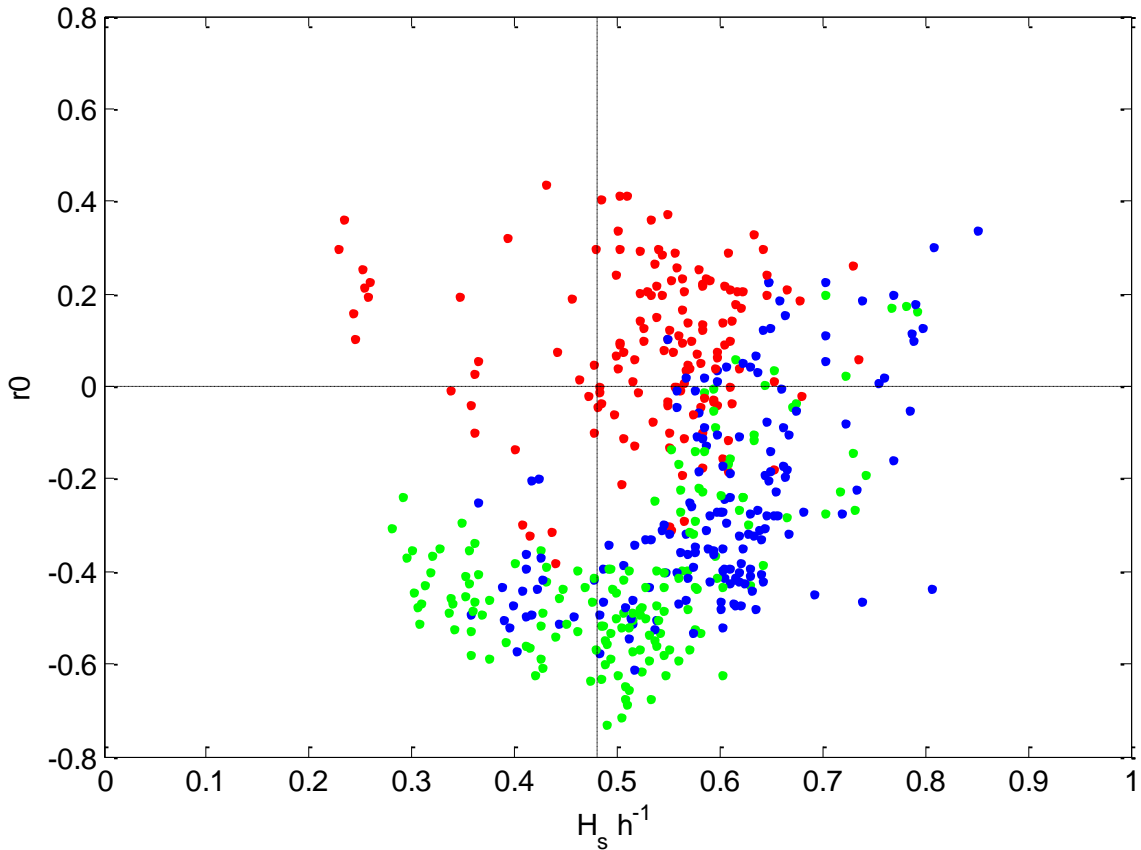


Figure 5.3 Correlation between sea-swell wave envelope and infragravity waves plotted against significant relative wave height at Truc Vert (green), Mini-Frame 13 (blue) and Mini-Frame 15 (red).

#### **Cross-shore development of Skewness, asymmetry**

Figure 5.4 shows the development of skewness and asymmetry of sea-swell waves and infragravity waves in the cross-shore direction for the four selected cases. Sea-swell wave shape develops as expected; skewness increases in the shoaling zone and decreases in the onshore direction (Figure 5.4 top panels) while sea-swell waves become increasingly more asymmetric in the onshore direction (Figure 5.4 panels in the second row). Infragravity-wave skewness increases slightly in the onshore direction, especially at -50 m and -60 m marks. During tide 10 and 12 infragravity waves are negatively skewed between 0 m and -10 m which increases towards positive skewness in onshore direction just as sea-swell waves. Infragravity-wave asymmetry remains relatively constant along the transect and seems to decrease close to the shore for tide 10, 12 and 23. Mini-Frame 16 is located at the -60 mark, however not much reliable data is present in the bulk data-set to be able to make a clear distinction whether infragravity wave skewness and asymmetry have a pronounced effect on sediment transport direction close to the shore. Furthermore because skewness and asymmetry of infragravity waves are practically the same at Mini-Frame 13 (-22 m) and 15 (-45 m).

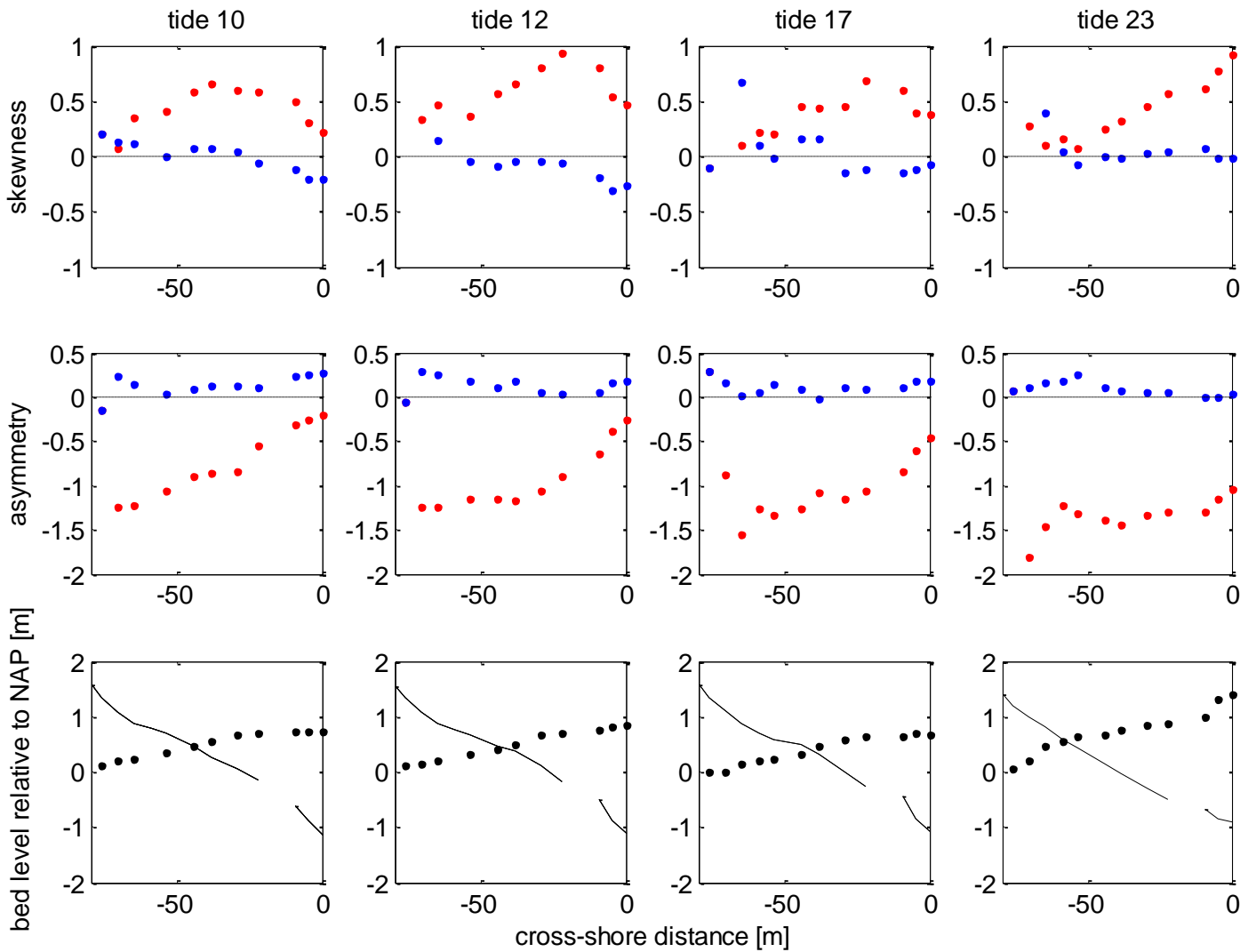


Figure 5.4: Development of skewness and asymmetry in the cross-shore direction, red: sea-swell waves, blue: infragravity waves and black dots:  $H_{m0}$  [m].

To estimate in whether the two Mini-Frames are located in the shoaling or the surf zone during the selected cases the cross-shore development of the energy flux using the Battjes-Janssen (1974) model has been calculated (Figure 5.5). The seaward boundary of the surf zone has been determined at 85% of the offshore incident energy following Thomson et al (2006).

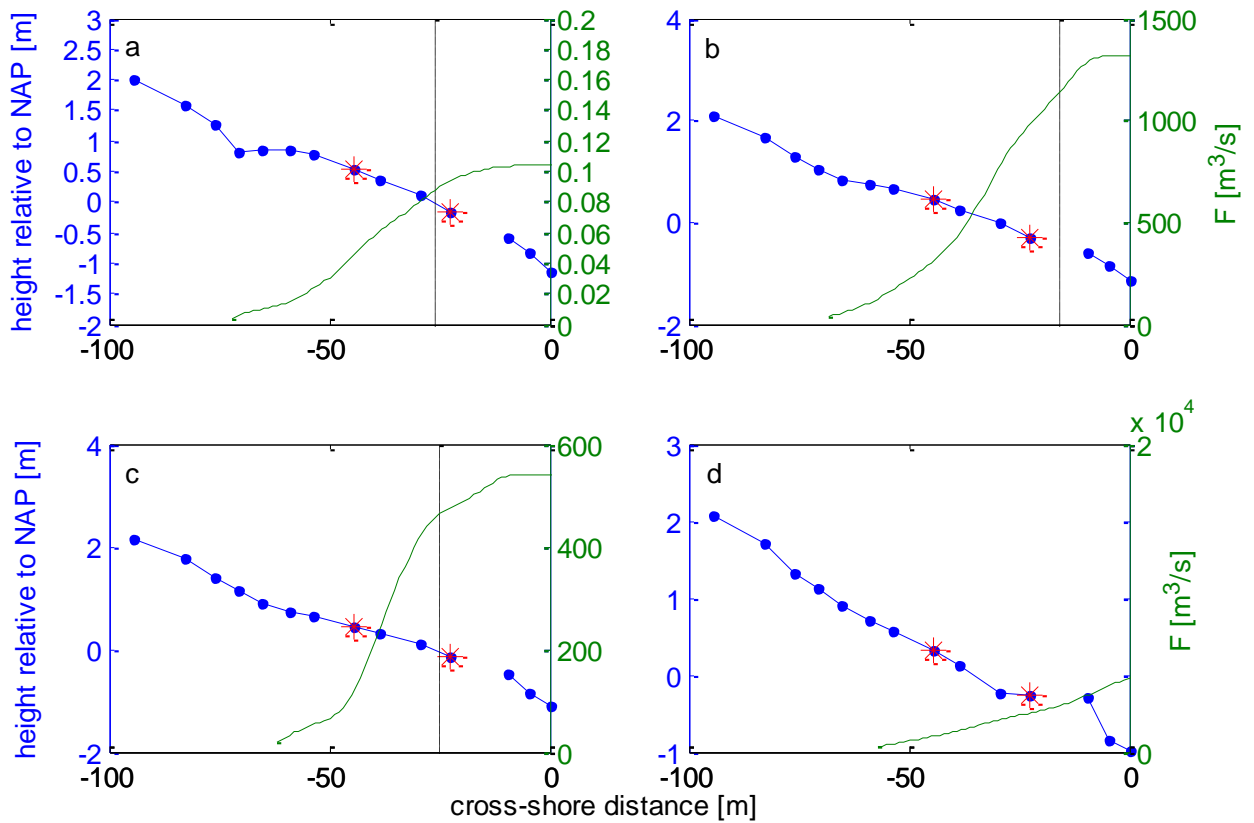


Figure 5.5: Energy flux along the cross-shore transect. Blue line and dots are the cross-shore profile and instruments. Red stars are Mini-frame 15 and 13. Vertical dashed line is the estimated location where the surf zone starts. a) tide 10, b) tide 12, c) tide 17, d) tide 23.

## 5.2 Sediment transport

### Sediment transport components

Sediment transport is calculated with time-series of suspended sediment concentration and flow velocities for the bulk data set, using the method described in section 3.1. The two hours around each high tide are divided into blocks of 15 minutes for which sediment transport is calculated for the different components; mean transport and oscillatory transport. Oscillatory transport consists of high-frequency sea-swell sediment transport and low-frequency infragravity-wave sediment transport. Values for averaged suspended sediment transport by the different transporting components for Mini-Frame 13, 15 and 16 are plotted as a function of relative wave height ( $H_s h^{-1}$ ) are plotted in figure 5.6. Wave height for the 15-minute block is defined as four times the standard deviation of the high frequency sea-surface elevation.

$$H_s = 4 * \sigma(\eta)$$

The Truc Vert frame is not included, as most of the time the lowest OBS is not at the desired height of 3-7 cm above the bed. Comparisons with the three Mini-Frames are therefore not reliable as suspended sediment concentration signals are highly dependent on height above the bed (e.g. Huntley and Hanes, 1987).

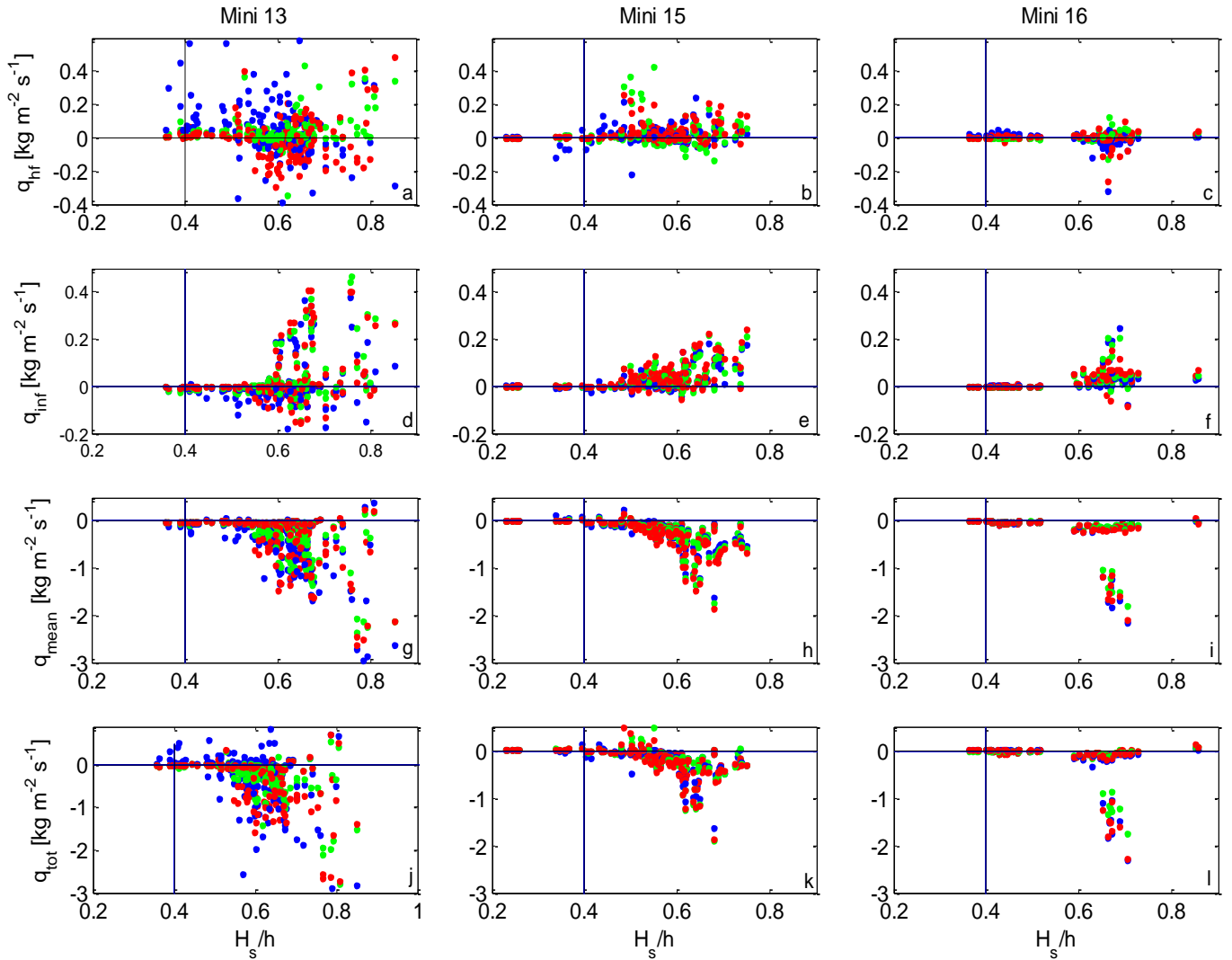


Figure 5.6: 15-minute averaged suspended sediment transport for the bulk data set for the different sediment transport components: a,b,c) transport by sea-swell waves, d,e,f) transport by infragravity waves, g,h,i) transport by the mean current and j,k,l) total sediment transport, relative to local relative significant wave height ( $H_s/h$ ) at Mini-Frame 13, 15 and 16. Blue dots, lowest OBS, green dots, middle OBS and red dots highest OBS. Positive is onshore directed, also note the differing scales between each component.

Sediment transport by infragravity waves ( $q_{ig}$ ) has the same order of magnitude as sediment transport by sea-swell waves ( $q_{hf}$ ) while mean current sediment transport ( $q_{mean}$ ) is dominant over the oscillating components (Figure 5.6). An increase in sediment transport for both infragravity and the mean component can be seen at  $H_s h^{-1} \sim 0.55$ . At this point it is expected that most of the sea-swell waves start to break and subsequently stir up sediment from the bed. Sea-swell wave sediment transport is predominantly onshore directed for both Mini-Frame 13 and 15 (Figure 5.6a, b). At Mini-Frame 13 offshore transport occurs at the highest OBS (red dots), this might be due to the time it takes for sediment to reach higher up in the water column and the flow is close to flow reversal, by which sediment at the height of the highest OBS is transported during the offshore phase of a sea-swell wave. At Mini-Frame 16 sea-swell wave sediment transport is small because most of the energy in this frequency band has already been dissipated (Figure 5.6c). During high energy conditions, sediment transport due to sea-swell waves has the same order of magnitude as during low/medium energetic conditions, which might be because the relative wave height is the same during all measured conditions and most sea-swell waves already lost energy due to wave breaking further offshore.

Infragravity-wave sediment transport increases at a relative wave height of  $\sim 0.50$  (Figure 5.6d-f). Mini-Frames 15 and 16 show onshore directed infragravity wave transport while Mini-Frame 13 shows an offshore directed trend, until  $H_s h^{-1} \sim 0.60$ . The high onshore-directed infragravity-wave sediment transport at Mini-Frame 13 occurred during high energy conditions (Tide 2, 22, 23 and 24). Mean transport is offshore directed (Figure 5.6g-i) and is the main contributor to the total sediment transport (Figure 5.6j-l). Table 5-4 and 5-5 give an overview of the different transport components averaged over 2 hours for tide 10, 12, 17 and 23 for Mini-Frame 13 and 15.

Table 5-4: 2 hour averaged sediment transport rates by the different sediment transport components for Mini-Frame 13

Sediment transport [kg m <sup>-2</sup> s <sup>-1</sup> ]	Tide 10	Tide 12	Tide 17	Tide 23
<b>q<sub>tot</sub></b>	0.045	-0.092	0.005	-0.722
<b>q<sub>mean</sub></b>	-0.052	-0.084	-0.025	-1.050
<b>q<sub>hf</sub></b>	0.116	0.022	0.037	0.043
<b>q<sub>inf</sub></b>	-0.019	-0.030	-0.007	0.286

Table 5-5: 2 hour averaged sediment transport rates by the different sediment transport components for Mini-Frame 15

Sediment transport [kg m <sup>-2</sup> s <sup>-1</sup> ]	Tide 10	Tide 12	Tide 17	Tide 23
<b>q<sub>tot</sub></b>	-0.052	-0.113	0.058	-0.402
<b>q<sub>mean</sub></b>	-0.087	-0.172	-0.007	-0.559
<b>q<sub>hf</sub></b>	0.033	0.019	0.049	0.035
<b>q<sub>inf</sub></b>	0.00	0.040	0.018	0.121

### Sediment concentration and velocity signal

A more detailed view in to the suspension of sediment is given in the next four figures where in the top panels velocities of sea-swell waves (blue) and the infragravity waves (red) are shown. The lower panels show sediment concentration where high peaks in sediment concentration are cut-off to make the concentration signal clearer. Figure 5.7 shows the recorded signals of tide 12 at Mini-Frame 13. The  $r_0$  value is -0.33 and the infragravity-wave can be considered to be bound. Peaks in sediment concentration occur when there is a deep infragravity-wave trough with negative velocities up to  $\sim -0.5$  m/s. During smaller depressions no such peaks can be found. Sediment concentrations are high for a relatively long time period, similar to the time scale of infragravity waves. During the entire concentration signal small peaks are visible which seem to correspond more to a sea-swell wave period. Mini-Frame 13 is probably located in between the shoaling and surf zone (Figure 5.2f and 5.5b) where the largest sea-swell waves break. The likely stirring agent is the turbulence injected into the water column due to sea-swell wave breaking in the infragravity-wave trough, the relatively large infragravity-wave velocity might retain the sediment into suspension for a longer time period.

Figure 5.8 shows the same moment as figure 5.7 but then for Mini-Frame 15. Here the  $r_0$  is 0.27 and infragravity waves can be considered as free. The infragravity-wave signal shows slightly larger amplitudes compared to Mini-Frame 13, the last two high velocity ( $-0.5$  m/s) events at Mini-frame 13 can be linked (by eye) to two infragravity wave troughs at Mini-Frame 15 (nr. 2 and 3 with nr. 2 and 4). Infragravity-wave trough nr. 1 at Mini-Frame 13 decreased considerably in amplitude at Mini-frame

15. No sediment concentration peaks are visible at every high infragravity-wave velocity event. Peaks in sediment concentrations seem to occur at large values of the sea-swell wave signal.

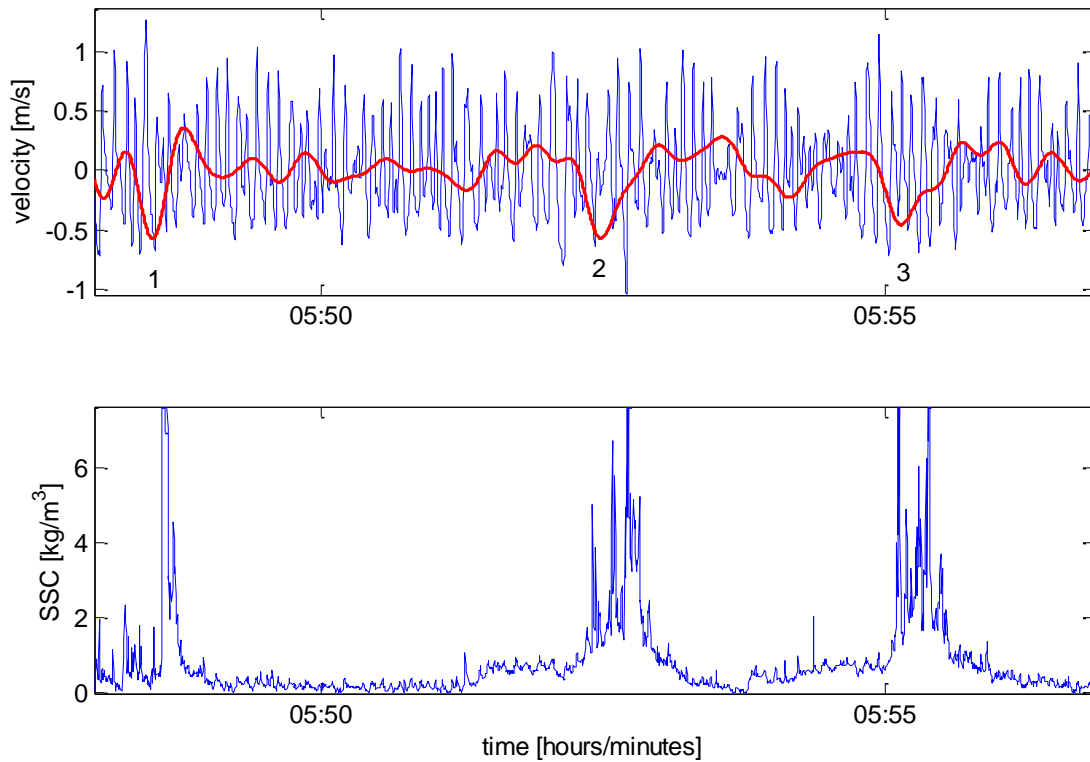


Figure 5.7: Time-series of cross-shore velocity for sea-swell waves (blue) and infragravity waves (red) (top panel) and suspended sediment concentration (bottom panel) at Mini-Frame 13 during tide 12.

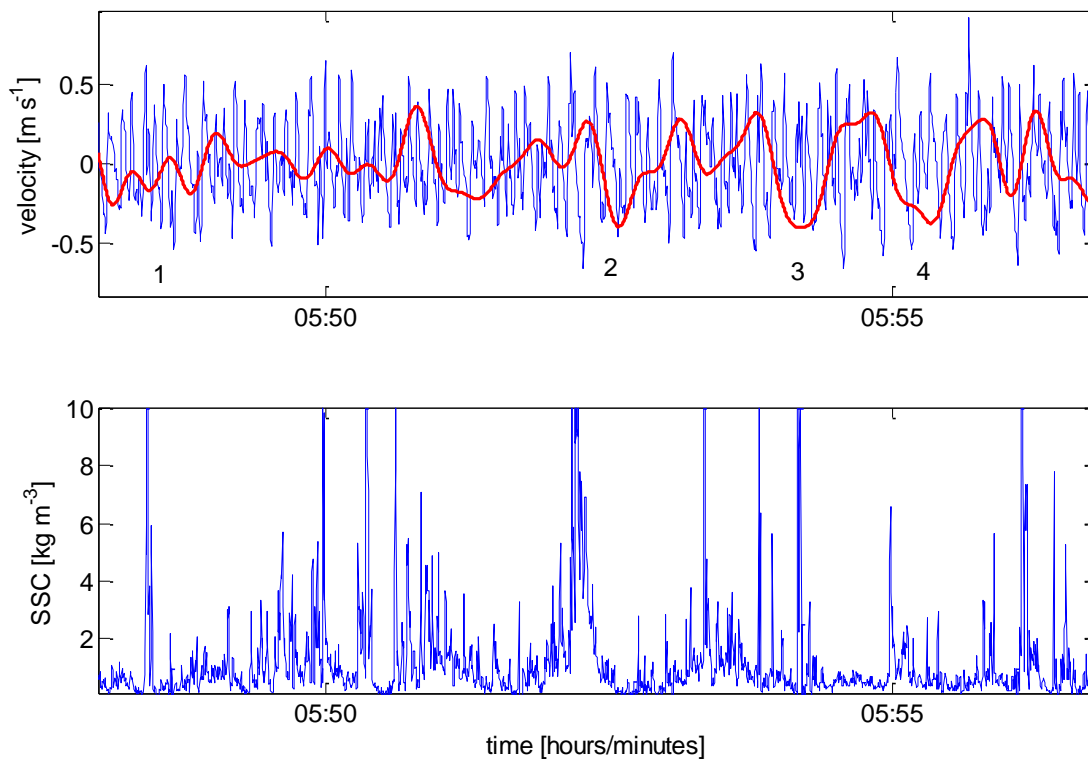


Figure 5.8: Time-series of cross-shore velocity for sea-swell waves (blue) and infragravity waves (red) (top panel) and suspended sediment concentration (bottom panel) at Mini-Frame 15 during tide 12.

Similar figures have been made for tide 17 at Mini-Frame 13 and 15 (Figure 5.9 and 5.10). Offshore conditions at Mini-Frame 13 are comparable to tide 12 (table 5-1 and 5-2). Sea-swell wave velocities have about the same magnitude as during tide 12, although infragravity-wave velocities are less. The  $r_0$  value is -0.35, the position in the coastal regime is on the boundary of the shoaling zone towards the surf zone (Figure 5.2g and 5.5). When looked at closely, suspension peaks do predominantly occur during negative infragravity-wave velocities but are less pronounced compared to tide 12. Also the concentration peaks are lower ( $\sim 2 \text{ kg m}^{-3}$ ) and elevated suspended sediment concentration events are shorter. Similar as in figure 5.7 small peaks can be seen in the concentration signal. These seem, again, to be caused by sea-swell waves and seem independent of infragravity-wave water level modulation as they occur in both phases of the infragravity-wave.

Figure 5.10 shows the same time series as figure 5.9 but then for Mini-Frame 15. Here the  $r_0$  value is 0.28, Mini-Frame 15 is located well within the surf zone. On average, sea-swell wave velocities are lower and infragravity-wave velocities are more or less the same. Sediment concentrations are higher at Mini-Frame 15 than at Mini-Frame 13. Again, there is no increased sediment concentration signal during the trough phase of the infragravity-wave, high sediment concentration peaks seem random.

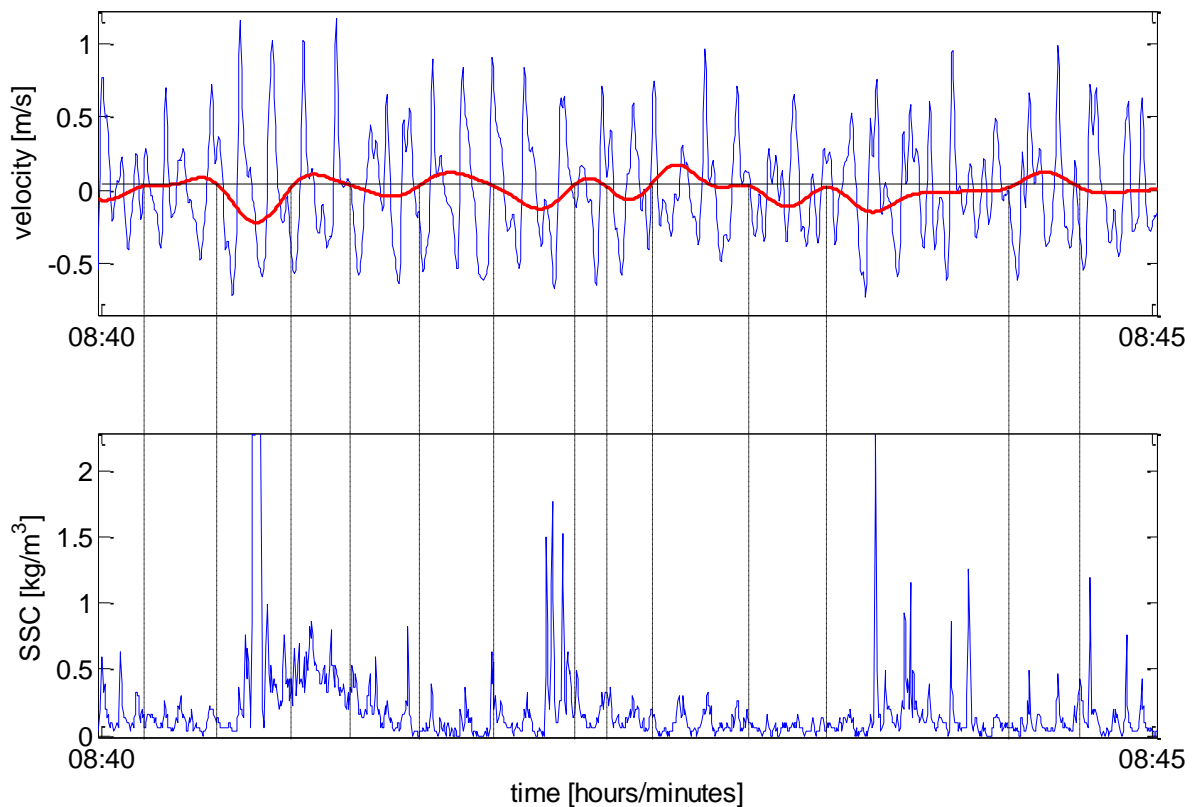


Figure 5.9: Time-series of cross-shore velocity for sea-swell waves (blue) and infragravity waves (red) (top panel) and suspended sediment concentration (bottom panel) at Mini-Frame 13 during tide 17. Dashed lines indicate flow reversals of the infragravity wave.

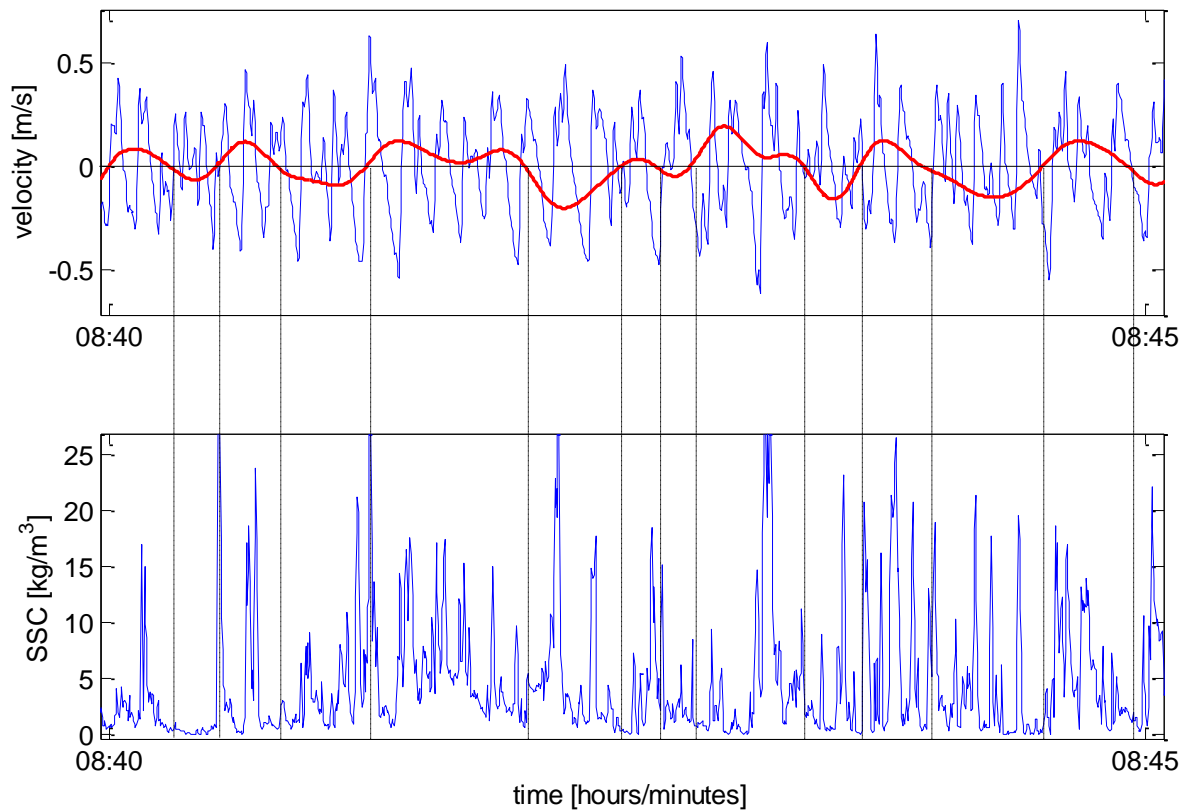


Figure 5.10: Time-series of cross-shore velocity for sea-swell waves (blue) and infragravity waves (red) (top panel) and suspended sediment concentration (bottom panel) at Mini-Frame 15 during tide 17. Dashed lines indicate flow reversals of the infragravity wave.

Figure 5.11 shows the sediment concentration at Mini-Frame 16 during tide 23. Here the top panel shows a pressure signal instead of a velocity signal because the latter one showed an intermittently wet and dry signal and reliable transport calculations cannot be made. The  $r_0$  value is 0.47, and Mini-Frame 16 is probably close to the swash zone. Here the sea-swell waves have the same order of magnitude as the infragravity-wave. Increased sediment concentrations are found during the trough of the infragravity wave while sea-swell waves are almost absent there. It is likely that the infragravity-wave itself is the stirring agent instead of breaking sea-swell waves.

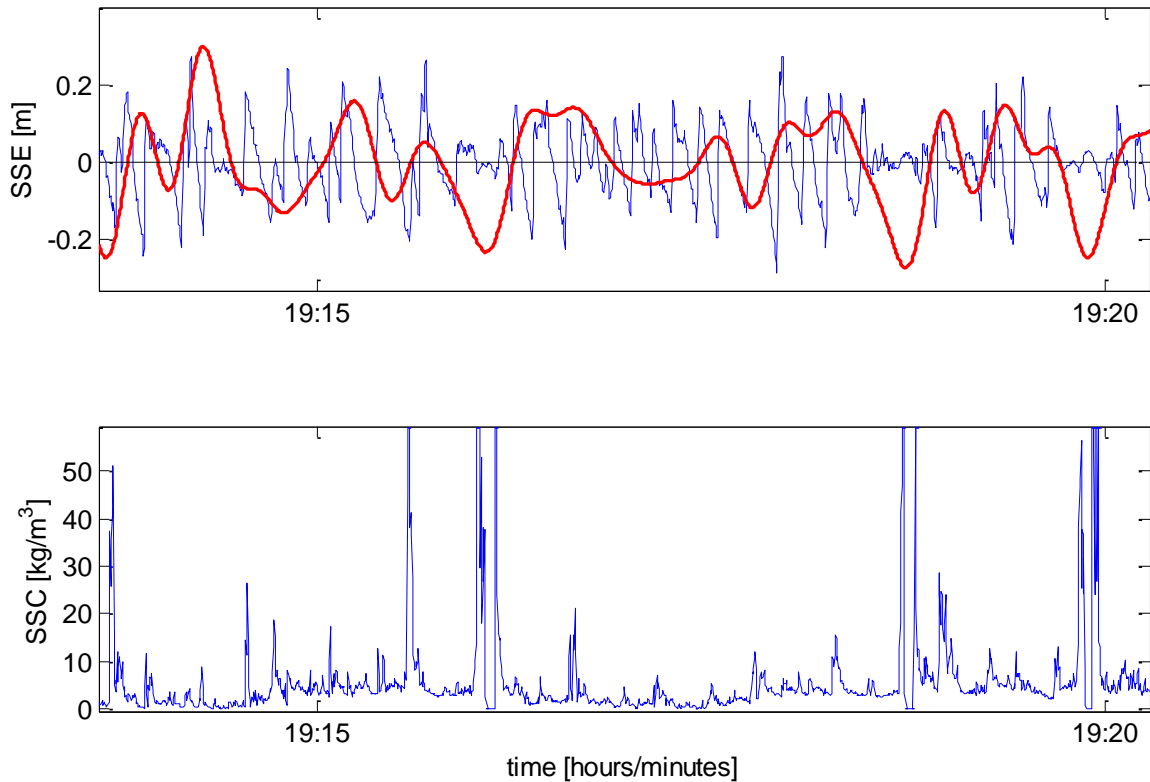


Figure 5.11: Time-series of sea surface elevation (SSE) for sea-swell waves (blue) and infragravity waves (red) (top panel) and suspended sediment concentration (bottom panel) at Mini-Frame 16 during tide 23.

### Power and co-spectra

In Figure 5.12 the power spectra of the velocity signal of Mini-Frame 13 and 15 are plotted together, these locations are selected because of the observed difference in transport direction by infragravity waves (Figure 5.6 d and e). Also the power spectra of the further offshore located Truc Vert Frame is added to observe any possible energy loss towards Mini-Frame 13.

During tide 10 (Figure 5.14a) two distinct peaks in the sea-swell regime, at  $\sim 0.11$  Hz and a higher harmonic at  $\sim 0.21$  Hz, are visible at Mini-Frame 13 and the Truc Vert Frame. The higher harmonic largely dissipated upon arrival at Mini-Frame 15. The primary peak has slightly decreased, while infragravity-wave energy has increased. As the power spectrum at the Truc-Vert frame is almost similar to the spectrum of Mini-Frame 13, this indicates that Mini-Frame 13 is probably just outside the surf zone, confirming the Battjes-Janssen model (Figure 5.5a). Mini-Frame 15 is well within the surf zone.

During tide 12 (Figure 5.12b) Mini-Frame 13 and Truc Vert Frame show similar spectra, with a peak at  $\sim 0.18$  Hz. The peak has again largely dissipated at Mini-Frame 15, while infragravity-wave energy has increased and now dominates.

Tide 17 (Figure 5.12c) shows the same trends as tide 12 with the difference that the spectrum is narrower and there is less energy in the infragravity band. Similar to tide 10, the frames are in the same coastal regime for both tide 12 and 17.

Tide 23 (Figure 5.12d) is a low tide during storm conditions. Most of the sea-swell wave energy already dissipated offshore before arriving at the Truc Vert Frame. Spectral peaks in sea-swell wave energy shifts towards a lower frequency which is about half of the original frequency. The remainder of the sea-swell wave energy dissipates between Mini-Frame 13 and 15. Infragravity waves are

dominant over sea-swell waves and gain some energy towards Mini-Frame 15. The spectral peak in infragravity wave energy slightly shifted towards a higher frequency from Mini-frame 13 towards 15.

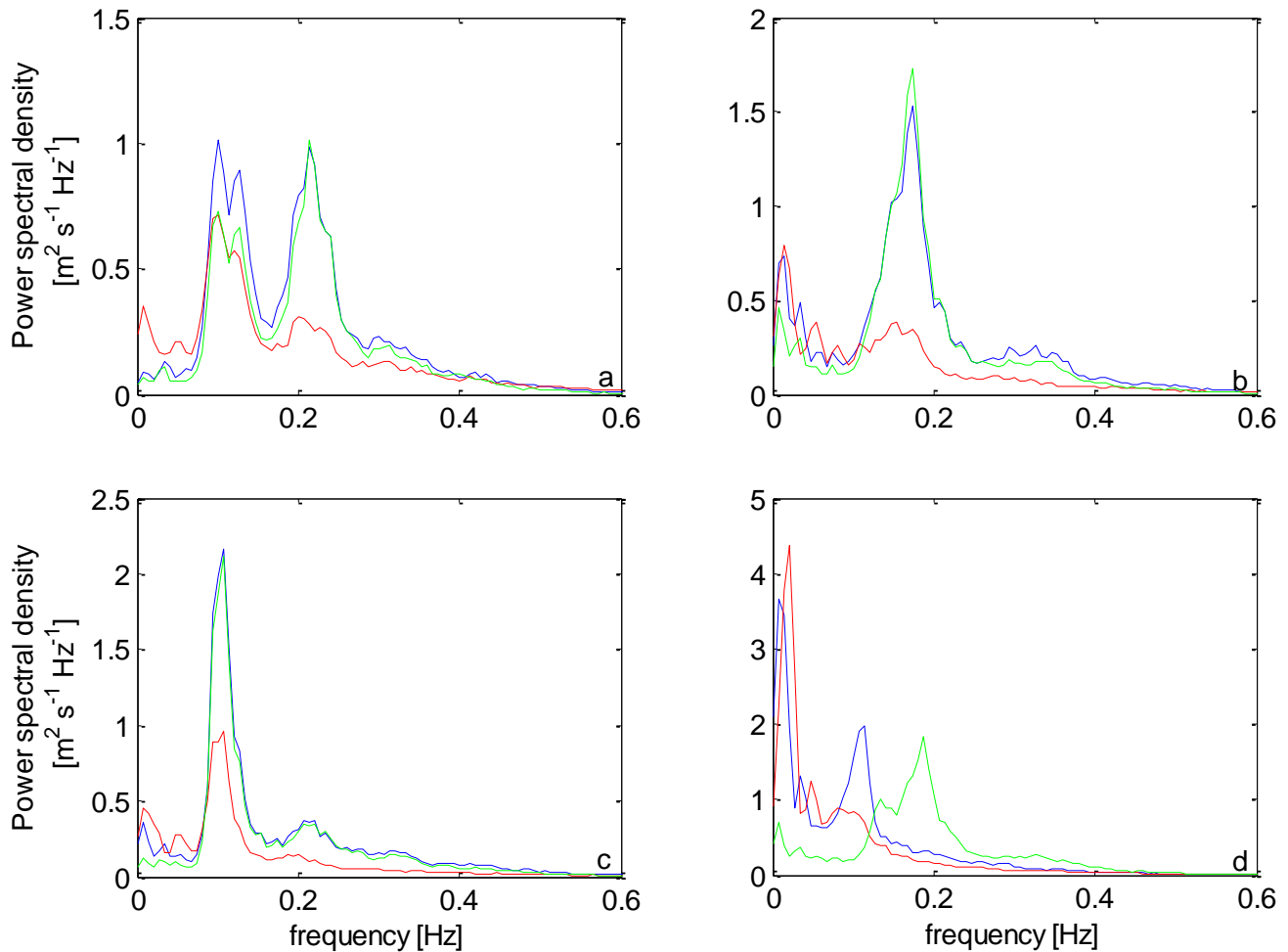


Figure 5.12: power spectral density of current velocity for the four selected cases a) tide 10, b) tide 12, c) tide 17 and d) tide 23. Green: Truc Vert Frame Blue: Mini-Frame 13 and red: Mini-Frame 15.

The direction of sediment transport by infragravity waves has seen to change with height, where close to the bed (~5 cm) sediment transport is directed offshore while higher above the bed the magnitude of the offshore sediment transport decreases and can even become weak onshore (Huntley and Hanes 1987). Figure 5.13 shows the difference in sediment transport direction and magnitude at different heights above the bed at Mini-Frame 13 for tide 10 and 17 where OBS1 is closest to the sea-bed. For both tides the lowest OBS shows the largest sediment transport magnitudes. Sea-swell waves show onshore directed transport and infragravity waves show offshore directed transport. For tide 10 the same pattern can be observed as in Huntley and Hanes (1987), suspended sediment transport by infragravity waves becomes smaller. However, for tide 17 (Figure 5.13b), differences between the three OBS's are smaller. Here OBS3 shows the largest offshore directed transport in the infragravity band. Figure 5.13 shows that the magnitude and direction of suspended sediment can differ for each OBS at a different height above the bed.

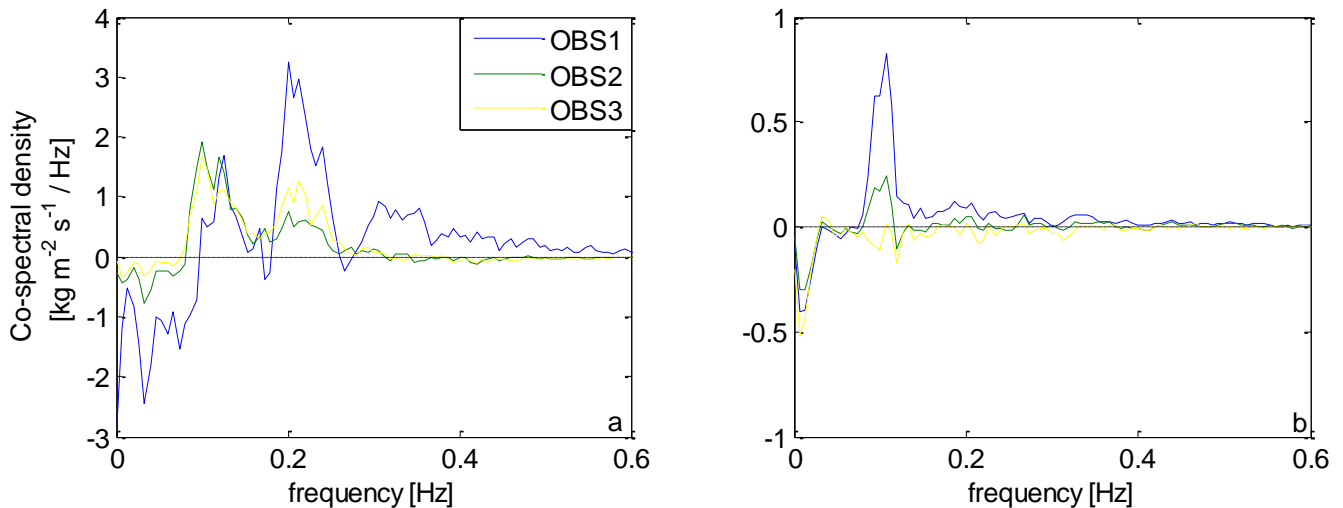


Figure 5.13: cross-spectra for Mini-frame 13 for the concentration signals from OBS1 (closest to the bed), OBS2 and OBS 3. a) tide 10 and b) tide 17.

Cross-spectra between suspended sediment concentration and flow velocity (Figure 5.14) reveal the trend observed in Figure 5.6d. The used sediment concentration signal is based on the positioning of the OBS. For all four selected tides the OBS's which are approximately at the same height at both Mini-frame 13 and 15 are chosen (thus not always the OBS closest to the bed). OBS height ranges from 2 cm to 7 cm above the bed.

During tide 10 (Figure 5.14a) sediment transport is dominated by sea-swell frequencies at Mini-Frame 13. Here, the infragravity wave component is smaller and is offshore directed. At Mini-Frame 15 both sea-swell and infragravity wave suspended sediment transport are onshore directed and have about the same but smaller magnitude compared to Mini-Frame 13.

During tide 12 (Fig 5.14b) suspended sediment transport by infragravity waves is dominant. The magnitude of sediment transport is equal at both Mini-Frame 13 and 15 but in opposite direction. Dominance of infragravity wave transport is expected when looking at Figure 5.7 where high suspension events occur on the time scale of infragravity waves. However, the low sea-swell transport at Mini-Frame 13 during tide 12 is surprising as the sea-swell frequency band dominated in the corresponding power spectra (Figure 5.12b). This might be explained by the absence of breaking waves or that breaking induced turbulence only reached the bottom during a deep infragravity wave trough.

During tide 17 (Figure 5.14c) suspended sediment transport by sea-swell waves is almost the same for both Mini-Frame 13 and 15 while power spectra show a large difference. Relative wave height is about the same (table 5-2 and 5-3) which might explain the similar amount of sediment transport. Sediment transport by infragravity at Mini-Frame 15 during tide 17 has the same magnitude as sediment transport by sea-swell waves and is again directed in the opposite direction compared to Mini-Frame 13. During tide 23 (Figure 5.14d) there is high onshore directed infragravity wave transport, here both Mini-Frames are both well within the surf zone and both spectra are dominated by infragravity waves.

For all tides with low-moderate energy conditions infragravity waves at Mini-Frame 13 (15) transport sediment in the offshore (onshore) direction. During high energy conditions both Mini-Frames show dominant onshore directed transport by infragravity waves.

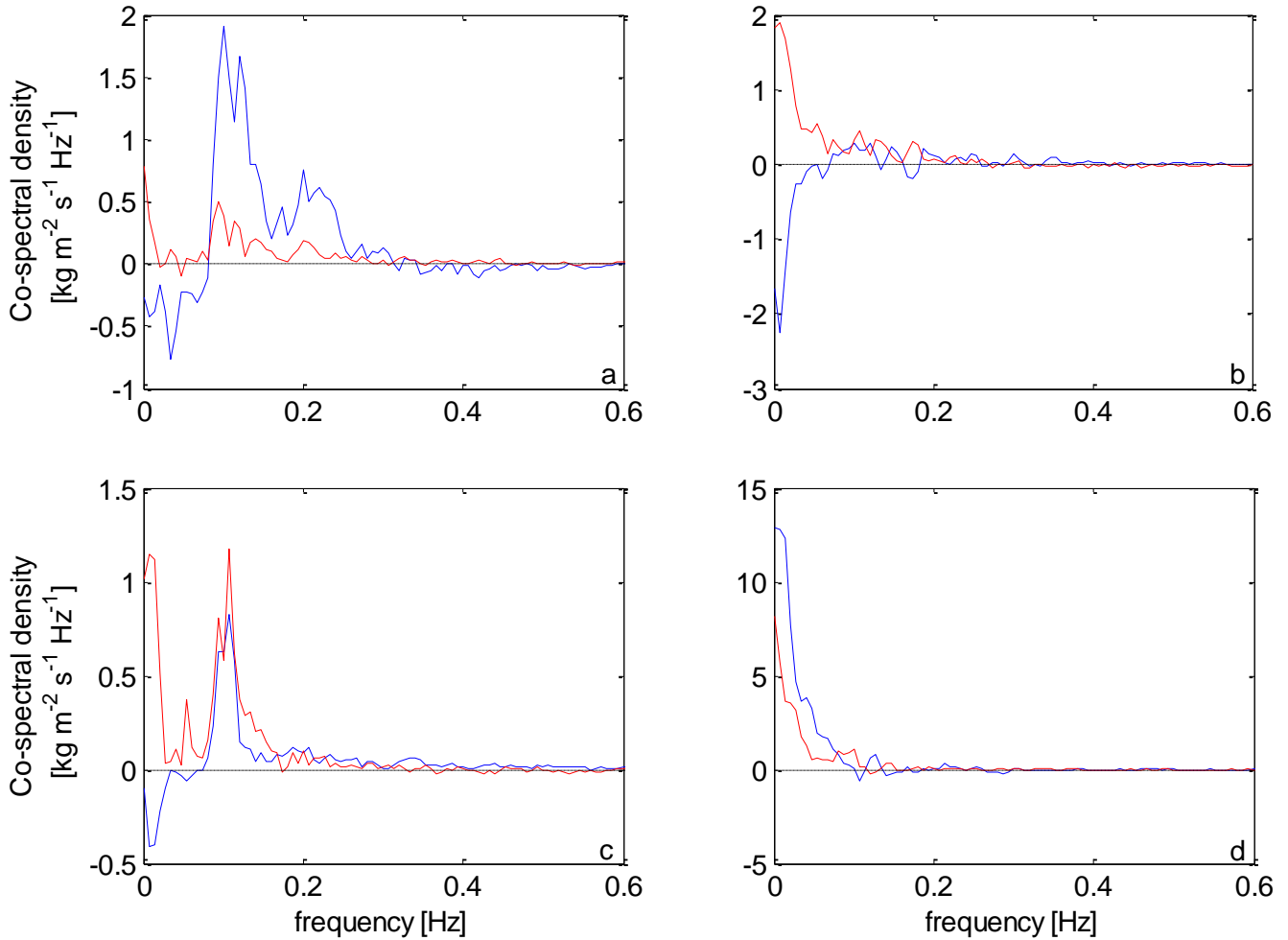


Figure 5.14: Co-spectral density between current velocity and suspended sediment concentration for the four selected cases a) tide 10, b) tide 12, c) tide 17 and d) tide 23. Blue: Mini-Frame 13 and red: Mini-Frame 15.

#### Correlation between suspended sediment and squared sea-swell wave velocity

To investigate the observations made in figures 5.7 to 5.10, sea-swell wave velocities are correlated to the suspended sediment concentration, following the method is described in Alsina and Cáceres (2011). They correlated square sea-swell wave velocities with suspended sediment concentrations during the trough phase of the infragravity wave. The correlations were calculated with the Pearson's product-moment correlation coefficient (PMCC) for moving averaged values. The PMCC ( $R$ ) between two random variables is defined as:

$$R_{x,y} = \frac{cov(X,Y)}{\sigma_x \sigma_y}$$

where  $cov(X, Y)$  is the covariance between  $X$  and  $Y$  and  $\sigma$  is the standard deviation of  $X$  or  $Y$ . PMCC oscillates between -1 and 1 indicating perfect negative/positive linear relationship between two variables. Here  $X$  is sea-swell wave velocity and  $Y$  is suspended sediment concentration. The method is based on the assumption that sea-swell velocities are the main sediment stirring mechanism. Alsina and Cáceres (2011) found relatively good correlations ( $R = 0.58$  and  $0.53$ ) between suspension events and squared sea-swell wave velocities at infragravity wave troughs during high energy wave conditions. They also observed that high suspended sediment concentrations often coincided with

negative peaks in infragravity wave velocity. They identified no strong correlation was found with sea-swell wave height, sea-swell wave horizontal velocity or Turbulent Kinetic Energy (TKE).

First the sea-swell wave velocity signal is squared and the 5-second average of the sediment concentration, sea-swell - and infragravity-wave velocity signals are calculated. The moving average of 5 seconds is chosen because it is roughly the period of sea-swell waves and it removes some random effects. The averaged infragravity-wave velocity signal has been separated into positive and negative velocities to make a distinction between the trough and crest phase. Figures 5.15 and 5.16 show the correlation between 5-second averaged suspended sediment concentrations and averaged squared sea-swell wave velocity in the trough (c), crest (b) and during both phases of the infragravity wave (a). A positive correlation means that sediment concentrations are high during large sea-swell velocities. Table 5-6 gives an overview of the correlations for tide 10, 12 17 and 23.

*Table 5-6: Correlation factors between averaged square sea-swell wave velocity and averaged suspended sediment concentrations.  $R_{all}$ : during both positive (onshore) and negative (offshore) averaged infragravity wave velocities,  $R_{crest}$ : during positive averaged infragravity wave velocities and  $R_{trough}$ : during negative averaged infragravity wave velocities.*

<b>Tide 10</b>	<b>TV frame</b>	<b>Mini 13</b>	<b>Mini 15</b>	<b>Mini 16</b>
$R_{all}$	0.03	0.50	0.12	-
$R_{crest}$	0.01	0.47	0.03	-
$R_{trough}$	0.02	0.50	0.21	-
$r_0$	-0.51	-0.46	-0.04	-
<b>Tide 12</b>	<b>TV frame</b>	<b>Mini 13</b>	<b>Mini15</b>	<b>Mini 16</b>
$R_{all}$	0.06	0.06	0.13	-
$R_{crest}$	0.03	0.09	0.11	-
$R_{trough}$	0.03	0.01	0.13	-
$r_0$	-0.54	-0.33	0.27	-
<b>Tide 17</b>	<b>TV frame</b>	<b>Mini 13</b>	<b>Mini15</b>	<b>Mini 16</b>
$R_{all}$	0.40	0.16	0.09	-
$R_{crest}$	0.30	0.19	0.13	-
$R_{trough}$	0.41	0.12	0.03	-
$r_0$	-0.50	-0.35	0.28	-
<b>Tide 23</b>	<b>TV frame</b>	<b>Mini 13</b>	<b>Mini15</b>	<b>Mini 16</b>
$R_{all}$	0.20	0.11	0.22	-
$R_{crest}$	0.22	0.09	0.24	-
$R_{trough}$	0.16	0.10	0.14	-
$r_0$	0.23	0.26	0.29	-

The data set generally returns poor correlations compared to what Alsina and Cáceres (2011) found. Expected was to see higher correlations during the infragravity wave trough phase than during the crest phase, however this is not the case. Especially for conditions at tide 12, Mini-frame 13 (Figure 5.7), where peaks in sediment concentration occur during negative infragravity-wave velocities, higher correlations were expected. The low values of R show that peaks in sediment concentration do not correspond well to high sea-swell wave velocities. Figures 5.15 and 5.16 illustrate a moderately good (0.47 – 0.5) and a poor (0.01 – 0.06) correlation, respectively. The same method was applied for

infragravity wave velocities itself and suspended sediment concentrations, however this resulted in similar poor correlations.

Several possible explanations for the poor correlations can be given. Firstly; due to the fixed position of only a few OBS's along the cross-shore transect it is very unlikely that the OBS is in the exact position where it can measure the maximum suspended sediment concentration generated by a single sea-swell wave. Second, there is probably a time-lag between the highest measured velocity and the entrained sediment to reach the height of the OBS. The time at which velocities are highest does not correspond with highest suspended sediment concentrations. Third, the possible presence of ripples might change the behaviour of suspended sediment. During onshore velocities the sediment is trapped in a vortex at the lee side of the ripple. During flow reversal the entrained sediment is released and is injected as plume into the water column and transported in the generally weaker offshore directed stroke. The latter explanation would mean that maximum suspended sediment concentrations would occur when flow velocities are around zero.

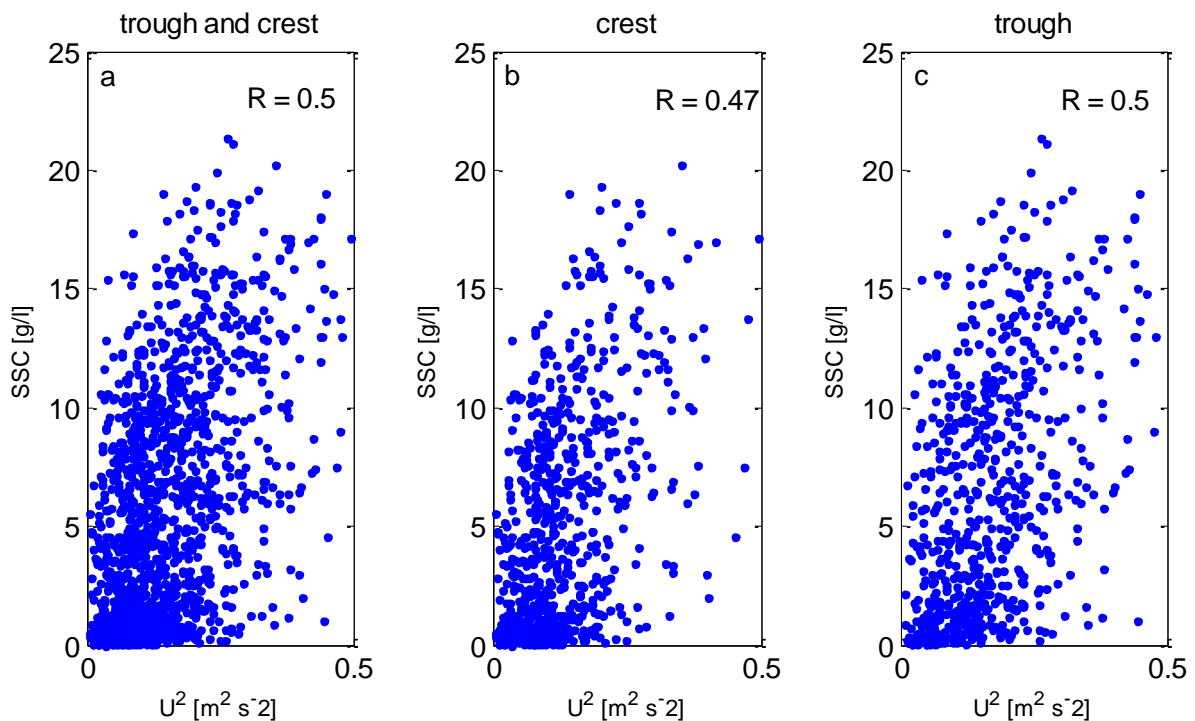


Figure 5.15: Correlation plot between suspended-sediment concentration and: a) square sea-swell wave velocity, b) square sea-swell wave velocity during the crest phase of the infragravity wave and c) square sea-swell wave velocity during the trough phase of the infragravity wave during tide 10 at Mini-Frame 13.

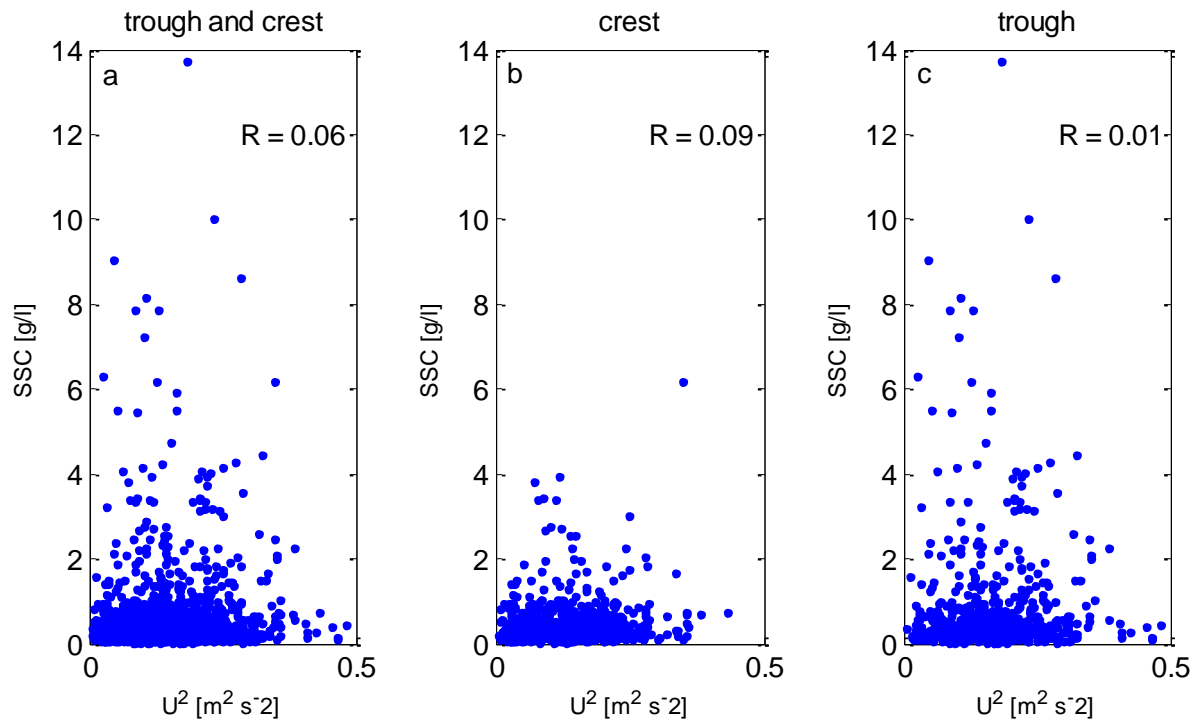


Figure 5.16: Correlation plot between suspended sediment concentration and: a) square sea-swell wave velocity, b) square sea-swell wave velocity during the crest phase of the infragravity wave and c) square sea-swell wave velocity during the trough phase of the infragravity wave during tide 12 at Mini-Frame 15.

### Suspension events

No relevant correlation could be identified between suspended sediment concentrations and squared sea-swell/infragravity -wave velocities. Here we investigate whether intense suspended sediment event coincide with high infragravity (onshore and offshore) wave velocities. Figure 5.17 shows the percentage at which an intense suspended sediment concentration event coincided with a high infragravity-wave velocity event at Mini-Frame 13 and 15. An intense sediment suspension event is defined when the suspended sediment concentration is larger than two times the standard deviation of the considered concentration time-series. A high velocity event is identified when the velocity is higher than the standard deviation of the velocity signal. A value of 10% in figure 5.17 means that for 10% of the entire time-series high infragravity wave velocities coincide with high sediment concentrations. Values are rather low and are typically around 4-6%. This means that intense sediment events do not seem to relate well to high infragravity orbital velocities. An increase in velocity does not implicitly mean an increase in sediment concentration, nor does a deep trough or high crest stir more sediment.

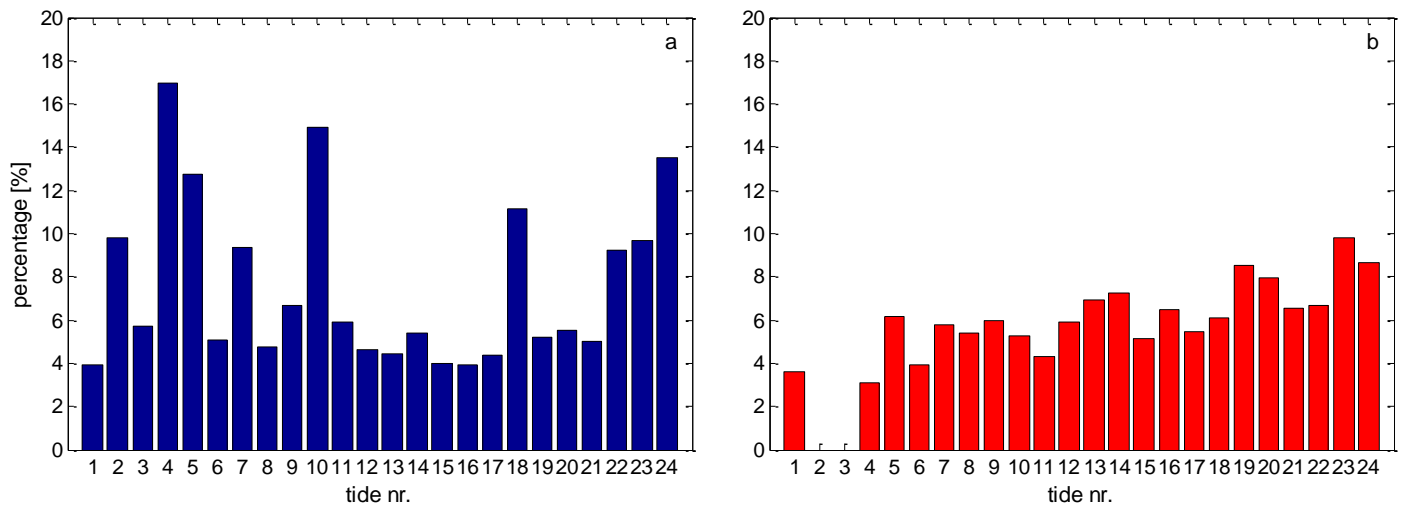


Figure 5.17: Percentage at which high infragravity-wave velocities coincide with an intense suspended-sediment event. a) Mini-frame 13 and b) Mini-frame 15.

The next figure visualises the location of intense suspension events relative to the infragravity-wave crest or trough. The same method as in figure 5.17 is used for defining a high intensity suspended sediment event. For figure 5.18, the corresponding infragravity-wave velocities that occur during these selected suspended-sediment events are split into negative and positive velocities. No distinction is made on the magnitude of the velocity. From there the fraction is calculated for which intense suspended sediment events correspond to negative or positive velocities (Figure 5.18). For example, when the fraction is 0.7 in figure 5.18a then 70% (30%) percent of the time an intense suspended sediment event occurs during negative (positive) infragravity-wave velocities. Figure 5.18a (b) shows the fraction for negative (positive) infragravity-wave velocities plotted against the  $r0$ . For negative  $r0$  most intense events occur during the infragravity-wave trough (offshore directed transport), when  $r0$  becomes increasingly more positive the intense events predominantly occur at infragravity wave crests (onshore directed transport). This shows that the position of the sea-swell waves relative to the infragravity wave determines, for a large part, when an intense suspension event occurs and its corresponding transport direction.

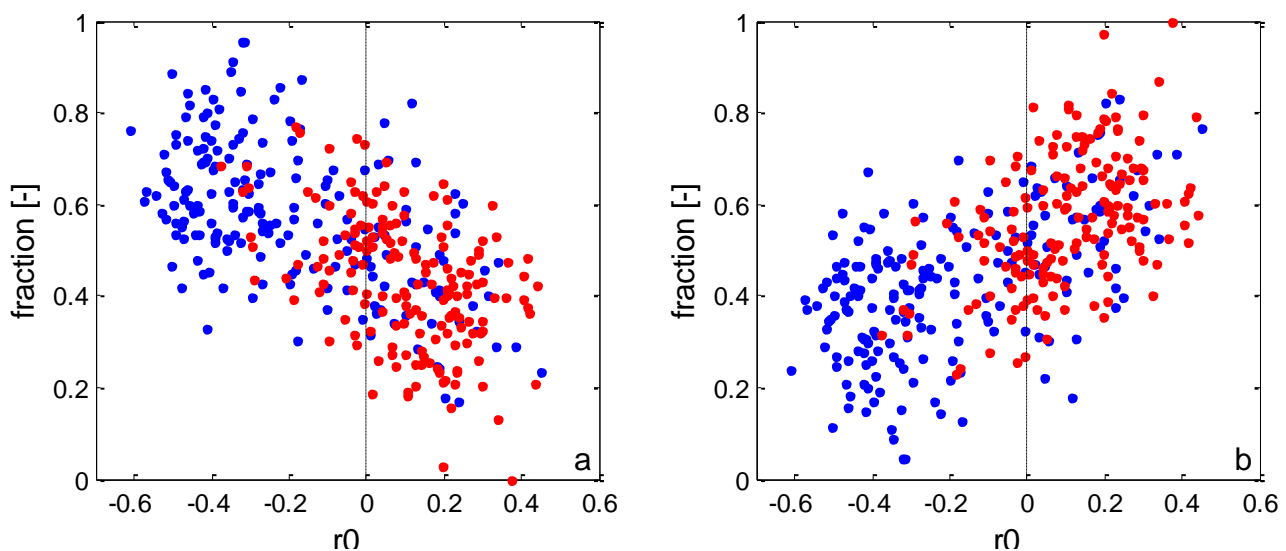


Figure 5.18: Plot of the fraction for which intense suspended-sediment events correspond to negative or positive infragravity wave velocities against  $r0$  for the bulk data set with a) fraction during negative infragravity-wave velocities and b) fraction during positive infragravity-wave velocities. Blue: Mini-Frame 13 and red: Mini-Frame 15.

### Transport directions

Figures 5.7 and 5.9 show that especially at locations where  $r_0$  is negative, peaks in sediment concentrations can visually be linked to offshore directed infragravity wave velocities. However, when concentration signals become increasingly more chaotic, visually identifying trends becomes increasingly more difficult. It is expected that high sea-swell waves break first in the trough of an infragravity-wave, dissipate energy and thereby stir up sediment. After breaking of the largest waves, the cross-correlation between the sea-swell wave envelope and the infragravity wave becomes positive and the highest sea-swell waves then occur on the infragravity-wave crest. Then the sea-swell waves at the crest start to break and the cross-correlation goes towards 0 again. Figure 5.19 shows the 15-minute averaged infragravity-wave suspended sediment transport from the bulk data set at Mini-frame 13 and 15 plotted against  $r_0$ . At negative values of  $r_0$ , infragravity-wave transport is predominantly offshore directed. Values between -0.1 and 0.1 can roughly be considered as a transition zone where infragravity-wave transport occurs in both onshore and offshore directions, here high sea-swell waves occur both in the infragravity wave trough and crest. Values of  $r_0 > 0.1$  show a predominantly onshore infragravity-wave suspended sediment transport. In general, positive values of  $r_0$  also correspond to higher transport rates than at negative values of  $r_0$ . This trend might be caused by the fact that when the infragravity-wave is still bound and  $r_0 < 0$ , the waves are still in the shoaling- or first part of the surf zone and sediment suspension is small due to the absence of breaking waves. When the correlation  $> 0$  more intense wave-breaking occurs and turbulence travels towards the bed, suspending larger amounts of sediment which can be transported by the infragravity-wave.

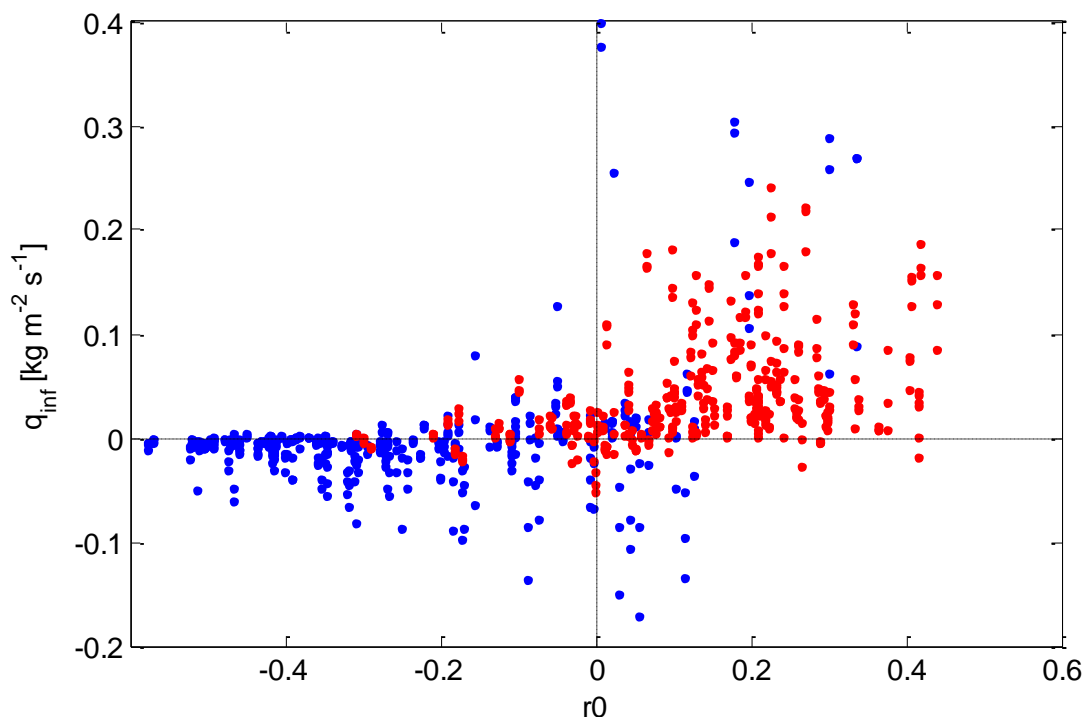


Figure 5.19: 15-minute averaged suspended sediment transport by infragravity waves ( $q_{ig}$ ) plotted against  $r_0$ . Blue: Mini-Frame 13 and red: Mini-Frame 15.

The same figure but then for sea-swell waves can be seen in figure 5.20. For both positive and negative values of  $r_0$  sea-swell wave sediment transport is predominantly directed onshore and magnitudes are about the same. Some offshore transport occurs at Mini-Frame 13 when values of  $r_0$  are around zero.

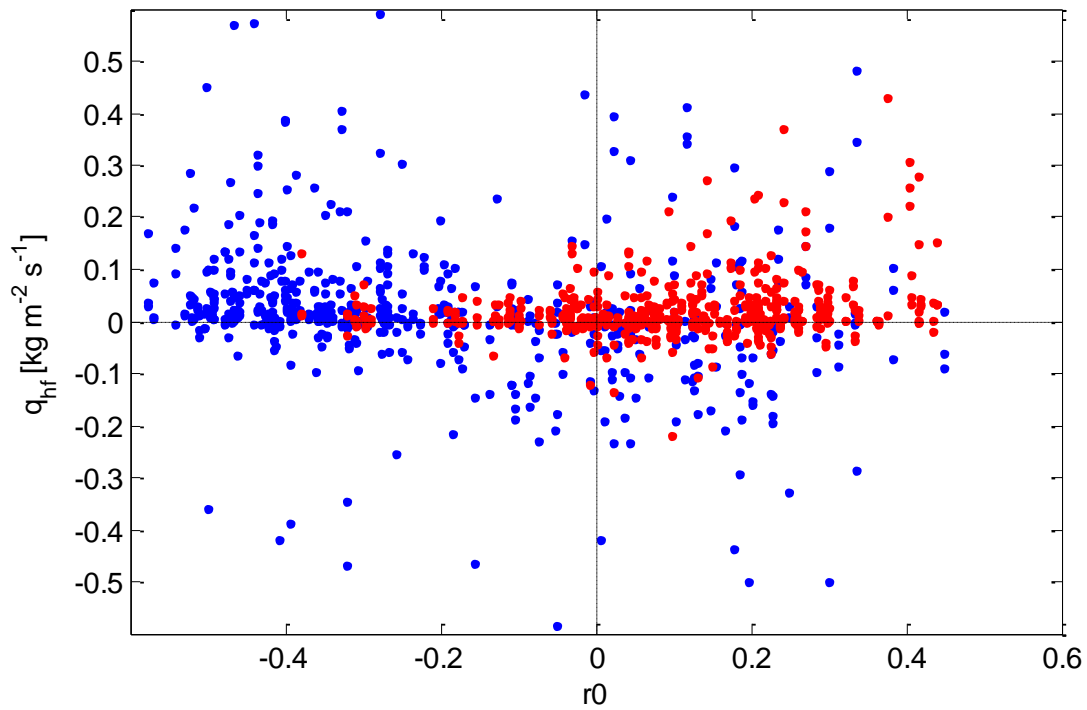


Figure 5.20: 15-minute averaged suspended sediment transport by sea-swell waves ( $q_{hf}$ ) plotted against  $r0$ . Blue: Mini-Frame 13 and red: Mini-Frame 15.

## 6. Discussion

The discussion contains four sections, in the first section the research sub-questions will be answered and discussed. The second section answers the main research question. In the third section, our results are compared with previous studies and in the fourth section an outlook is given for future research directions.

### 6.1 Sub questions

**Q1: What is the relative importance of infragravity-wave induced transport compared to transport by sea-swell waves and the mean transport during different wave conditions?**

Suspended sediment transport by infragravity waves is equally important as sediment transport by sea-swell waves. Sediment transport is, however, dominated by mean currents. This results in a net offshore-directed transport close to the bed (at 2 – 20 cm), for the 24 tides considered.

**Q2: Can we identify the advection transport in our observations?**

The advection mechanism can be identified in several ways;

- 1) When looking at figure 5.6 an increase in suspended sediment transport can be seen at a relative significant wave height of  $\sim 0.45 - 0.5$ . At this point sea-swell waves break (Figure 5.3) and subsequently stir up sediment which is partly transported by infragravity waves.
- 2) When  $r_0$  has a negative value, intense suspension events occur predominantly in infragravity wave troughs (Figure 5.18). Negative values of  $r_0$  occur in relatively deep water where the infragravity wave is still bound. The largest sea-swell waves are present in the trough and are likely to break first and, again, stir up sediment which is partly transported by the infragravity wave trough in the offshore direction. It is highly unlikely that in this part of the coastal regime infragravity waves suspend sediment, as the height of infragravity waves is about 10-15% of the sea-swell wave height (Figure 5.1), and water depth of 1 m.

**Q3: Can infragravity waves suspend sediment, and if so, in what way?**

Infragravity waves can suspend sediment in a both indirect and direct way. The indirect way is sea surface elevation modulation by the infragravity wave, causing sea-swell waves to be in either deeper (on top of the crest) or shallower (in the trough) water. This mechanism can become important at values of  $r_0$  between  $\sim -0.1$  and  $\sim 0.4$  where sea-swell waves in the trough have the same height as in the crest of the infragravity wave. The water depth modulation by the infragravity wave might then be responsible for whether a sea-swell wave breaks or not. Close to shore it is very likely that infragravity waves stir sediment themselves as they become increasingly dominant towards the shore (Figure 5.2). Assuming that infragravity waves do not break, the suspension mechanism of sediment would be caused by orbital velocities near the bed. However, recent studies by van Dongeren et al. (2007) and de Bakker et al. (2014) suggest that infragravity waves do break in the nearshore which might be an extra stirring agent

### 6.2 Main question

**What are the processes behind the spatial variability in the cross-shore direction of sediment transport induced by infragravity waves?**

Sediment transport by infragravity waves can be subdivided into three cross-shore zones (Figure 6.1). Location (a) shows a highly idealized offshore situation where high sea-swell waves are present in the trough. In the first part of the surf zone the high sea-swell waves located in trough break first

and suspended sediment is transported offshore by the infragravity-wave (Figure 5.19). Outside the surf zone, the sequences of large sea-swell waves, present in the trough of the bound infragravity-wave (where velocities are offshore directed), stir a larger amount of sediment than the sequences of small sea-swell waves present on the infragravity-wave crest. The infragravity wave probably causes an insignificant change in sea surface elevation to have a pronounced effect on whether sea-swell waves break or not during measured conditions. For our dataset, the dominant mechanism for where sea-swell waves break first is the height of the sea-swell wave itself. At location (b) exactly the opposite happens and suspended sediment is transported onshore by the infragravity wave. Here, sea-swell waves in the trough of the infragravity-wave have dissipated a large part of their energy. The sea-swell waves at the crest are larger and cause higher suspended-sediment concentrations than sea-swell waves in the trough which results in a net onshore directed transport by infragravity waves. At both location (a) and (b) sediment suspension is most likely caused by sea-swell wave velocities and/or turbulence injected into the water column due to breaking sea-swell waves. At location (c) the infragravity wave itself causes suspension of sediment. The direction of transport is here expected to be offshore when taking into account the observations in Figure 5.11, where suspension events occur during the trough phase of the infragravity wave.

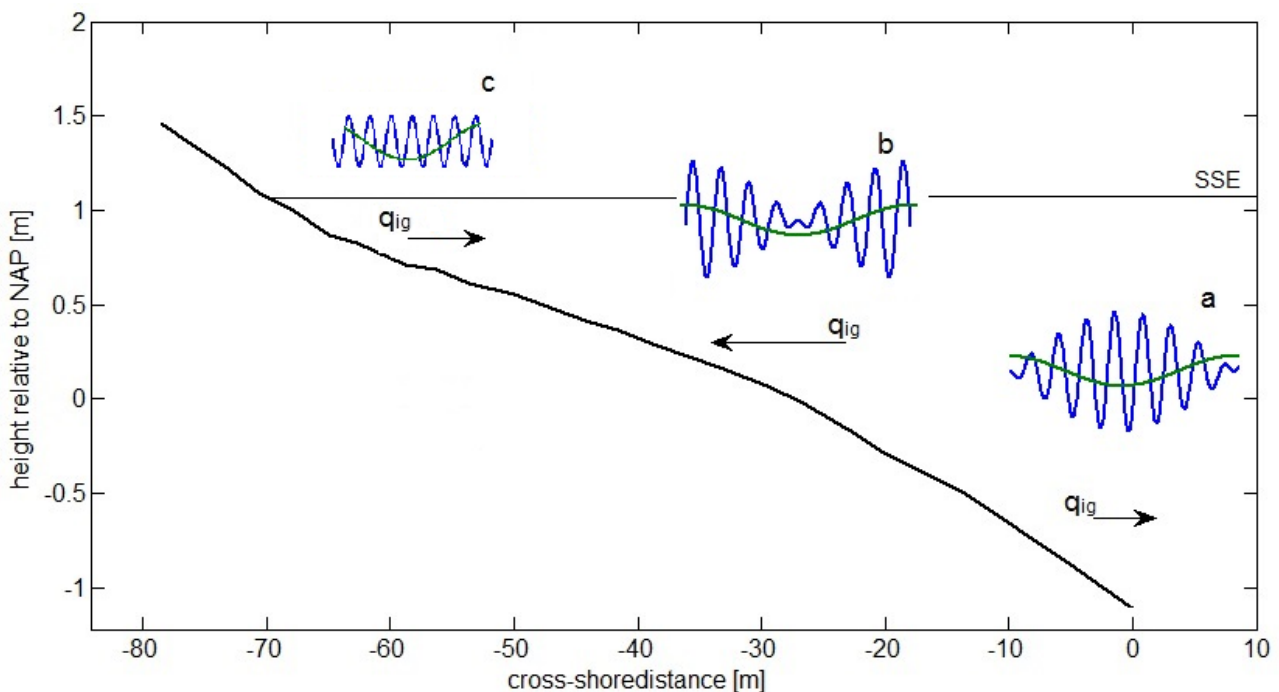


Figure 6.1: Overview of the transport by infragravity waves depending on the cross-shore position and relative location of sea-swell waves (highly idealized). a)  $r_0 = -1$ , b)  $r_0 = 1$  and c)  $r_0 = 0$ .

### 6.3 Comparison with literature

We observe that sediment transport in the nearshore increases significantly when sea-swell waves, in agreement with literature, start to break (Figure 5.6). For example, measurements by Houser and Greenwood (2005) show a similar trend regarding suspended sediment transport, with an increase in suspended sediment transport with higher values of  $H_s/h$  (Figure 3.9). Although, contrary to our observations, the mean sediment transport component which is, in Figure 3.9 not dominant over the oscillating components. This probably is due to the gentler slope as for the same wave

conditions the undertow is stronger on steep-sloping beaches than on gentle-sloping beaches (Longuet-Higgins and Stewart, 1964).

Bound infragravity waves, with  $r_0 < 0.1$  here seem to transport sediment in the offshore direction (Figure 5.16), just seaward of the surf zone. The offshore sediment transport by the infragravity wave is due to the group behaviour of incident sea-swell waves where large sea-swell waves present in the trough stir a larger amount of sediment than the smaller sea-swell waves present on the crest of the infragravity wave. These observations are in line with Huntley and Hanes (1987) and Osborne and Greenwood (1992) who observe near-bed suspended sediment transport to be strongly onshore directed at sea-swell wave frequencies, and weakly offshore directed at infragravity-wave frequencies outside the surf zone (Figure 5.14 a and c). Also, Huntley and Hanes (1987) observed a change of sediment transport rate with height above the bed (Figure 3.4), even showing opposite directed transport for higher located sensors. We observe for For tide 10 (Figure 5.13) similar trends, although onshore transport is not identified. For tide 17 an increase in sediment transport at infragravity-wave frequencies at the highest OBS can be seen instead of an expected decrease.

Beach and Sternberg (1988) and Smith and Mocke (2002) both observed suspended sediment events at the scale of infragravity waves. Similar results can be seen in Figure 5.8, however this occurrence seems random. During other recorded velocity and concentration signals with almost similar boundary conditions no such patterns can be observed.

According to Aagaard and Greenwood (2008), infragravity waves transport sediment onshore (offshore) landward (seaward) of a resuspension maximum, however the exact explanation is unclear to us. They assume, a resuspension maximum where relative wave height is highest. But this does not directly explain the variable transport directions. The cross-correlation factor,  $r_0$ , can more or less be a surrogate for relative wave height. In Figure 5.3 it can be seen that maximum relative wave height occurs in the range where  $r_0$  is between  $-0.3$  and  $0.2$ , at the location where sea-swell waves break. When comparing Figure 3.5 and 5.19, it can be seen that they look more or less similar. Both figures show small offshore directed transport seaward of a resuspension maximum / negative values of  $r_0$ , and larger onshore directed transport landward of a resuspension maximum / positive values of  $r_0$ . From this we conclude that landward (seaward) of the resuspension maximum in Figure 3.3,  $r_0$  is positive (negative).

The overall effect of infragravity waves on morphology just outside and inside the surf zone is expected to be small. During the four selected tides the mean transport component ultimately defined the net suspended-sediment transport direction. Closer to the shore the infragravity wave can become more dominant. The most prominent result observed by Russell (1993) is that infragravity waves can totally dominate the frequency dependent near-bed (suspended) sand transport from the inner surf zone during storm conditions on a moderately sloping beach (1:70), and that this transport is predominantly offshore directed at infragravity frequencies. This means that that the infragravity wave is the main mechanism by which the beach erodes during storm. Similar observations can be made here on a relatively steep sloping beach (1:30) during storm conditions. Both the energy spectrum (Figure 5.12d) and suspended sediment transport (Figure 5.14d) at Mini-Frame 13 and 15 are dominated by infragravity frequencies, however, the direction of sediment transport is onshore. Mini-Frame 16, which is located further landward shows possible signs of net offshore transport at infragravity frequencies (Figure 5.11). This cannot be validated due to the lack of a reliable velocity signal.

It could be hypothesized that on a gentler sloping beach the effect visible in Figure 5.19, where infragravity waves transport sediment offshore for values of  $r_0 < 0$  and onshore for values of  $r_0 > 0$ , will

probably be more pronounced. The transition from bound to free waves can take place over a longer distance and thus takes more time. The time gap between breaking large sea-swell waves present in the trough and smaller sea-swell waves at the crest of the infragravity wave is larger. This might lead to a more pronounced offshore transport signal further seaward where  $r_0$  values are negative and a more pronounced onshore transport signal when  $r_0$  values are positive. Furthermore, on a gentler slope infragravity wave growth due to energy-transfers from higher harmonics is larger compared to a steep slope. Resulting in relatively more energy in the infragravity wave band and thus the possibility of larger amounts of sediments being transported by infragravity waves.

#### **6.4 Suggestions for further research**

High-suspension events during high negative-velocity events of the infragravity wave seem to be event-based and only when certain requirements are met. These suspension events cannot be identified when purely looking at average infragravity-wave height, sea-swell wave height on relative wave height. While conditions were almost similar the sediment concentration signal showed different dynamics (tide 12 and 17, figures 5.7 and 5.9). It would be interesting to know when and at which conditions such a suspension event occurs and whether it might be linked to breaking intensity.

In the inner surf- and swash zone, infragravity waves are dominant and high suspended sediment concentration occur, potentially leading to large morphological change. However in this region measurements are limited because of the presently available measurement instruments. Future research should therefore focus on the inner-surf and swash zone.

## 7. Conclusion

Field data collected during a six-week field campaign has been used to study the direction of sediment transport by infragravity waves in the cross-shore direction in the intertidal area at the Sandmotor, The Netherlands. Flow velocity meters, pressure sensors and sediment concentration meters were positioned in a cross-shore array on a relatively steep sloping beach (1:30).

In the surf zone, mean-current induced sediment transport is seen to dominate over oscillating transport, and sediment transport by infragravity waves has the same order of magnitude as sea-swell waves. When looking only at intense suspended-sediment events (defined as an event where the suspended sediment concentration is two times the standard deviation of the considered concentration time-series) they are seen to correlate well with the relative position of the sea-swell wave on top of the infragravity wave. Intense events predominantly occur during negative infragravity wave velocities (trough phase) when  $r_0$  is negative. When  $r_0$  becomes increasingly positive, intense sediment suspension events occur during positive infragravity-wave velocities.

The direction of suspended-sediment transport by infragravity waves is seen to depend strongly on the relative location of the sea-swell waves on top of the infragravity wave, quantified by the  $r_0$  parameter. When  $r_0$  has a negative (positive) value, the largest sea-swell waves predominantly occur in the trough (crest) of the infragravity wave and suspended-sediment transport by infragravity waves is directed offshore (onshore). In general  $r_0$  is negative outside the surf zone, due to the groupiness behaviour of sea-swell waves, and becomes positive in the shoreward direction when the group structure disappears leading to onshore transport. This results in a sediment divergence along the cross-shore due to infragravity waves. However, the overall effect of sediment divergence is overruled by the mean transport component which causes the net suspended sediment transport to be offshore directed. During the four selected tides, suspended-sediment concentrations do not show strong correlations with square sea-swell wave velocities nor is there a specific preference for the trough or crest phase of the infragravity wave.

Overall, in the surf- and shoaling zone, the infragravity wave acts as an advective agent and transports sediment stirred by sea-swell waves with the direction of the suspended-sediment transport linked to the relative position of larger sea-swell waves being present on either the crest or trough of the infragravity wave. Closer to shore infragravity waves might stir their own sediment, however the used data set does not have reliable data in the inner-surf and swash zone to investigate this in depth.

## 8. References

- Alsina, J.M., Cáceres, I. – (2011) Sediment suspension events in the inner surf and swash zone. Measurements in large-scale and high-energy wave conditions. *Coastal engineering*, vol. **58**, p. 657-670
- Aagaard, T., Greenwood, B. – (2008) *Infragravity wave contribution to surf zone sediment transport – The role of advection*. *Marine Geology* **251** pages 1–14.
- Battjes, J.A., Bakkenes, H.J., Janssen, T.T., and van Dongeren, A.R. – (2004) *Shoaling of subharmonic waves*. *Journal of Geophysical research*, vol **109**.
- Baldock, T.E., Huntley, D.A., Bird P.A.D., O'Hare, T., Bullock, G.N. – (2000) *Breakpoint generated surf beat induced by bichromatic wave groups*. *Coastal Engineering*, vol. **39**, p. 213–242.
- Beach, R.A., Sternberg, R. – (1988) *Suspended sediment transport in the surf zone: response to cross-shore infragravity motion*. *Marine Geology*, Vol. **80**, 61-79.
- Butt, T., and Russell, P. – (1999) *Suspended sediment transport mechanisms in high-energy swash*. *Marine geology*, vol. **161**, p. 361-375.
- de Bakker, A.T.M., Tissier M.F.S., Ruessink B.G. – (2014) *Shoreline Dissipation of infragravity waves*. *Continental Shelf Research*, vol. **72**, p. 73–82.
- Drake, T.G., and Calantoni J. – (2001) *Discrete particle model for sheet flow sediment transport in the nearshore*. *Journal of Geophysical research*, vol. **106**, p. 19,859 – 19,868.
- Guedes, R.M.C., Bryan, K.R., Coco, G. – (2013) *Observations of wave energy fluxes and swash motions on a low-sloping, dissipative beach*. *Journal of geophysical research: Oceans*, Vol. **118**, 3651-3669
- Hamm L., Madsen P.A., Peregrine D.H. – (1993) *Wave transformation in the nearshore zone: a review*. *Coastal Engineering*, vol. **21**, 5-39 Elsevier Science Publishers B.V., Amsterdam.
- Holthuijsen, L.H. – (2006) *Waves in oceanic waters*. Cambridge University press.
- Houser, C., Greenwood, B. – (2005) *Hydrodynamics and sediment transport within the inner surf zone of a lacustrine multiple-barred nearshore*. *Mar. Geol.* vol. **218**, 37–63.
- Huntley, D.A., and Hanes, D.M. – (1987) *Direct measurement of suspended sediment transport*. *Coastal Sediments '87*. (New Orleans). *Am. Soc. Civ. Eng.*, New York, pp. 723-737.
- Hsu, T.J., and Hanes, D.M. – (2004) *Effects of wave shape on sheet flow sediment transport*. *Journal of Geophysical research*, vol. **190**, C05025.
- Lippman, T.C., Herbers, T.H.C., Thornton, E.B. – (1999) *Gravity and Shear Wave Contributions to Nearshore Infragravity Motions*. *American Meteorological Society*, Vol. 29.
- Longuet-Higgins, M.S., Stewart, R.W. – (1964) *Radiation stresses in water waves - a physical` discussion with applications*. *Deep-Sea Res.* vol. **11**, 529–562.
- Longuet-Higgins, M.S., Stewart, R.W. – (1962) *Radiation stress and mass transport in gravity waves, with application to 'surf-beats'*. *Journal of Fluid Mechanics* **13**, 481-504.
- Osborne, P.D., Greenwood, B. – (1992). *Frequency dependent cross-shore suspended sediment transport. 1. A non-barred shore face*. *Marine Geology*, vol. **106**, 1-24 Elsevier Science Publishers B.V., Amsterdam.
- Ruessink, B.G. – (1998) *The temporal and spatial variability of infragravity energy in a barred nearshore zone*. *Continental Shelf Research*, vol. **18**, p. 585-605.
- Ruessink, B.G., Michallet, H., Abreu, T., Sancho, F., Van der A, D.A., Van der Werf, J.J., and Silva, P.A. – (2011), *Observations of velocities, sand concentrations, and fluxes under velocity-asymmetric oscillatory flows*. *Journal of geophysical research*, Vol. **116**, C03004
- Russell, P.E. – (1993) *Mechanisms for beach erosion during storms*. *Continental Shelf Research*, vol. **13**, No. 11, pp. 1243-1265.
- Smith, G.G., Mocke, G.P. – (2002) *Interaction between breaking/broken waves and infragravity-scale phenomena to control sediment suspension transport in the surf zone*. *Marine Geology*, vol. **187** 329-345

- Symonds G., Huntley D.A. and Bowen A.J – (1982) *Two-Dimensional surf beat: Infragravity wave Generation by a time varying breakpoint*. Journal of geophysical research, vol. **87**, no. c1, pages 492-498.
- Thomson, J., Elgar, S., Raubenheimer, B., Herbers, T.H.C., and Guza, R.T. – (2006) *Tidal modulation of infragravity waves via nonlinear energy losses in the surf zone*. Geophysical research letters, vol. **33**.
- Thornton, B. – (1979) *Energetics of breaking waves within the surf zone*. Journal of geophysical research, Vol. **84**, No. C8.
- van Dongeren, A. R., Svendsen I. A., and Sancho F. E. – (1996), Generation of infragravity waves, in Proceedings of the 25th International Conference on Coastal Engineering, edited by B. Edge, p. 1335–1348, Am. Soc. of Civ. Eng., Reston, Va.
- van Dongeren, A., Battjes, J., Janssen, T., van Noorloos, J., Steenhauer, K., Steenbergen, G., Reniers, A., - (2007) *Shoaling and shoreline dissipation of low-frequency waves*. Journal of Geophysics. Res. vol. **112**, C02011.
- Yu, Y., Sternberg, R.W., Beach, R.A. – (1993) *Kinematics of breaking waves and associated suspended sediment in the nearshore zone*. Continental Shelf Research, Vol. **13**, No. 11, pp. 1219-1242.
- Zhang, D. P. and Sunamura, T. – (1990) *Conditions for the occurrence of vortices induced by breaking waves*. Coastal Eng. Japan, Vol. **33**, pp. 145-155.